Finite element solution of interface and free surface three-dimensional fluid flow problems using flow-condition-based interpolation

by

Soyoung You

Submitted to the Department of Mechanical Engineering
in partial fulfillment of the requirements for the degree of

Doctor of Philosophy in Mechanical Engineering and Computation

at the

MASSACHUSETTS INSTITUTE OF TECHNOLOGY

February 2015

Author . . . . . .
Department of Mechanical Engineering
January 13, 2015

Certified by . . . . . .
Klaus-Jürgen Bathe
Professor of Mechanical Engineering
Thesis supervisor

Accepted by . . . . . .
David Edgar Hardt
Chairman, Departmental Committee on Graduate Students

Accepted by . . . . . .
Nicolas G. Hadjiconstantinou
Co-Director, Computational Science and Engineering

Finite element solution of interface and free surface three-dimensional fluid flow problems using flow-condition-based interpolation

by

Soyoung You

Submitted to the Department of Mechanical Engineering
on January 13, 2015, in partial fulfillment of the
requirements for the degree of
Doctor of Philosophy in Mechanical Engineering

Abstract

The necessity for a highly accurate simulation scheme of free surface flows is emphasized in various industrial and scientific applications. To obtain an accurate response prediction, mass conservation must be satisfied. Due to a continuously moving fluid domain, however, it is a challenge to maintain the volume of the fluid while calculating the dynamic responses of free surfaces, especially when seeking solutions for long time durations.

This thesis describes how the difficulty can be overcome by proper employment of an Arbitrary Lagrangian Eulerian (ALE) method derived from the Reynolds transport theorem to compute unsteady Newtonian flows including fluid interfaces and free surfaces. The proposed method conserves mass very accurately and obtains stable and accurate results with very large solution steps and even coarse meshes. The continuum mechanics equations are formulated, and the Navier-Stokes equations are solved using a 'flow-condition-based interpolation' (FCBI) scheme. The FCBI method uses exponential interpolations derived from the analytical solution of the 1-dimensional advection-diffusion equation.

The thesis revisits the 2-dimensional FCBI method with special focus on the application to flow problems in highly nonlinear moving domains with interfaces and free surfaces, and develops an effective 3-D FCBI tetrahedral element for such applications. The newly developed 3-D FCBI solution scheme can solve flow problems of a wide range since it can handle highly nonlinear and unsteady flow conditions, even when large mesh distortions occur. Various example solutions are given to show the effectiveness of the developed solution schemes.

Thesis Supervisor: Klaus-Jürgen Bathe
Title: Professor

Acknowledgements

I would like to give great gratitude to my thesis supervisor, Professor Klaus-Jürgen Bathe, for his support and inspirations throughout my degree.

The members of my thesis committee, Professor Henrik Schmidt and Professor Ken Kamrin, have provided many encouragements and suggestions.

I would like to show great respect to my mother, Eun-suk Lee for patience and encouragements.

I give much thanks to my colleague, Jean-Philippe Péraud for numerous support and useful discussions.

Contents

List of figures

Chapter 1

Introduction

Free surface analyses calculate fluid flow problems in continuously moving fluid domains. Many industries require free surface solutions, such as vehicle dynamics and earthquake engineering [1]. If free surfaces are not calculated correctly, the whole system and its environment may be affected - possibly causing catastrophic consequences such as instability of vehicles and the failure of containers storing hazardous fluids.

Because of the importance of accurately simulating free surfaces, intensive research efforts have been made towards the development of numerical methods for incompressible free surface flow solutions. The Volume of Fluid (VOF) method [2, 3] is a well-known scheme for an Eulerian approach which uses density functions. This approach can ensure mass conservation but a serious disadvantage of the method is that it does not accurately capture the interface [4].

A famous Lagrangian approach for free surface analysis is the Smoothed Particle Hydrodynamics (SPH) method. The SPH method is widely used for its convenience because it does not require meshes. However, many artificial constants such as smoothing factors are used; it is very difficult to find accurate solutions; the use may induce spurious oscillations; and, according to reference [5], the SPH method does not pass the patch test. Another widely used free surface flow calculation method is the level set approach. This method makes it easy to

capture the interface accurately, by using a function that has a zero value contour on the free surface as an identifier [6]. Despite its desirable interface and topology-capturing capability, it generally lacks the ability to conserve the conservative values: in particular, the total mass of the fluid [7].

In this thesis, we develop an improved numerical method for fluid flow problems that include interfaces and free surfaces. The formulation that we present achieves robust mass conservation of fluids without requiring any *a posteriori* mass conservation treatment. It uses an arbitrary Lagrangian-Eulerian (ALE) method with a special focus on maintaining very accurate mass conservation calculations during long response times. With the ALE method, the grid points of the calculation domain can move arbitrarily while avoiding severe mesh distortion resulting in the accurate capture of interface and boundary properties of the moving body [8, 9].

The finite element method is employed because of its strong mathematical foundation, which enables the direct evaluation of Jacobians used for the Newton-Raphson iterations [10]. For the effective solution of the Navier-Stokes equations, we adopt the flow-condition-based interpolation (FCBI) for elements [10-12]. However, to include the convective effects of moving meshes with free surfaces in the 2-dimensional analysis, we revisit the method and derive an improved FCBI scheme for an ALE formulation with triangular elements. For the capability to handle complicated three-dimensional (3-D) geometries with stability and accuracy at high Reynolds number fluid flows, the 3-D flow-condition-based interpolation for a tetrahedral MINI element is developed. The 3-D tetrahedral MINI element is used to pass the inf-sup condition, applying both the schemes of a finite volume method and a finite element method. The interpolation of the convective term is giving the upwinding for four sub regions of the 3-D tetrahedral elements. To establish the governing equations, the Petrov-Galerkin method is used at the surrounding control surfaces of control volumes. The control volumes are formed around the nodes that correspond to the degrees of freedom. The control volume, therefore, does not include only one element, but all the elements that share the node.

1.1 Overview

The present chapter introduces the Reynolds transport theorem and the derivation based on the Leibniz' rule. The Reynolds transport theorem, with a very strong mathematical foundation on the Leibniz' rule, allows one to calculate the derivative of the moving domain. The Reynolds transport theorem is a very important tool for solving free surface or multi-phase flow problems; and, in a larger scope, fluid-structure interaction problems, as it facilitates the necessary frameworks. This will be shown in more detail in section 1.2. Additionally, the simple and robust iteration method used in all the example problems provided in this thesis, Newton-Raphson, is presented with detailed explanations. This method is used in all the example problems provided in this thesis and the detailed explanations of how we used the method in the flow problems are presented.

In Chapter 2, the Arbitrary Lagrangian Eulerian (ALE) method used in this thesis is explained in a general context. As discussed in the introduction, the ALE is suitable for solving many free surface problems. This method achieves our objective of obtaining accurate dynamic behavior while using coarse meshes and introduces the ability to track the interfaces. Also, our discretization method in time and space on the interface will be presented.

As a basis for the stable and efficient calculation of the ALE solutions, we revisit the 2-dimensional triangular flow-condition-based interpolation (FCBI) to interpolate the convective terms in the Navier-Stokes equation. This is the optimal choice, again, to obtain accurate solutions, while not requiring dense meshes. The FCBI allows solving fluid problems with a large range of Reynolds numbers to be solved. More details can be found in reference [11] and Chapter 3. The extension to the free surface problems which are highly unsteady is necessary and

shown. The application methods for moving domain problems, which are free surface and multi-phase flows, are also provided in Chapter 3.

Since the most complicated free surface problems occur in 3-dimensional domains, the 3-D FCBI method is developed and presented in this thesis; the essence of the development is shown in Chapter 4. We use tetrahedral elements, which are particularly adapted to complicated 3-dimensional geometries. The developed 3-D method is based on the 1-dimensional advection-diffusion equations used in the 2-D cases. Therefore, derivations are similar to the 2-dimensional case, and the resulting method retains its efficiency. That is, it is very efficient in terms of accuracy with coarse meshes and large time steps.

The progress in capabilities for the solution of 3-D problems is very encouraging for the diverse possible applications of the method.

1.2 Reynolds transport theorem

The second fundamental theorem of calculus holds for a smooth function f defined on an open interval I. Let us define F by

$$F(x) = \int_a^x f(t)dt \tag{1.1}$$

where a and x are in I.

Then equation (1.1) satisfies at each point of I

$$\frac{dF}{dx} = f(x) \tag{1.2}$$

For the integral with an upper bound constant

$$F(x) = \int_x^b f(t)dt \tag{1.3}$$

equation 1.4 holds in a similar way.

$$\frac{dF}{dx} = -f(x) \tag{1.4}$$

If f depends on two variables, $\tilde{x}$ and t, and if the integral is a definite integral between constants a and b, equation (1.5) holds:

$$F(t) = \int_a^b f(\tilde{x},t)\,d\tilde{x} \tag{1.5}$$

We then have the relation:

$$\frac{dF(t)}{dt} = \int_a^b \frac{\partial}{\partial t} f(\tilde{x},t)\,d\tilde{x} \tag{1.6}$$

When the limits of the integration are functions of time, we use the chain rule in the material derivative.

$$\frac{dF}{dt} = \frac{\partial F}{\partial t} + \frac{\partial F}{\partial a}\frac{da}{dt} + \frac{\partial F}{\partial b}\frac{db}{dt} \tag{1.7}$$

The partial derivatives of F with respect to a and b can be written explicitly as follows:

$$\frac{\partial F}{\partial a} = \lim_{\Delta a \to 0} \frac{\int_{a+\Delta a}^{b} f(\tilde{x},t)\,d\tilde{x} - \int_a^b f(\tilde{x},t)\,d\tilde{x}}{\Delta a} = -\lim_{\Delta a \to 0} \frac{\int_a^{a+\Delta a} f(\tilde{x},t)\,d\tilde{x}}{\Delta a} = -f(a,t) \tag{1.8}$$

$$\frac{\partial F}{\partial b} = \lim_{\Delta b \to 0} \frac{\int_a^{b+\Delta b} f(\tilde{x},t)\,d\tilde{x} - \int_a^b f(\tilde{x},t)\,d\tilde{x}}{\Delta b} = \lim_{\Delta b \to 0} \frac{\int_b^{b+\Delta b} f(\tilde{x},t)\,d\tilde{x}}{\Delta b} = f(b,t) \tag{1.9}$$

Therefore, equation 1.7 is rewritten as equation 1.10 below

$$\frac{dF}{dt} = \int_{a(t)}^{b(t)} \frac{\partial}{\partial t} f(\tilde{x},t)\,d\tilde{x} + f(b,t)\frac{db}{dt} - f(a,t)\frac{da}{dt} \tag{1.10}$$

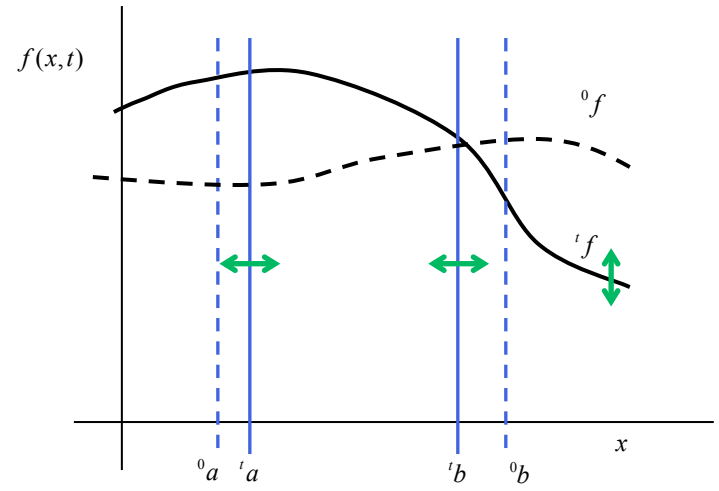

(Fig. 1.1) Illustration of an unsteady function defined in a moving domain

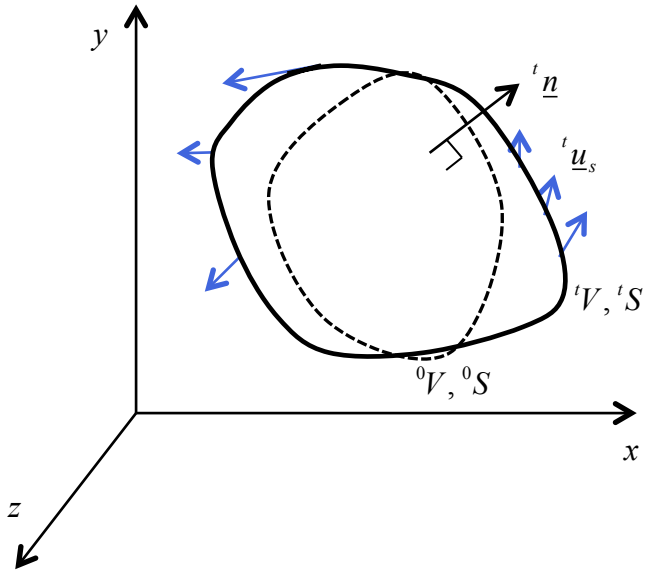

(Fig. 1.2) Three-dimensional moving control volume

Figure 1.1 illustrates the concept of moving function and boundaries in equation (1.10). At the initial time step, the limits were ${}^0a$ and ${}^0b$, and the function was $f(x,0) = {}^0f$. The moving boundaries at the current time step are now ${}^ta$ and ${}^tb$, and the function has the value of $f(x,t) = {}^tf$. The time differentiation of the integral with moving boundaries can be formulated

using equation (1.10), which is known as the "Leibniz' rule for the differentiation of integrals", and the concept of the rule can be easily extended to 3-dimensional spaces. Let us now consider a 3-dimensional field where the integrand is a function of space and time, $F(x, y, z, t)$.

The control volume is denoted by V and the control surface by S. The normal direction on the control surface is $\underline{n}$, the velocity of the control surface is $\underline{u}_S$ and the time of all variables is indicated by the left superscripts. The time rate of change of the value f in the control volume V is required to address the 3-dimensional Leibniz' rule. For the 3-dimensional domain, the boundaries of the integrals become control surfaces.

Therefore, equation (1.10) is rewritten for the 3-dimensional integration as follows:

$$\frac{d}{dt}\int_{t_V} f \, dV = \int_{t_V} \frac{\partial f}{\partial t} \, dV + \int_{t_S} f(\underline{u}_S \cdot {}^t\underline{n}) \, dS \qquad (1.11)$$

The control volume theory of the moving fluid domain is derived from equation (1.11) and is the basis of the Reynolds transport theorem, which is applied to derive the arbitrary Lagrangian-Eulerian formulation for the FCBI methods.

The frame of observation for ALE does not require the meshes to be stationary, nor to move with the same velocity as the material points. For this reason, ALE is greatly favored in the analysis of free surface or multi-phase flow problems. In other words, since flow problems with interfaces require to accurately capture the interfaces, the Lagrangian perspective is naturally adopted to flow problems at the interfaces. However, the interior domains are not required to follow the Lagrangian perspective, freeing our analysis from its limitations –e.g., mesh distortion or mesh entanglements – since the ALE control volume concept will work with the concept of the mesh's motions. We therefore need to pay attention to the analysis of arbitrarily-moving control volumes, applying Leibniz rule in mathematical aspects and the Reynolds transport theorem in mechanics aspects.

The general representation of flow problems using arbitrarily-moving control volumes is accomplished by substituting the value $f = \rho$ (see equations (1.12) and (1.13)), where ρ is the

mass density, for the integral form of the mass conservation equation and $f = \rho \underline{u}$ (see equations (1.15) and (1.16)) for the conservation of momentum, where $\underline{u}$ is the velocity vector. We first write the two following equations:

$$\frac{d}{dt}\int_{t_V} \rho \, dV = \int_{t_V} \frac{\partial \rho}{\partial t} \, dV + \int_{t_S} \rho(\underline{u}_S \cdot {}^t\underline{n}) \, dS \tag{1.12}$$

$$\frac{\partial \rho}{\partial t} + \nabla \cdot (\rho \underline{u}) = 0 \tag{1.13}$$

Applying the Gauss theorem and the relation (1.13) to equation (1.12) gives the mass conservation equation for the arbitrarily-moving control volume:

$$\frac{d}{dt}\int_{t_V} \rho \, dV = -\int_{t_S} \rho(\underline{u} \cdot {}^t\underline{n}) \, dV + \int_{t_S} \rho(\underline{u}_S \cdot {}^t\underline{n}) \, dS \tag{1.14}$$

The differential form of the momentum equation is given by

$$\frac{\partial \rho \underline{u}}{\partial t} + \nabla \cdot (\rho \underline{u}\underline{u} + \underline{\tau}) - \rho \underline{g} = 0 \tag{1.15}$$

where $\underline{g}$ is the gravitational acceleration and $\underline{\tau}$ is the stress tensor given by $\underline{\tau} = -pI + \mu(\nabla \underline{u} + \nabla \underline{u}^T)$. In the latter expression, μ is the dynamic viscosity and p is the pressure. Similarly, the momentum conservation equation is derived. Applying equation (1.15) into equation (1.16) gives equation (1.17)

$$\frac{d}{dt}\int_{t_V} \rho \underline{u} \, dV = \int_{t_V} \frac{\partial \rho \underline{u}}{\partial t} \, dV + \int_{t_S} \rho \underline{u}(\underline{u}_S \cdot {}^t\underline{n}) \, dS \tag{1.16}$$

$$\frac{d}{dt}\int_{t_V} \rho \underline{u} \, dV + \int_{t_S} ([\rho \underline{u}(\underline{u} - \underline{u}_S) - \underline{\tau}] \cdot {}^t\underline{n}) \, dS = \int_{t_V} \rho \underline{g} \, dV \tag{1.17}$$

1.3 Newton-Raphson method

The proposed scheme for free surface or multi-phase problems is highly nonlinear. There are many approaches to solve nonlinear finite element problems. However, the Newton-Raphson iteration is considered to be the key to solving finite element algebraic equations with nonlinearity [13]. When applied properly, Newton-Raphson achieves quadratic convergence [14,15]. The iteration is started with an initial guess of the solution, which means it is an open method that can lead to difficulty in convergence. If the initial roots, initial nodal velocities or pressure in free surface problems are not guessed well, the solution can experience convergence difficulties [16]. However, we presume that the benefit of the Newton-Raphson method exceeds the difficulty when the initial condition of the flow can be calculated. For example, when we simulate water sloshing in a moving tank, we usually assume that the initial condition is stationary. As a result, the initial guess utilizes zero velocities and the static hydrodynamic pressure distribution.

In fluid problems, momentum and mass fluxes are written as an internal function ($^{t+\Delta t}F(\underline{U})$) of a vector $\underline{U}$ of nodal velocities and pressures, and the source term is an external loading vector ($^{t+\Delta t}R(\underline{U})$). Symbol Δt refers to the time increment. The details of the construction of the fluxes and the loading vectors will be provided in the next chapter.

The objective is to find the nodal velocities and pressure vector $\underline{U}^*$ that satisfies equation (1.18) [16].

$$^{t+\Delta t}F(\underline{U}^*) - {}^{t+\Delta t}R(\underline{U}^*) = 0 \qquad (1.18)$$

The flux and the loading are always evaluated with the previous iterations at the current time step. For free surface problems, the difficulty lies in the undetermined control volume configurations. They involve the velocities of the mesh motion, which will frequently be referred to as mesh velocity in this thesis. Control volume configurations are also dependent on the time integration of the mesh velocities.

The Newton-Raphson iteration method is based on the Taylor series expansion of equation (1.18) in terms of the differentiations with respect to $\underline{U}$.

$$F(\underline{U}^*) = F({}^{t+\Delta t}\underline{U}^{(i-1)}) - {}^{t+\Delta t}R + \frac{\partial F({}^{t+\Delta t}\underline{U}^{(i-1)})}{\partial \underline{U}}(\underline{U}^* - {}^{t+\Delta t}\underline{U}^{(i-1)}) + \text{higher-order terms} \tag{1.19}$$

where i is the iteration number.

In finite element problems, if the derivative term of equation (1.19) is calculated at each iteration, the matrix $\frac{\partial F({}^{t+\Delta t}\underline{U}^{(i-1)})}{\partial \underline{U}}$ is called the tangent stiffness matrix (see figure 1.3).

$${}^{t+\Delta t}K^{(i-1)} = \left[\frac{\partial F(\underline{U})}{\partial \underline{U}}\right]\Bigg|_{{}^{t+\Delta t}\underline{U}^{(i-1)}} \tag{1.20}$$

When the iteration number i is 1, the stiffness matrix is evaluated by using the converged values at the previous time step.

$${}^{t+\Delta t}K^{(0)} = \left[\frac{\partial F(\underline{U})}{\partial \underline{U}}\right]\Bigg|_{{}^{t}\underline{U}} \tag{1.21}$$

Due to the method used in equation (1.21), the time step size of the scheme should not be too large. Since the tangent stiffness matrix of the first iteration is constructed with the variables of the previous time step, using a large time step size can induce difficulty in convergence. Moreover, when the control volume moves with time, the mass conservation function contains terms that are not a function of the velocities only but also of the time rate of change of the volume size and mesh velocities. Therefore, the mesh motion should not be completely arbitrary. One more important difference from the steady case is the involvement of the mesh velocity to calculate the convection velocity term in momentum fluxes. A good choice of mesh velocity as a function of the nodal velocities is a proper way to accelerate the convergence.

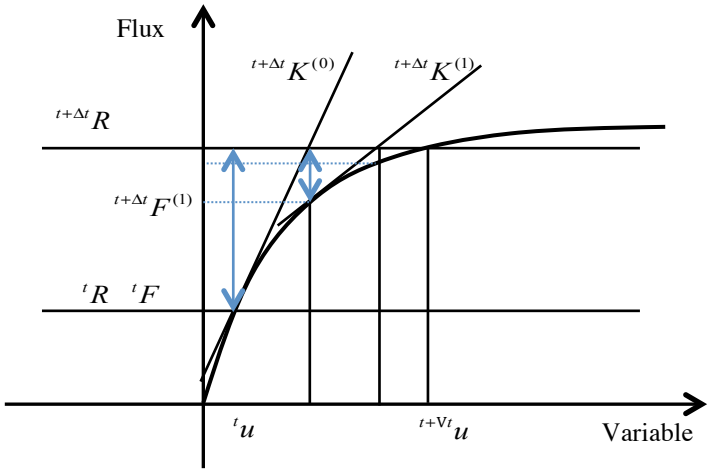

(Fig. 1.3) Graphical illustration of Newton-Raphson iteration for a single-degree of freedom problem, taken from [16]

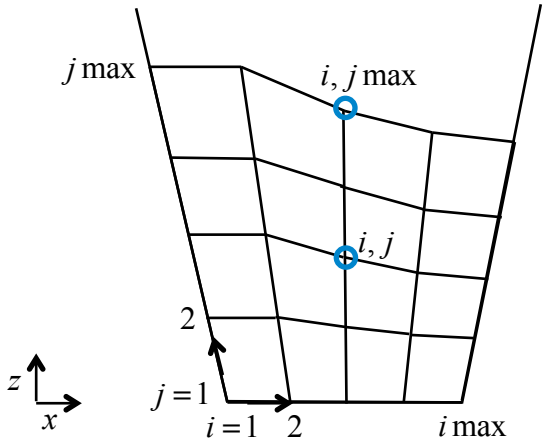

(Fig. 1.4) Illustration of the mesh velocity mechanism

As will be explained from equation (2.1), the mesh velocity $\underline{u}_m$ at the free surface is a function of the fluid velocity:

$$\underline{u}_m^{(i.j\max)} = \underline{u}_m^{(i.j\max)}(\underline{u}^{(i,j\max)}) \tag{1.22}$$

More details will be provided in Section 2.3.

In this thesis, mesh velocities are chosen to be a function of the velocities at the free surface (or interface) and nodal coordinates (see figure 1.4):

$$\underline{u}_m^{(i.j)} = \left(\frac{z^{(i,j)}}{z^{(i,j\max)}} \right) \times \underline{u}_m^{(i.j\max)} \tag{1.23}$$

Therefore, the mesh velocity is a function of the velocity at the interface.

$$\underline{u}_m^{(i.j)} = \underline{u}_m^{(i.j)}(\underline{u}^{(i,j\max)}) \tag{1.24}$$

As a result, each flux equation is a function of the nodal velocities and nodal pressures of the free surface. We therefore write the flux:

$$F(\underline{u}, p) = \tilde{F}(\underline{u}, \underline{u}_m, p) \tag{1.25}$$

where the mesh velocity is a function of the velocities at the free surface or interface $\underline{u}_m = \underline{u}_m(\underline{u})$

$$\frac{\partial F}{\partial \underline{U}} = \frac{\partial \tilde{F}}{\partial \underline{U}} + \frac{\partial \tilde{F}}{\partial \underline{u}_m} \frac{\partial \underline{u}_m}{\partial \underline{U}} \tag{1.26}$$

$$^{t+\Delta t}\underline{K}^{(i-1)} (\,^{t+\Delta t}\underline{U}^{(i)} - \,^{t+\Delta t}\underline{U}^{(i-1)}) = \,^{t+\Delta t}\underline{R} - \,^{t+\Delta t}\underline{F}^{(i-1)} \tag{1.27}$$

The linearized equation at each iteration step gives the unknown $^{t+\Delta t}\underline{U}^{i}$. The iteration is repeated until the difference between the current iteration's root and the previous iteration's root is within a tolerance ε. In this thesis, the default for this tolerance has been set as 10^{-5}.

$$\frac{\left\| \,^{t+\Delta t}\underline{U}^{(i)} - \,^{t+\Delta t}\underline{U}^{(i-1)} \right\|_2}{\left\| \,^{t+\Delta t}\underline{U} \right\|_2} \leq \varepsilon \tag{1.28}$$

Chapter 2

Arbitrary-Lagrangian-Eulerian formulation

In this chapter, we present a finite element formulation, called the arbitrary Lagrangian Eulerian (ALE) formulation, in order to solve free surface or multiphase flow problems. Since ALE allows the mesh to move with relative freedom, the velocity of the mesh inside the fluid domain is neither the velocity of the material points (Lagrangian method), nor zero. The latter makes elements fixed, as in the Eulerian formulation. One well-known example is the immersed boundary method (IBM). With ALE, the nodes on the boundaries or interfaces move along material lines at the interfaces. Since it uses a mesh that can move freely inside the domain and accurately track the interfaces, the ALE formulation is chosen for this thesis.

2.1 Governing equations

The mass conservation equation of ALE is very sensitive to matching because of the nonlinearity induced by the continuously moving computational domain at each iteration and each time step. To satisfy mass conservation, there is one important criterion: the flow should not flow through the free surface interface (equation (2.1)). Therefore, we have

$$(\underline{u}-\underline{u}_m)\cdot\underline{n}^f=0 \quad \text{on} \quad S^f\times[0,T] \tag{2.1}$$

$$\frac{\partial \rho}{\partial t} + \nabla \cdot \rho \underline{u} = 0 \qquad \text{in} \qquad V^f \times [0,T] \tag{2.2}$$

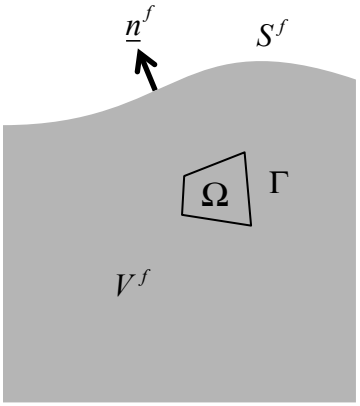

(Fig. 2.1) Free surface and related variables

where $\underline{n}^f$ is the normal vector on the free surface, S^f is the free surface and V^f denotes the fluid domain (see figure 2.1). Also, $\underline{u}_m$ is the velocity of an underlying medium of observation, which in ALE analysis, is the same as the mesh velocity.

In the fluid domain, we name Ω the moving control volume, and Γ the control surface that encloses the control volume. Equation (2.1) is a very straightforward and important kinematic relation that must be included to completely satisfy mass conservation and correctly construct the shape of the interface. The mass conservation equation (2.2) is often used for compressible flows. This is not to say that we are solving a compressible flow, but in a sense the density from an Eulerian perspective, as in equation (2.2), changes due to the free surface motion through the fixed point in space. An easier depiction of why we consider the differential mass conservation equation should include the time rate change of the density is provided in figures 2.2 and 2.3. Many sources in the literature, including reference [17], state only that the incompressibility equation $\nabla \cdot \underline{u} = 0$ needs to be satisfied. However, the statement is incorrect because the density changes along time at a fixed spatial point.

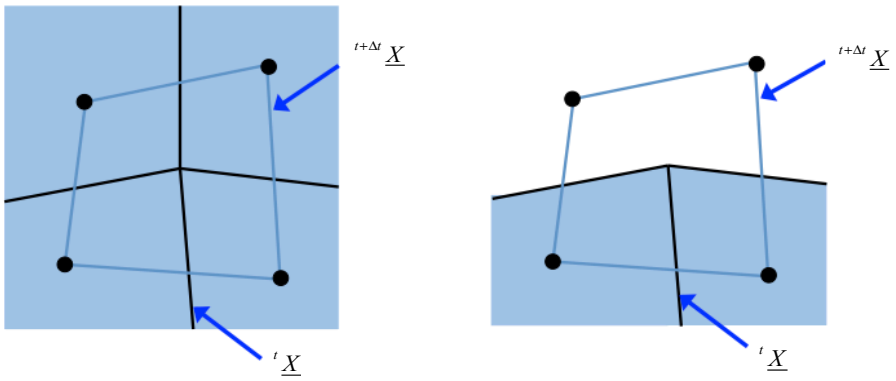

(a) (b)

(Fig. 2.2) Configuration change in time:
(a) mesh configuration of interior elements
(b) mesh configuration of interface elements

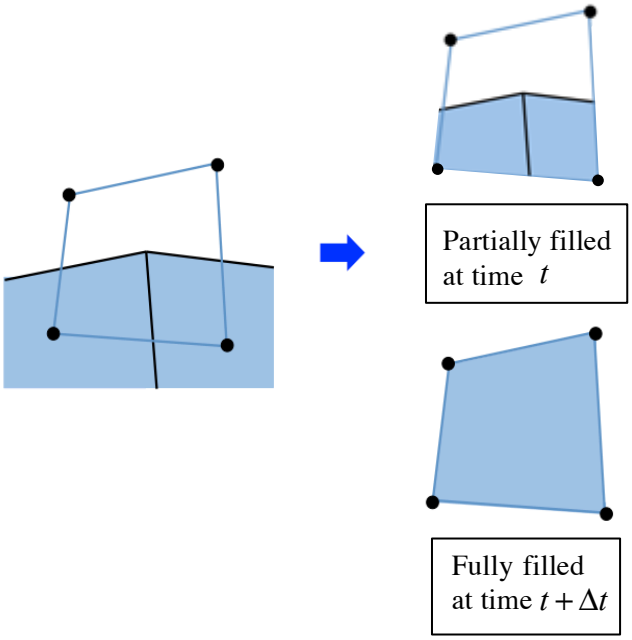

(Fig. 2.3) Average density change in time due to the level of filling of the interface control volumes

Based on the Reynolds transport theorem introduced in section 1.2, the weak forms of the mass conservation equation in a moving control volume maintaining a constant density can be written as follows:

$$\frac{d}{dt}\int_{\Omega}\rho d\Omega+\int_{\Gamma}\rho(\underline{u}_c\cdot\underline{n})d\Gamma=0 \tag{2.3}$$

where $\underline{u}_c$ denotes the convective velocity which satisfies

$$\underline{u}_c=\underline{u}-\underline{u}_m \tag{2.4}$$

Applying the relation (2.4), the equation is rewritten as:

$$\int_{\Gamma}\rho(\underline{u}\cdot\underline{n})d\Gamma=-\frac{d}{dt}\int_{\Omega}\rho d\Omega+\int_{\Gamma}\rho(\underline{u}_m\cdot\underline{n})d\Gamma \tag{2.5}$$

If the control volume is located in the interior region, it does not include an interface and the right hand side of equation (2.5) is zero. This is so because, as depicted in Figure 2.2 (a), the net flux at any time of observation has to be zero. However, if the control volume intersects the interface, the right hand side is non-zero and highly nonlinear due to the mesh motion: i.e., the mesh velocity, the control volume and the surrounding surfaces must be updated at each iteration.

The momentum equation is also derived using the Reynolds transport theorem. The weak form of the unsteady incompressible Navier-Stokes equation is

$$\frac{d}{dt}\int_{\Omega}\rho\underline{u}\ d\Omega+\int_{\Gamma}\rho(\underline{v}\underline{u}_c+pI-\mu(\nabla\underline{u}+\nabla\underline{u}^T))\cdot\underline{n}\ d\Gamma=\int_{\Omega}\rho\ d\Omega\ \underline{g}+\int_{S}\underline{F}^S dS \tag{2.6}$$

where $\underline{g}$ is the gravitational acceleration vector and $\underline{F}^S$ is the external surface traction on the area S. Note that the inertial term should account for the time rate of change of control volume size and the acceleration when it is differentiated by parts after finite element discretization. The details will be provided next in section 2.2. The notation of velocity in the convection term is written $\underline{v}$ and uses different interpolations for stability. This will be discussed in more detail in sections 3.1 and 4.1.

2.2 Time integration method

For the mesh update and the time differentiation of the flux integrals that appear in the governing equations, the trapezoidal rule is used. The trapezoidal rule has the advantage of being an implicit method and does not suffer from numerical dissipation. Therefore, equation (2.3) can be expressed with trapezoidal time discretization as:

$$\frac{\Delta t}{2}\left[\int_{{}^{t+\Delta t}\Gamma}{}^{t+\Delta t}\underline{u}_c \cdot \underline{n}\, d\Gamma + \int_{{}^{t}\Gamma}{}^{t}\underline{u}_c \cdot \underline{n}\, d\Gamma\right] = -({}^{t+\Delta t}\Omega - {}^{t}\Omega) \tag{2.7}$$

The effect from using other time discretization methods, such as the "forward Euler method" and the "backward Euler method" in multi-phase flow, is provided in section 3.2.4 to verify the effectiveness of this method.

When it comes to the application of the trapezoidal rule to the unsteady term of the Navier-Stokes equation, equation (2.6) should account for both the change in volume, which is dependent on the mesh's velocity, and the changes in velocity along time. Time differentiation is more straightforward, and should be done after discretization. This will be discussed after the introduction of the finite element discretization (see equation (4.42) for more details). We recall the relation:

$$\frac{d}{dt}\int_{\Omega}\rho\underline{u}\, d\Omega \rightarrow \dot{M}\underline{\hat{u}} + M\underline{\hat{a}} \tag{2.8}$$

Symbols M and $\dot{M}$ refer to the mass matrix and the time rate of change of the mass matrix, and $\underline{\hat{u}}$ and $\underline{\hat{a}}$ are the nodal velocity and acceleration, respectively.

2.3 Mesh motions on the interface

Mesh motions utilize the mesh velocities at the current and at the previous time step. Configuration of the mesh must be evaluated at each iteration. This is the main difficulty of free surface problems compared to fluid problems without interfaces.

Therefore, proper time advancing method is crucial. We use the following formulation:

$$ {}^{t+\Delta t}\underline{x} = {}^{t}\underline{x} + \frac{\Delta t}{2}({}^{t}\underline{u}_m + {}^{t+\Delta t}\underline{u}_m) \tag{2.9} $$

After updating the mesh with equation (2.9), the control volumes, the control surfaces and the normal vectors of the control surfaces are calculated in order to estimate and evaluate the fluxes. Since the elements around fluid interfaces should include the interface surfaces (see figure 3.3), mesh velocities around the interfaces must satisfy the condition that the density inside the control volumes be kept constant along time. Also, to avoid mesh entanglement and severe mesh distortion, the mesh must be guided by a preferred (prescribed) direction $\underline{m}$.

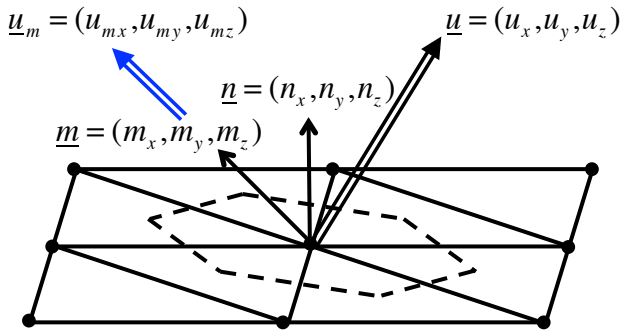

(Fig. 2.4) Variables on the free surface interface in 3-dimensional domains

In figure 2.4, we depict a free surface and the associated vectors. The solid lines are element defining lines and the dotted lines are the control volume/surface defining lines. The vectors are related by the equations.

$$\underline{u} \cdot \underline{n} = \underline{u}_m \cdot \underline{n} \tag{2.10}$$

$$(\underline{u}_m - \underline{u}_w) = \beta \underline{m} \tag{2.11}$$

where β is a parameter to be determined.

Equation (2.10) is analogous to equation (2.1). The vector denoted $\underline{u}_w$ is the averaged fluid domain's velocity or a representative overall domain velocity. For the rigid container, $\underline{u}_w$ is simply the excitation velocity of the container.

We define the nodal unit normal vector $\underline{n}$ as [18]:

$$\underline{n} = \frac{\overline{\underline{n}}}{|\overline{\underline{n}}|} \tag{2.12}$$

where $\overline{\underline{n}}$ is the area-weighted average:

$$\overline{\underline{n}} = \frac{\sum_{i=1}^{N} A_i \underline{n}_i}{\sum_{i=1}^{N} A_i} \tag{2.13}$$

In equation (2.13), N is the total number of elements forming the control surface on the free surface. Once $\underline{n}$ is numerically defined, equations (2.10) and (2.11) can be explicitly written and solved as a system of four equations and four unknowns. We thus obtain the expressions of the three components of $\underline{u}_m$.

Chapter 3

Two-dimensional FCBI of single phase and multi-phase ALE problems

In this chapter, we briefly recapitulate the 2-dimensional FCBI methods, which are adjusted for the 2-D free surface and multi-phase flows. Various example problems follow and demonstrate the superiority of the FCBI method because its mathematical formulations are based on a physical description of the problems.

3.1. Two-dimensional FCBI formulation

For 2-dimensional problems, triangular FCBI elements are used. The steady flow problem solutions were developed by H. Kohno and K. J. Bathe [11]. With the choice of triangular elements, we satisfy the inf-sup condition, by using 3 pressure degrees of freedom for pressure and 4 degrees of freedom for velocity. The former correspond to the 3 corner nodes of the triangle, while the latter correspond to the 3 corner nodes and the barycenter node. A detailed understanding of this choice is presented in reference [11].

The governing equations of the weighted unsteady incompressible two-dimensional fluid flow are written as follows:

$$\frac{d}{dt}\int_{\Omega} w\,(\rho \underline{u})d\Omega + \int_{\Gamma} w\,(\rho \underline{v}\underline{u}_c - \underline{\tau}(\underline{u},p))\cdot \underline{n}\; d\Gamma = \int_{\Omega} w\,(\rho \underline{g})d\Omega \tag{3.1}$$

$$\int_{\Gamma} q\,(\rho \underline{u}\cdot \underline{n})\; d\Gamma = -\frac{d}{dt}\int_{\Omega} q\;\rho\; d\Omega + \int_{\Gamma} q\,(\rho \underline{u}_m \cdot \underline{n})\; d\Gamma \tag{3.2}$$

, where $\underline{\tau} = \underline{\tau}(\underline{u},p) = -pI + \mu(\nabla \underline{u} + \nabla \underline{u}^T)$ is the stress tensor. The objective is to find $\underline{u} \in U_h$, $\underline{v} \in V_h$ and $p \in P_h$ such that all $w \in W_h$ and $q \in Q_h$ satisfy equations (3.1) and (3.2). The trial functions in space U_h and P_h are the usual functions, linear in space. However, the trial functions in V_h must be calculated at each iterations. The weight functions in the spaces W_h and Q_h are simply step functions. That makes this finite element formulation similar to the finite volume method. One more thing to note regarding the ALE formulation using FCBI elements is that the convective velocity of equation (3.1) utilizes usual linear interpolations, i.e. $\underline{u}_c \in U_h$ and the mesh velocity in equation (3.2) also uses linear interpolations, $\underline{u}_m \in U_h$.

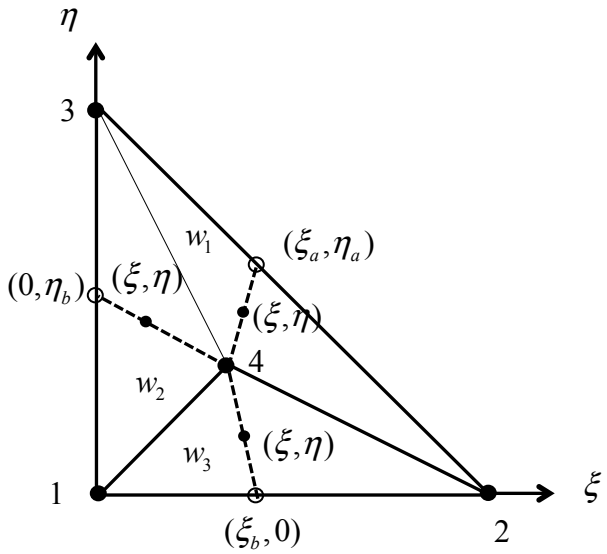

(Fig. 3.1) Variables used for constructing the interpolations in V_h

The methodology of 2-D FCBI uses the 1-D advection-diffusion equations and coordinates (ξ_a, ξ_b, η_a, η_b), which are the intersections of the element sides of each of the 3 sub-regions (w_1, w_2, w_3) of the triangular MINI elements and lines from the center of the element and the

flux calculation points (ξ,η) (see figure 3.1). More details on the interpolation functions of 2-D FCBI are provided in detail in reference [11].

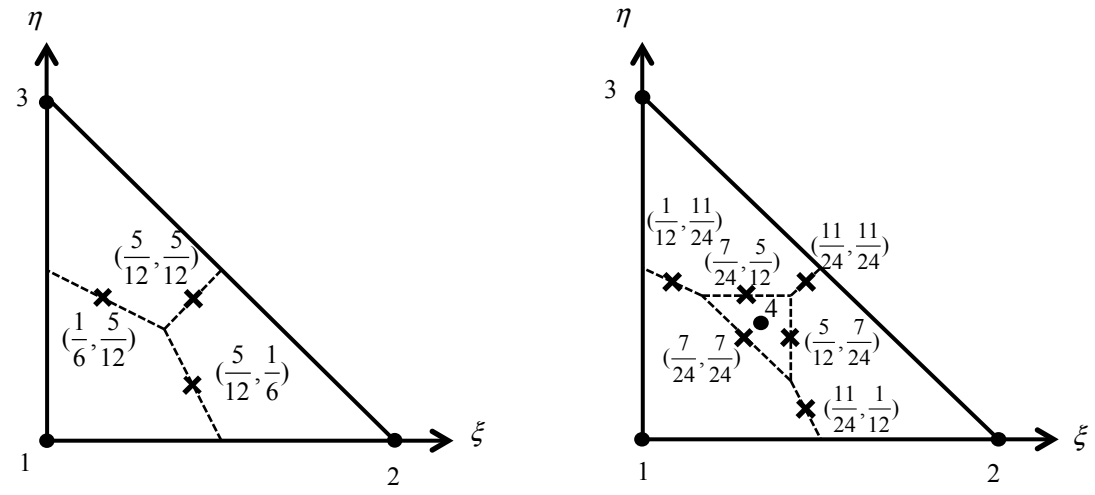

(a) (b)

(Fig. 3.2) Flux calculation points: (a) segment in space W_h (b) segment in space Q_h

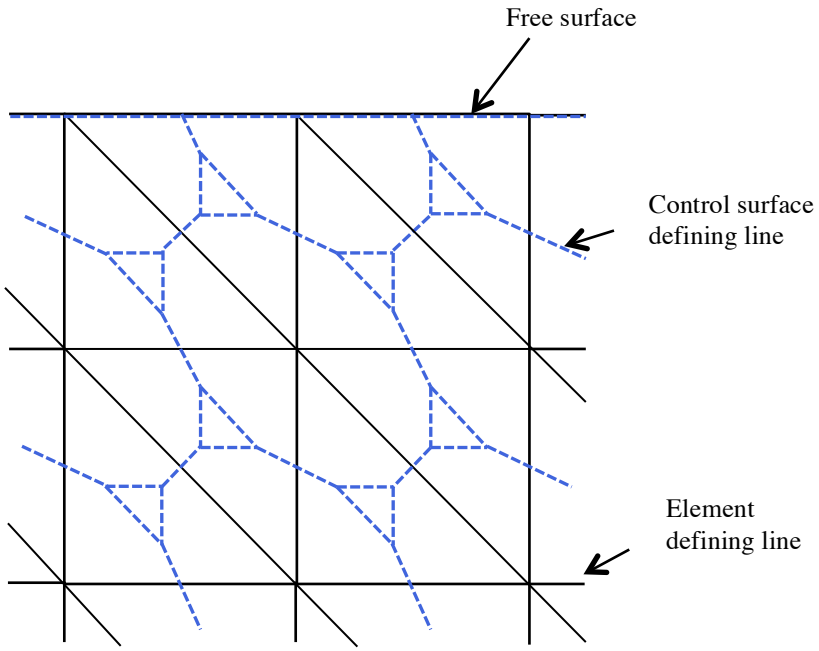

(a)

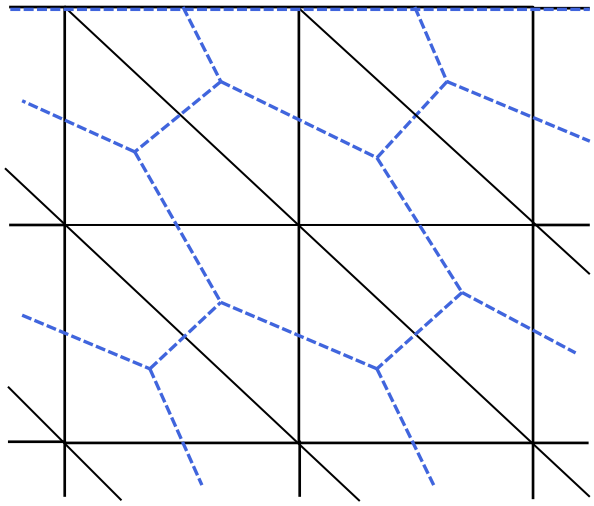

(b)

(Fig. 3.3) Typical control volumes including elements near the interface
(a) control volumes in space W_h
(b) control volumes in space Q_h

The usual control volumes are shown in figures 3.3a and 3.3b. The control volumes are formed with the method represented in figures 3.2a and 3.2b.

Note that the control volume defining lines overlap with the element defining line on the free surface. Also, the element defining lines are identical to the free surface lines. This is one of the benefits of the ALE method that captures free surface accurately with element lines. This also ensures that density inside the control volumes remains constant throughout the computation time for free surface flows. Although this is not exactly the Lagrangian approach of free surface particles, equation (2.1) ensures that the free surface interface is accurately captured without the limitations of a purely Lagrangian approach, such as mesh entanglements.

3.2 Numerical examples of 2-D problems

We here apply the 2-D FCBI method and validate it using structured meshes (see figure 3.3). The accuracy of mass conservation for long-duration calculations or highly distorted meshes is the main focus of this section. The suggested scheme is also used to solve a multi-phase flow problem. All example problems are viscous-flow problems. The FCBI method uses element Reynolds numbers and requires the element Reynolds number to be finite, i.e. not infinitely high as in inviscid flow problems (see Appendix B).

3.2.1 Free surface problem with a small sloshing amplitude

The first test case is a well-known example of free oscillation in a 2-D rectangular tank (see figure 3.4). The flow is calculated with simplified geometrical values and a gravitational acceleration value. The initial small amplitude sinusoidal height is given as follows:

$$\eta(x) = a\sin(\frac{\pi}{2b}x) \tag{3.3}$$

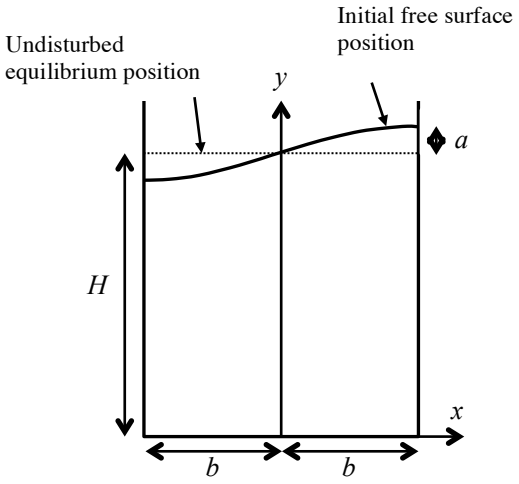

(Fig. 3.4) Problem definition of small amplitude sloshing

The condition is the same as in the references [6,17]. We compare our results with those two studies. The graph in figure 3.5 is the time history of heights at the left wall and the right wall. The width of the tank wall is 2 and the height, measured from $y = 0$ to the equilibrium undisturbed height is 1. The initial sinusoidal amplitude a is 0.01. The outside pressure at the free surface is kept at atmospheric pressure. The dynamic viscosity is given as 0.01 with a gravitational acceleration of 1. The mesh uses 392 triangular elements in total and 617 nodal points. The time step size is 0.005.

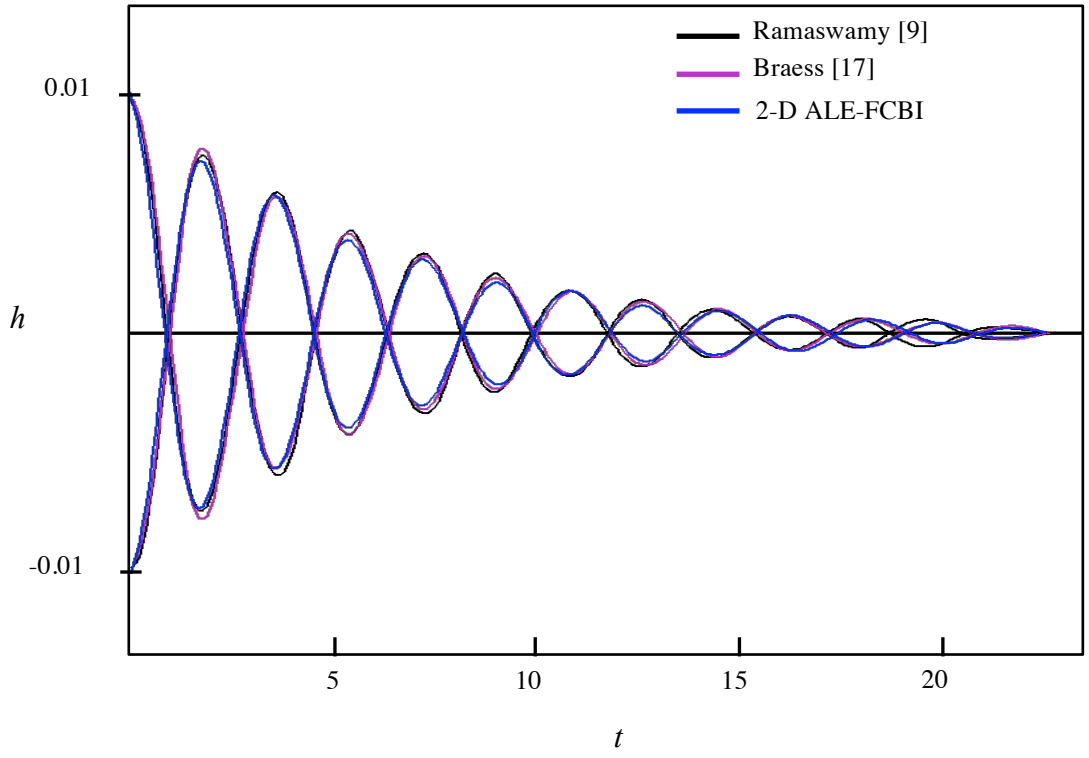

(Fig. 3.5) The results of the left and right wall height

Neither experimental results nor analytical solutions to this problem are available but figure 3.5 shows that the results conform with two other references that are solving the problem with ALE.

3.2.2 Free surface problem with large mesh distortion

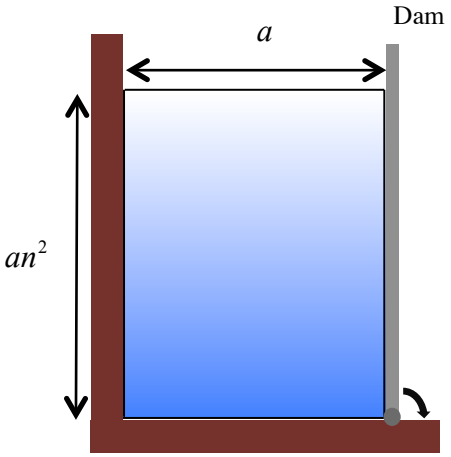

(Fig. 3.6) Problem definition of dam break example

Reference [19] presents a simple dam-break example, which consists of letting a water column collapse; this reference provides experimental data. Reference [20] gives the calculation result, allowing a comparison to the 2-D FCBI results. The problem uses water as the fluid. Initially, the water column stays stationary in the confined area in the dam and the no-slip container. At time $t = 0$, the water column starts to collapse due to the sudden removal of the dam. This problem is often used for comparing free surface calculation schemes. Also, it is a relevant problem because it leads to large deformations of the domain and to much distorted meshes. Proper fluid calculation schemes should yield accurate solutions despite the severe mesh distortion. The non-dimensional values measured for comparisons are the non-dimensional distance Z and the non-dimensional time T.

$$Z = z / a \tag{3.4}$$

$$T = nt\sqrt{\frac{g}{a}} \tag{3.5}$$

The value z is the distance from the stagnation point located at the lower left corner (see figure 3.6) to the advancing front of fluid; Z is normalized with the initial width of the water column. The initial height is defined by the geometrical variable n, which can be understood as the square

root of the aspect ratio. The material property used is that of water at room temperature and the ambient substance is air. As stated in reference [19], the density ratio of water to air is high; therefore we assume in this example a single-phase flow. Although reference [19] pointed out that the result is not very sensitive to the viscosity, we still use water viscosity of $\mu = 0.001 N \cdot \sec$ for all simulations. We use the gravitational acceleration value g=9.81m/sec2. For simplicity, we used 14 quadrilaterals for horizontal and vertical directions that contain two triangular elements. Therefore, about 400 elements (14x14x2) are used (see figure 3.9) which are fewer than 24x16 (=444) quadrilateral elements for the example of reference [20] with aspect ratio variable $n = 1$. Although reference [19] provides both the rectangular and semicircular container case, we performed the calculation for the rectangular tank for simplicity. The width of this dam experiment is $a = 5.715\text{cm}$. Since reference [19] assumes that the motion starts at non-dimensional time 0.01 after the release of the dam, we applied a non-dimensional time gap of 0.01.

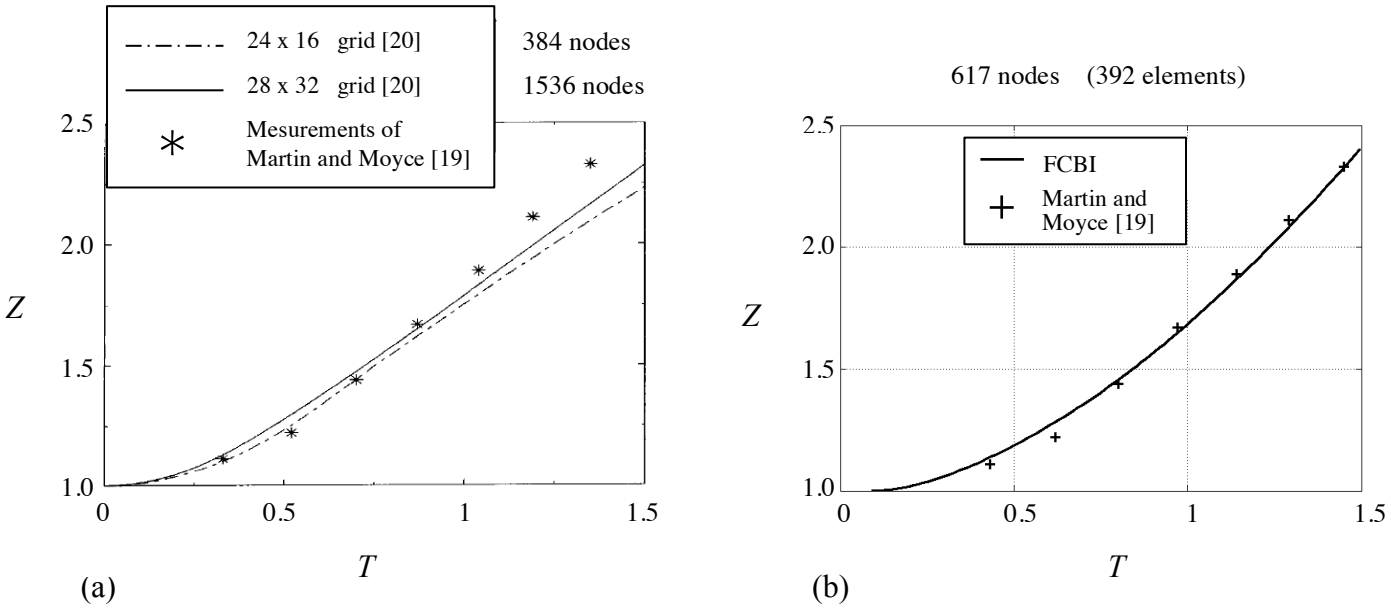

(Fig. 3.7) Time history of Z when n=1:
(a) results provided by reference [20] (b) results using FCBI ALE

As the comparison between the reference and the 2-D FCBI ALE method shows, the FCBI method achieves very accurate solutions with fewer node numbers. This is made possible by its capability of accurately capturing the interface configuration and effectively calculating the fluxes around the control surfaces. Figure 3.7 corresponds to an aspect ratio of 1 and figure 3.8 corresponds to an aspect ratio of 2 ($n=\sqrt{2}$), i.e. the column is twice as long in height than in width. Agreement with the experimental data is also observed to be excellent. Results using several mesh sizes are shown in figure 3.8. The method does not require many elements to calculate very accurate answers and accurate dynamic flow response is achieved regardless of the mesh size. The good agreement of these results is meaningful because it also verifies that the method handles severe mesh distortion very well, as illustrated by figure 3.9 in which we show the mesh lines at several times (see figure 3.9).

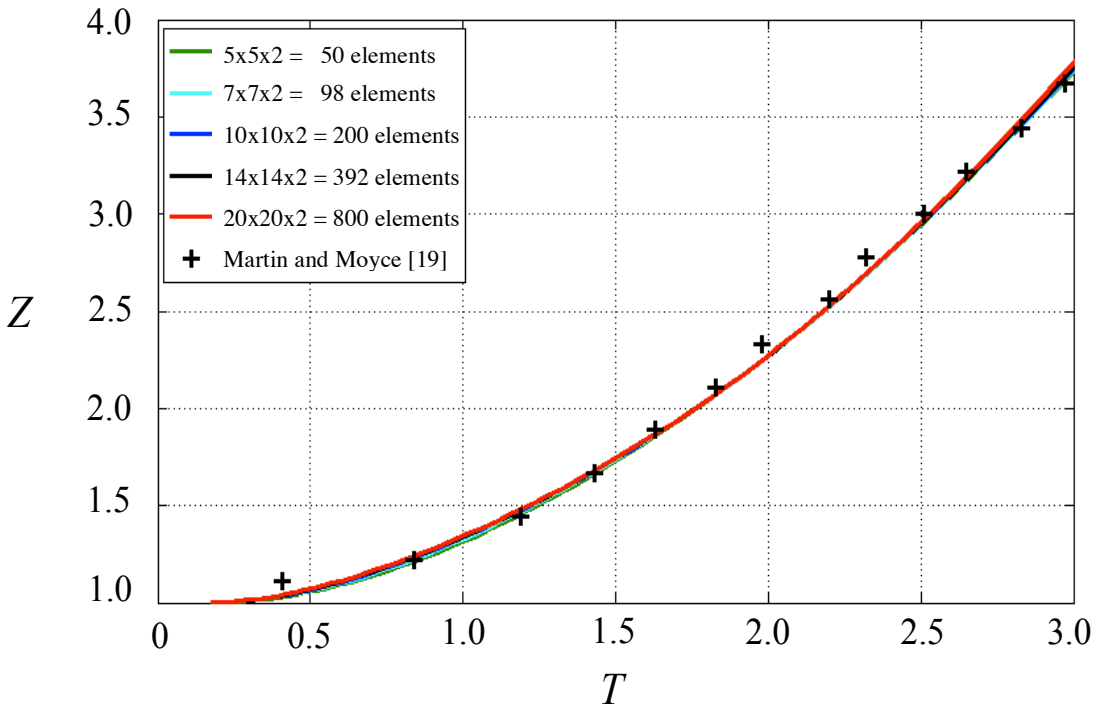

(Fig. 3.8) Time history of Z with different mesh sizes

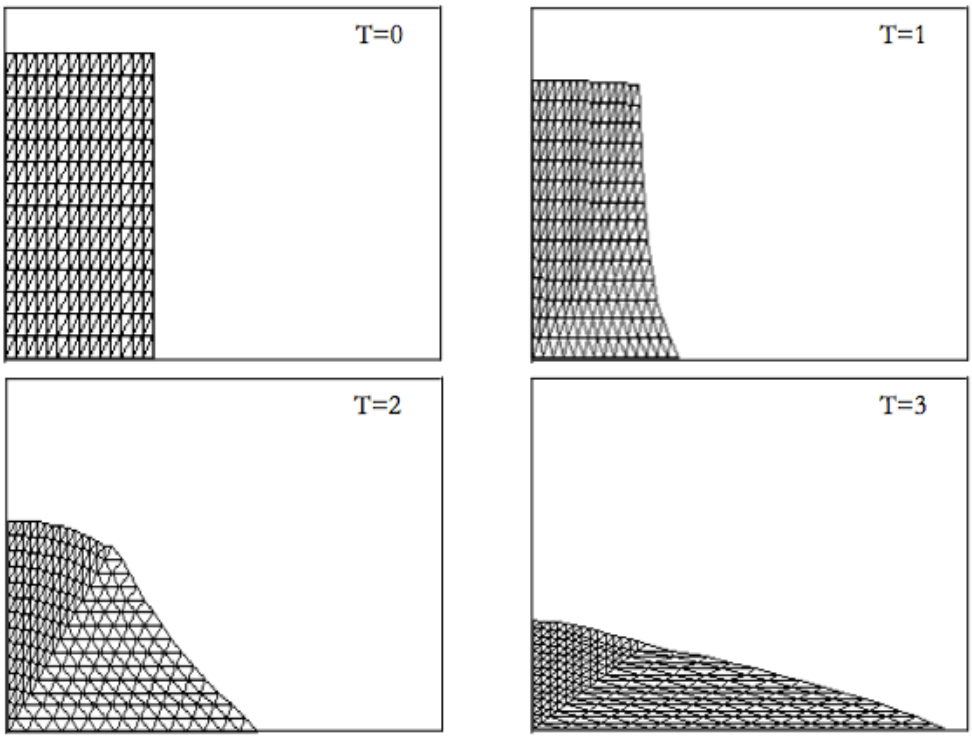

(Fig. 3.9) Snap shot of meshes at four different times
At T=3, the mesh is heavily distorted but this does not affect the accuracy of the results.

3.2.3 Sloshing problem with long time duration

The goal of the numerical example presented in this section is to check if the scheme conserves mass accurately throughout the long computational time. Mass conservation is a good way to check the validity of free surface or multi-phase flow solution schemes, since it has to remain constant in time if there is no mass source or sink. The trapezoidal tank shown in figure 3.10 is excited with a velocity $\sin^2(\omega t)$. This example is chosen because we want to have a smooth excitation velocity and also to cover large spatial domains during calculations. Figure 3.11 shows the mesh that we used for this calculation.

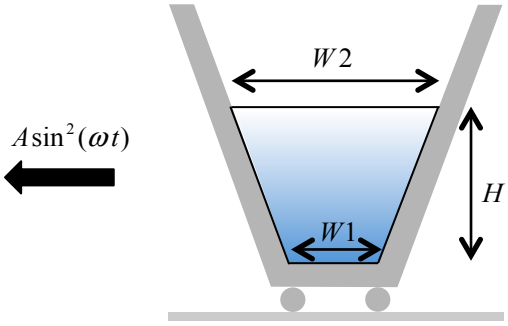

(Fig. 3.10) Problem definition for long duration calculation of oil sloshing in a trapezoidal tank

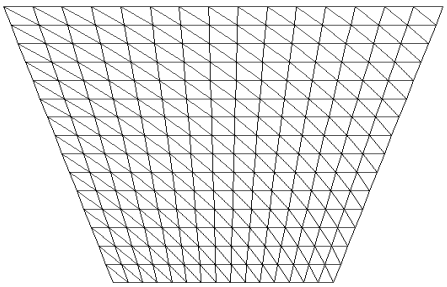

(Fig. 3.11) Mesh used with $15\times15\times2=450$ elements

We choose the engine oil SAE 5W-20 as the material for this problem to ensure that the flow interface does not break. The material properties of the sloshing liquid, geometric parameters, and flow conditions are presented in table 3.1:

(Table 3.1) Properties used for the sloshing problem

Excitation velocity	$A=-1, \quad \omega=5$
Density	$\rho=850kg/m^3$
Viscosity	$\mu=45.2kg/m\cdot\sec$
Gravitational acceleration	$g=9.81m/\sec^2$
Time step size	$\Delta t=0.01\sec$
Time duration	$t_{\max}=125.6\sec=100$ cycles
Bottom width of the container	$W_1=0.5m$
Water width at equilibrium ($t=0\sec$)	$W_2=1m$
Equilibrium height ($t=0\sec$)	$H=1m$

In this section, we verify the validity of equation (2.3) which is not the same as what was suggested in other ALE references (reference [17]). As mentioned above in order to show the effect of having non-zero $\frac{\partial\rho}{\partial t}$ at a fixed point, this example uses an excitation velocity that does not cause the domain to return to the original position.

The following equation,

$$\int_{t+\Delta t\Gamma} ({}^{t+\Delta t}\underline{u}\cdot\underline{n})\, d^{\,t+\Delta t}\Gamma = -\frac{2}{\Delta t}({}^{t+\Delta t}\Omega - {}^{t}\Omega) + \int_{t+\Delta t\Gamma} ({}^{t+\Delta t}\underline{u}_m\cdot\underline{n})\, d^{\,t+\Delta t}\Gamma - \int_{t+\Delta t\Gamma} ({}^{t+\Delta t}\underline{u}_c\cdot\underline{n})\, d^{\,t}\Gamma \tag{3.7}$$

is a reformulation of equation (2.7) and has the benefit of stability; it does not allow numerical dissipation, as discussed in the choice of the time advancing method choice (see section 2.2). The mass conservation error after 100 cycles is 9.47×10^{-9} % of the original mass. One hundred

cycles of sloshing correspond to a physical time of approximately 2 minutes. In other words, mass conservation errors are negligible even for calculations that involve long physical times.

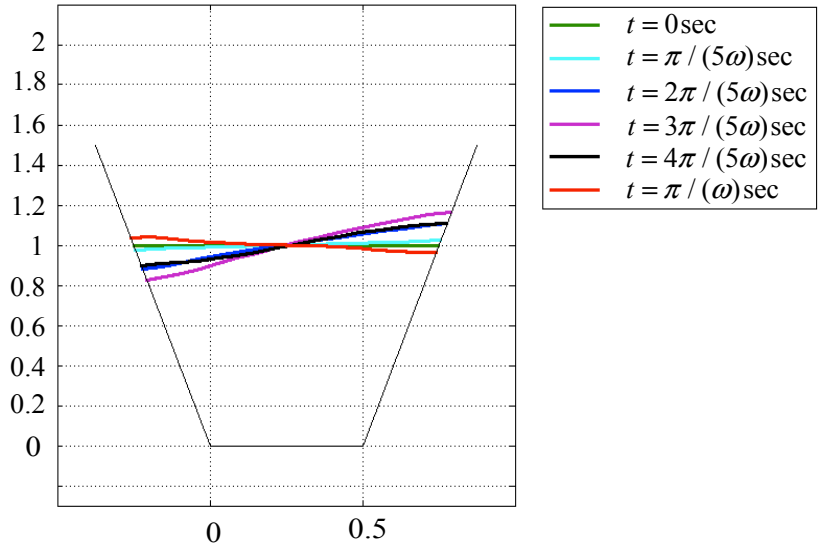

(Fig. 3.12) Interface snapshot of the first half cycle of the engine oil sloshing simulation

3.2.4 Multi-phase flow problem

In this section, a multi-phase (2- phase) problem is considered. Many applications, such as in the oil industry [21], combustion engineering [22], biofluidics [23], etc., require a reliable solution scheme for multi-phase flows. The solution scheme for the ALE-FCBI method does not differ much from that for free surface flows. However, there are some differences on how we treat control volumes. Let us consider elements around the interface of the two flows as depicted in figure 3.13.

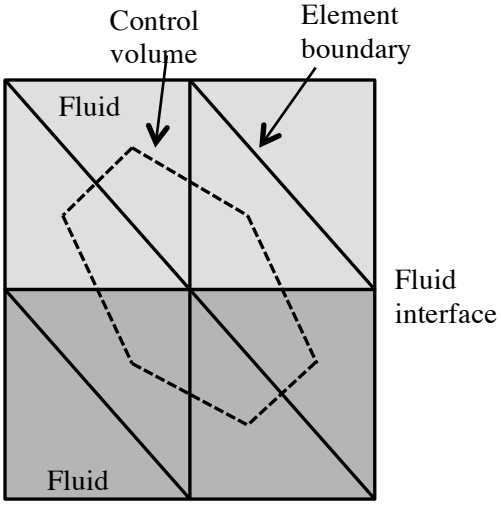

(Fig. 3.13) A control volume at the interface of multi-phase flow

Since an interface control volume contains different fluid materials, the mass conservation equation is written as equation (3.8), which is a general multi-phase mass conservation equation with the index i - element numbering in a control volume. Therefore, Γ_i is the control surface that encloses the control volume in element i, and Ω_i is the part of the control volume that belongs to the element i.

$$\sum_{i=1}^{n} \int_{\Gamma_i} q(\rho_i \underline{u} \cdot \underline{n}) d\Gamma_i = \sum_{i=1}^{n} [-\frac{d}{dt}(\int_{\Omega_i} q\rho_i d\Omega_i + \int_{\Gamma_i} q(\rho_i \underline{u}_m \cdot \underline{n}) d\Gamma_i)] \qquad (3.8)$$

where n is the total number of elements around the interface node.

The comparison simulation is performed and mass conservation equation models along with the time advancing methods are tested. Below is the problem description with the physical property variables, which are suggested in reference [24].

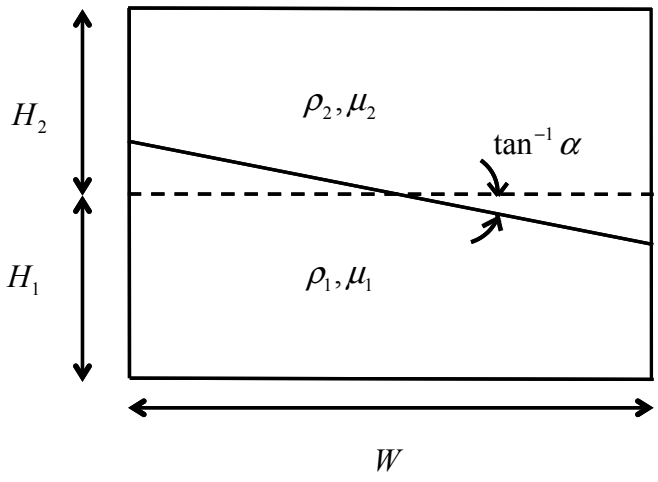

(Fig. 3.14) Definition of the simulation for two-phase flow comparison

Reference [24] provides the simulation results of an experiment of large amplitude for 2-phase flow. We solve the problem using the condition of the reference. The problem statement is the sloshing of the 2-phase flow with different material properties. As described in figure 3.13 and similarly to the 1-phase free surface flow configuration, the lines defining the elements and the lines defining the interface overlap. However, for multiphase flows, the line defining the control volume does not necessarily overlap with the fluid interfaces. In the example shown in figure 3.14, the density of the lower domain, which is heavier, is $\rho_1 = 2$ and the upper domain has a density $\rho_2 = 1$. The viscosity of both fluids is given as $\mu_1 = \mu_2 = 0.001$. The gravitational acceleration is given as $g = 0.294$ and the initial slope of the interface is $\alpha = 0.25$. The dimensions are $W = 0.8$, $H_1 = 0.3$ and $H_2 = 0.3$. Note that this is a pure numerical example, therefore, units are not given for the dimensions and material properties.

Reference [24] uses the technique of mass correction to conserve mass. However, in this thesis, no specific treatment is needed because mass conservation was derived from the proper mathematical and physical control volume analysis. Note that the reference uses an explicit Euler time integration method which requires the CFL condition to be fulfilled for stability. If the time step size is not small enough, the solution is unstable. For comparison, we tested both an explicit Euler time advancing scheme (model A) and an implicit Euler time advancing scheme (model B-1). Model B-2 adopts the trapezoidal time integration scheme.

For multi-phase flow, control volumes can contain many elements that belong to distinct phases and each element must be assigned its correct density and viscosity. Therefore, the mass conservation equation for this two phase flow can be rewritten as

$$\sum_{i=1}^{n} \int_{t+\Delta t\Gamma} \rho_i ({}^{t+\Delta t}\underline{u} \cdot \underline{n}) d\Gamma_i = {}^{t+\Delta t}R_m \tag{3.9}$$

where ${}^{t+\Delta t}R_m$ is a generic notation for a function which, in what follows, depends on the model we use. Symbol ρ_i denotes the corresponding density at each flux calculation point within the control surfaces. First, in the explicit Euler equation, we used the following solution scheme.

Model (A)

$${}^{t+\Delta t}R_m = 0 \tag{3.10}$$

$${}^{t+\Delta t}\underline{X} = {}^{t}\underline{X} + \Delta t({}^{t}\underline{u}_m) \tag{3.11}$$

The following model uses the implicit Euler scheme and the correct ALE formulation.

Model (B-1):

$${}^{t+\Delta t}R_m = \sum_{i=1}^{2} [-\frac{1}{\Delta t} \rho_i ({}^{t+\Delta t}\Omega_i - {}^{t}\Omega_i) + \int \rho_i ({}^{t+\Delta t}\underline{u}_m \cdot \underline{n}) d\Gamma] \tag{3.12}$$

$${}^{t+\Delta t}\underline{X} = {}^{t}\underline{X} + \Delta t({}^{t+\Delta t}\underline{u}_m) \tag{3.13}$$

$${}^{t+\Delta t}\underline{a} = \frac{1}{\Delta t}({}^{t+\Delta t}\underline{u} - {}^{t}\underline{u}) \tag{3.14}$$

Next, mass conservation is enforced with the trapezoidal rule time advancing scheme, which is the method that we primarily use in this thesis, and which we suggest for the calculation of multi-phase flows. It requires mesh updates at every iteration in order to calculate mass conservation correctly and the current time step's volume must be calculated at each iteration until it converges. Therefore, it is the most nonlinear scheme among the 3 suggested mass conservation schemes. We will refer to it as model (B-2)

Model (B-2):

$$ {}^{t+\Delta t}R_m = \sum_{i=1}^{2}[-\frac{2}{\Delta t}\rho_i({}^{t+\Delta t}\Omega_i - {}^{t}\Omega_i) + \int_{t+\Delta t\Gamma_i}\rho_i({}^{t+\Delta t}\underline{u}_m \cdot \underline{n})d\,{}^{t+\Delta t}\Gamma_i - \int_{t\Gamma_i}\rho_i({}^{t}\underline{u}_c \cdot \underline{n})d\,{}^{t}\Gamma_i] \quad (3.15) $$

$$ {}^{t+\Delta t}\underline{X} = {}^{t}\underline{X} + \frac{\Delta t}{2}({}^{t+\Delta t}\underline{u}_m + {}^{t}\underline{u}_m) \quad (3.16) $$

$$ {}^{t+\Delta t}\underline{a} = -{}^{t}\underline{a} + \frac{2}{\Delta t}({}^{t+\Delta t}\underline{u} - {}^{t}\underline{u}) \quad (3.17) $$

All comparison calculations provided as below use $14\times14\times2 = 392$ triangular elements, equally spaced in each direction. This discretization choice was made in order to facilitate the comparison with the data of reference [24], which uses 400 elements.

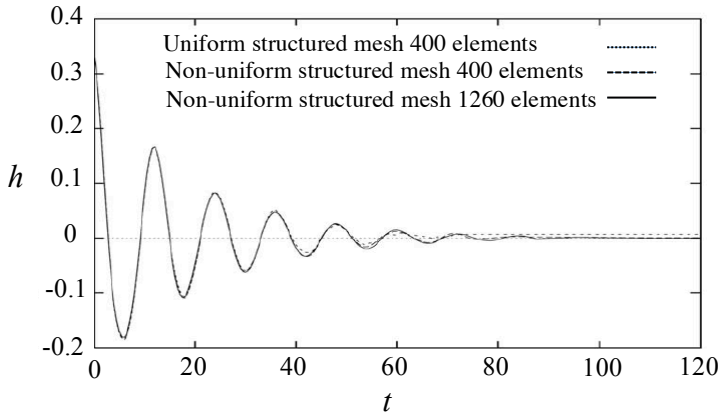

(a)

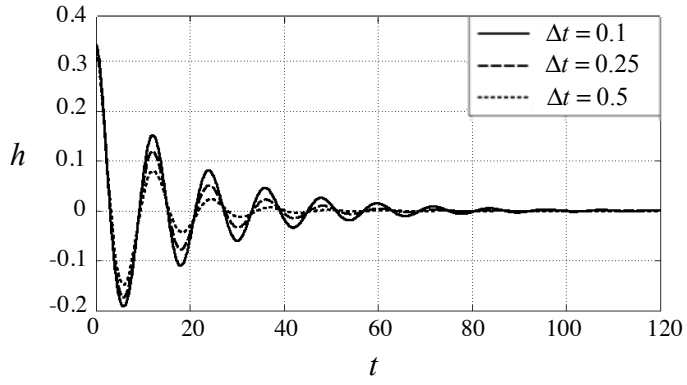

(b)

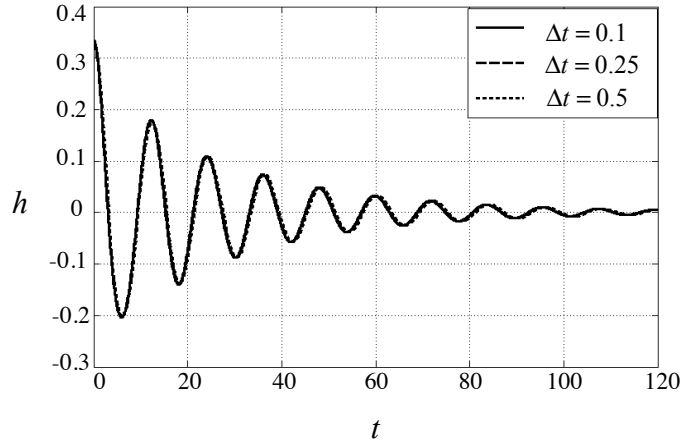

(c)

(Fig. 3.15) Time history of the left wall interface height:
(a) results of reference [24]
(b) results using model A-1
(c) results using model B

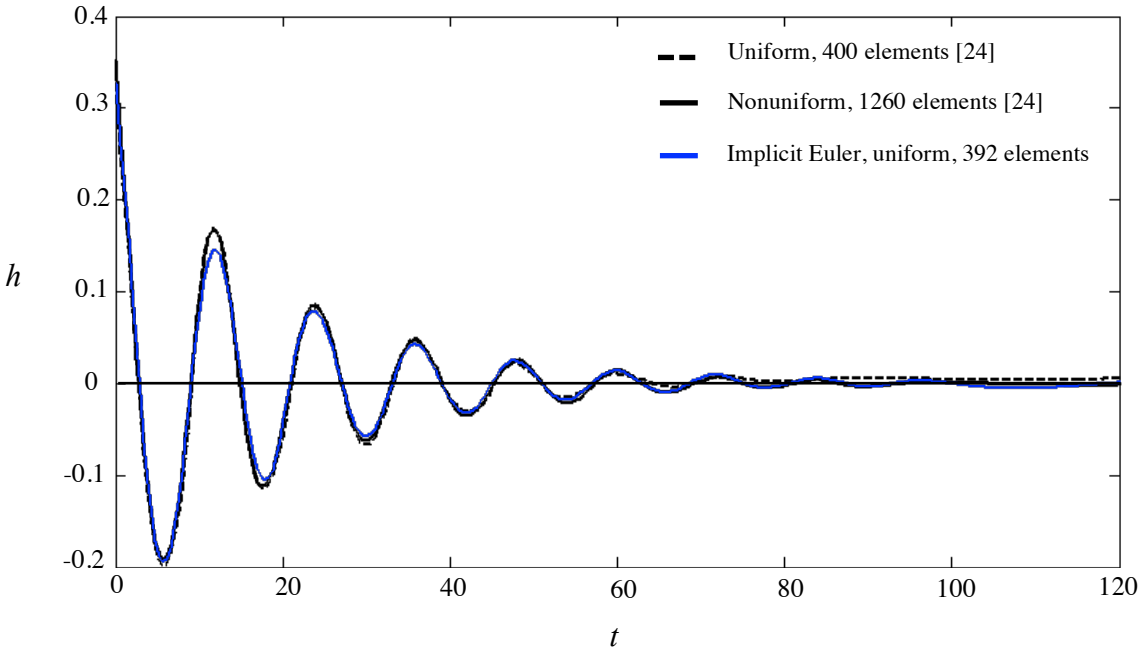

(Fig. 3.16) Time history of the left wall interface height comparison

The results of reference [24] show good agreement with the dissipative implicit Euler scheme result of 2-D ALE-FCBI (see figure 3.15). Using the trapezoidal and explicit Euler scheme shows less amplitude dissipation than the reference's results. Also of note is that the reference's dissipated state from time $t = 80$ shows that the overall height is higher than the original undisturbed height, indicating that the scheme did not exactly maintain the mass (see figure 3.16). For this 2-phase flow example, at $t = 120$, the implicit Euler scheme and the trapezoidal scheme respectively give mass errors of 0.0178% and 0.0251%, whereas reference [24] obtains a mass error of 1%.

Chapter 4

Three-dimensional FCBI ALE problems

The motivation of the development for the tetrahedral element is its capability to generate meshes that are adapted to complicated 3-D geometries. For the simple structured mesh problems used here, we calculate the solutions with structured meshes based on hexahedra. One hexahedron can be divided into 6 tetrahedral elements (see figure 4.1).

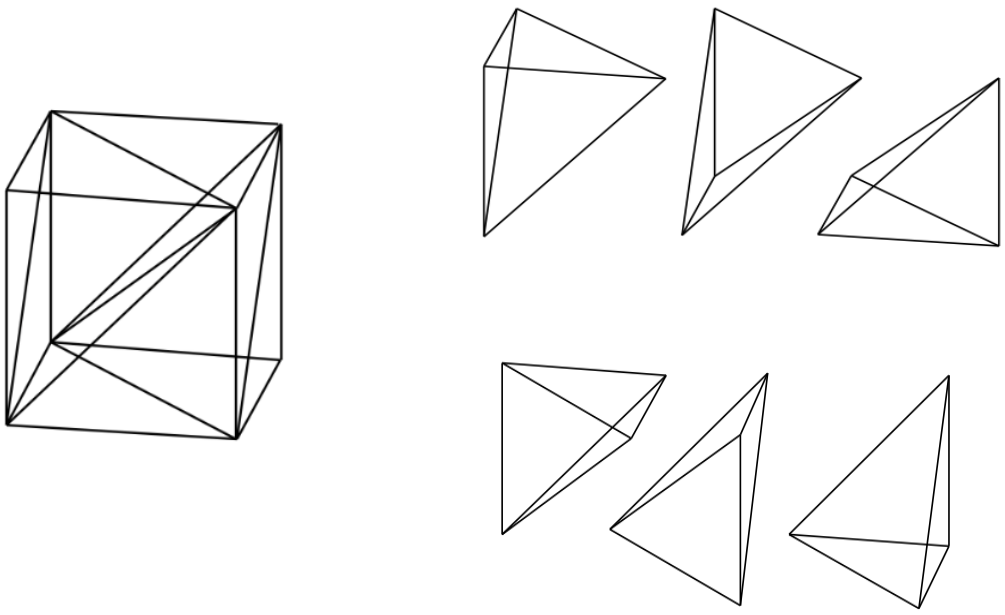

(Fig. 4.1) A hexahedron for structured mesh and its constituting tetrahedral elements

4.1 Three-dimensional FCBI formulation

4.1.1 Tetrahedral FCBI MINI element theory

Three dimensional unsteady incompressible fluid flows are considered, where the flow is governed by the Navier-Stokes equations. Assuming that the problem is well-posed in the Hilbert spaces U and P, the governing differential forms of the problem may be expressed as follows.

Find the velocity $\underline{u}(\underline{x}) \in U$ and pressure $p(\underline{x}) \in P$

$$\frac{\partial \rho}{\partial t} + \nabla \cdot (\rho \underline{u}) = 0 \qquad , \quad \underline{x} \in \Omega \tag{4.1}$$

$$\frac{\partial \rho \underline{u}}{\partial t} + \nabla \cdot (\rho \underline{u}\underline{v} - \underline{\tau}) = \rho \underline{g} \qquad , \quad \underline{x} \in \Omega \tag{4.2}$$

where $\underline{\tau}$ is the stress calculated as

$$\underline{\tau} = \underline{\tau}(\underline{u}, p) = -p\underline{I} + \mu\left\{\nabla \underline{u} + (\nabla \underline{u})^T\right\} \tag{4.3}$$

and $\underline{I}$ in equation (4.3) is an identity tensor. The essential boundary conditions are

$$\underline{u} = \underline{u}^s \qquad , \quad \underline{x} \in S_v \tag{4.4}$$

and the force boundary conditions are

$$\underline{\tau} \cdot \underline{n} = \underline{f}^s \qquad , \quad \underline{x} \in S_f \tag{4.5}$$

where $\underline{u}^s$ is the prescribed velocity on the boundary S_v, $\underline{f}^s$ is the prescribed traction on the boundary S_f, and $\underline{n}$ is the normal vector to the boundary. The boundary should satisfy the conditions $S = S_v \cup S_f$ and $S_v \cap S_f = \varnothing$, in the fluid domain $\Omega \in \Re^3$. We used a Petrov-Galerkin variational formulation in subspaces U_h, V_h and W_h of $\underline{U}$ and we use subspaces P_h and Q_h of P for the finite element solution. The formulation for the numerical solution is:

Find $\underline{u} \in U_h$, $\underline{v} \in V_h$ and $p \in P_h$ such that for all $w \in W_h$ and $q \in Q_h$

$$\int_\Omega q[\frac{\partial \rho}{\partial t} + \nabla \cdot \rho \underline{u}] \, d\Omega = 0 \tag{4.6}$$

$$\int_\Omega w \, [\rho \frac{\partial \underline{u}}{\partial t} + \nabla \cdot (\rho \underline{u}\underline{v} - \tau(\underline{u}, p))] \, d\Omega = \int_\Omega w \, [\rho \underline{g}] \, d\Omega \tag{4.7}$$

The trial functions U_h and P_h are the conventional linear interpolation functions of finite element for velocity and pressure, respectively. These are selected to satisfy the inf-sup condition of incompressible analysis [15]. The advection term, which is not considered in the Stokes flow assumptions, requires different trial functions in V_h from the functions in U_h. The trial functions in V_h should satisfy the stability of the method. Step weight functions are chosen in the spaces W_h and Q_h, to achieve the local conservation of momentum and mass, respectively.

By applying the Reynolds transport theorem to the free surface governing equations, we can choose the control volumes to enclose only one material (see section 1.2). In this case, the density inside the control volume is kept constant throughout the time while the mesh is moved arbitrarily in each phase. Since ALE allows the control volumes to move arbitrarily, applying Reynolds transport theorem and Gauss's theorem to equations (4.6) and (4.7) results in equations (4.8) and (4.9).

$$\frac{d}{dt}\int_\Omega q \, d\Omega + \int_\Omega q \, [(\underline{u} - \underline{u}_m) \cdot \underline{n}] \, d\Gamma = 0 \tag{4.8}$$

$$\frac{d}{dt}\int_\Omega w \, [\rho \underline{u}] \, d\Omega + \int_\Gamma w \, [\rho \underline{v}\{(\underline{u} - \underline{u}_m) \cdot \underline{n}\}] \, d\Gamma - \int_\Gamma w \, [\underline{\tau}(\underline{u}, p) \cdot \underline{n}] \, d\Gamma = \int_\Omega w \, [\rho \underline{g}] \, d\Omega \tag{4.9}$$

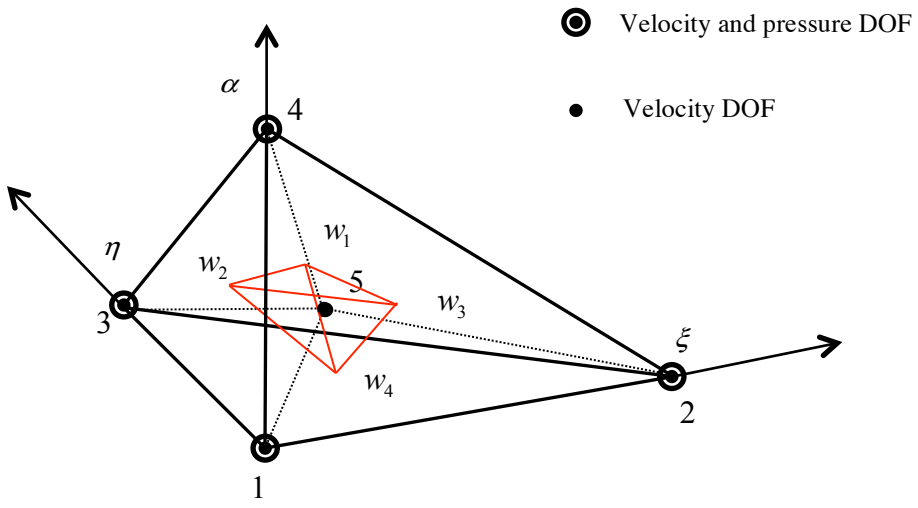

(Fig. 4.2) A 3-D MINI element

To establish an FCBI scheme for tetrahedral grids that can be used for problems with complex geometries, we develop a new method that possesses the basic ingredients mentioned above, i.e. interpolations that satisfy the inf-sup condition, the use of the flow conditions in the trial functions and step functions as weight functions. The procedure using the MINI element is detailed in this section.

Figure 4.2 shows a MINI element in which the velocity is defined at five nodes, local node numbers 1-5, while the pressure is defined at four nodes, the local node numbers 1-4, in order to satisfy the inf-sup condition. The flux is calculated with the interpolated values at the center of the surfaces of the control volumes. Velocity $\underline{u}$ and pressure p are obtained with the trial functions in U_h and P_h given in Tables 4.1 and 4.2.

The 3-dimensional interpolations for the usual velocities and pressure satisfy the following equations

$$\underline{u} = h_i^u \underline{\hat{u}}_i \tag{4.10}$$

$$p = h_i^p \hat{p}_i \tag{4.11}$$

where $\hat{\underline{u}}_i$ and $\hat{p}_i$ are the nodal velocity and pressure variables, respectively. With the use of step weight functions around nodes, the control volumes in the spaces W_h and Q_h can be defined as shown in figures 4.3a and 4.3b respectively, as well as in figures 4.4 and 4.5.

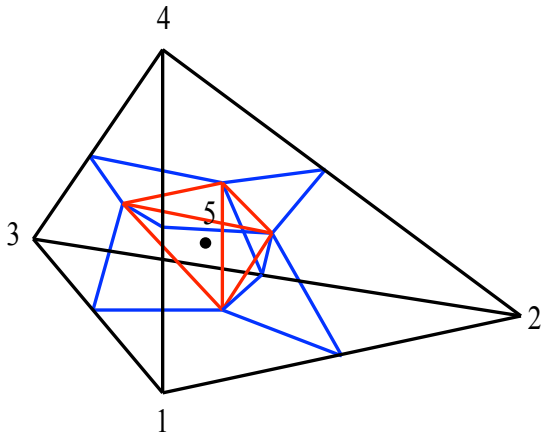

(a)

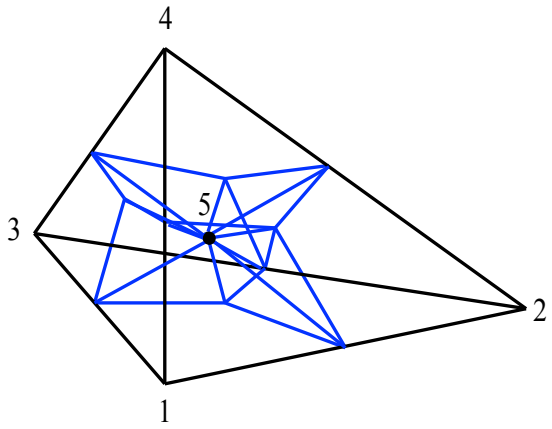

(b)

(Fig. 4.3) Control volumes and control surfaces:
(a) segment in space W_h and (b) segment in space Q_h

A hexahedron for structured meshes is generated as described in figure 4.1 for convenience. These patterns are not symmetric with respect to any axes, to verify the independence of the solution from the meshes' shapes when tested in 2-D like problems. Also, since the mesh

distortion level is diverse, we can show the independence of the solution from the mesh distortion.

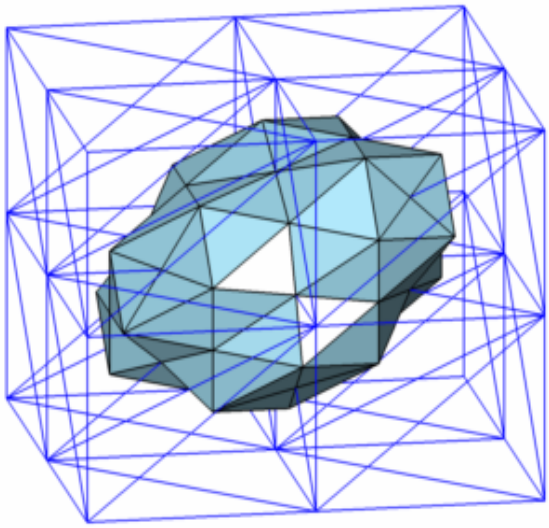

(Fig. 4.4) Typical control volume consisting of 4 neighboring hexahedra in space W_h

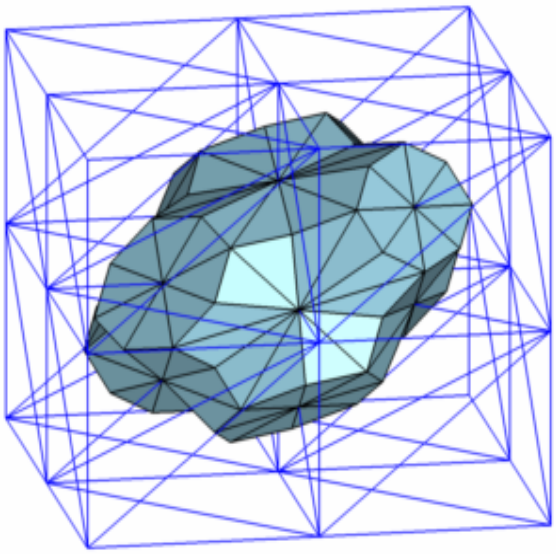

(Fig. 4.5) Typical control volume consisting of 4 neighboring hexahedra in space Q_h

(Table 4.1) Trial functions in U_h and nodal coordinates

Trial function	i	ξ	η	α
$h_1^u = 1-\xi-\eta-\alpha-\phi/4$	1	0	0	0
$h_2^u = \xi-\phi/4$	2	1	0	0
$h_3^u = \eta-\phi/4$	3	0	1	0
$h_4^u = \alpha-\phi/4$	4	0	0	1
$h_5^u = \phi$	5	$1/4$	$1/4$	$1/4$

The bubble function corresponds to the region as follows [25].

$$\phi = \begin{cases} 4\,(1-\xi-\eta-\alpha) & \text{in region } w_1 \\ 4\,\xi & \text{in region } w_2 \\ 4\,\eta & \text{in region } w_3 \\ 4\,\alpha & \text{in region } w_4 \end{cases} \tag{4.12}$$

in four domains shown in Figure 4.6.

(Table 4.2) Trial functions in P_h and nodal coordinates

Trial function	i	ξ	η	α
$h_1^P = 1-\xi-\eta-\alpha$	1	0	0	0
$h_2^P = \xi$	2	1	0	0
$h_3^P = \eta$	3	0	1	0
$h_4^P = \alpha$	4	0	0	1

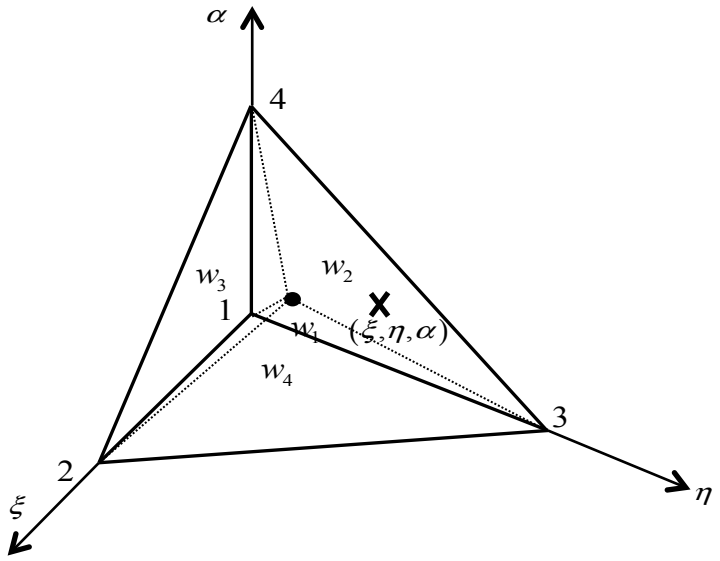

(Fig. 4.6) A tetrahedral MINI element with the definition of the region

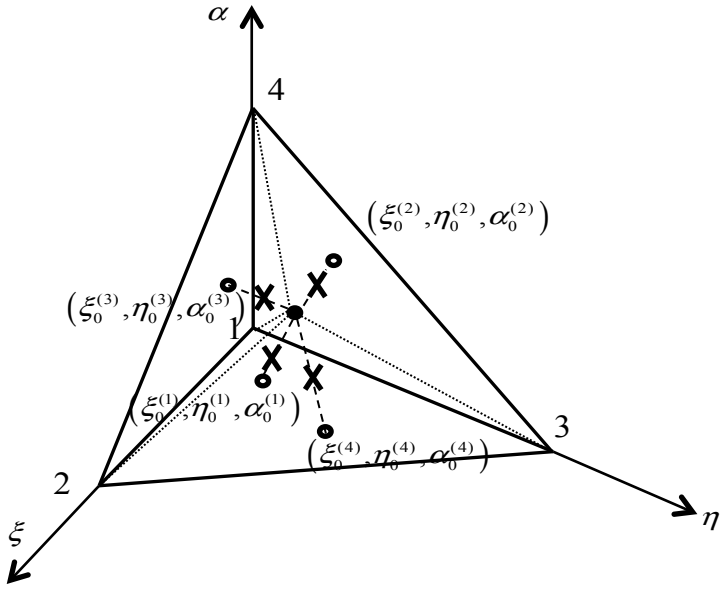

(Fig. 4.7) Variables used for the calculation of the trial functions in V_h
Note that the right superscripts in parentheses indicate region numbers.

Geometrically, $\xi_0^{(1)} + \eta_0^{(1)} + \alpha_0^{(1)} = 1$, $\xi_0^{(2)} = 0$, $\eta_0^{(3)} = 0$ and $\alpha_0^{(4)} = 0$ are satisfied (see figure 4.7). In order to reach a stable solution scheme, $\underline{v}$ in the advection term uses interpolations derived from flow conditions. Flow conditions are evaluated on the faces of the element with an analytical 1-dimensional advection-diffusion equation (see figure 4.8). In each of the four regions, w_1, w_2, w_3 and w_4, velocities are decomposed into their parallel-to-face component $\underline{v}_{\mathrm{P}}$ and their normal to face component $\underline{v}_{\perp}$. We then apply different interpolation functions to those components. For the parallel-to-face components, the flow-condition-based interpolation is applied and the perpendicular components are interpolated with the usual linear interpolation schemes. The trial functions for the parallel component h_{P}^{v} in V_h are given in Tables 4.3 and 4.4 (a), (b), (c) and (d). Therefore, the velocity $\underline{v}$ is calculated with the following equations:

$$v_{\mathrm{P}} = h_{i\mathrm{P}}^{v} v_{i\mathrm{P}} = h_i^{v} v_{i\mathrm{P}} \tag{4.13}$$

$$v_{\perp} = h_{i\perp}^{v} v_{i\perp} = h_i^{u} v_{i\perp} \tag{4.14}$$

where i is the node number.

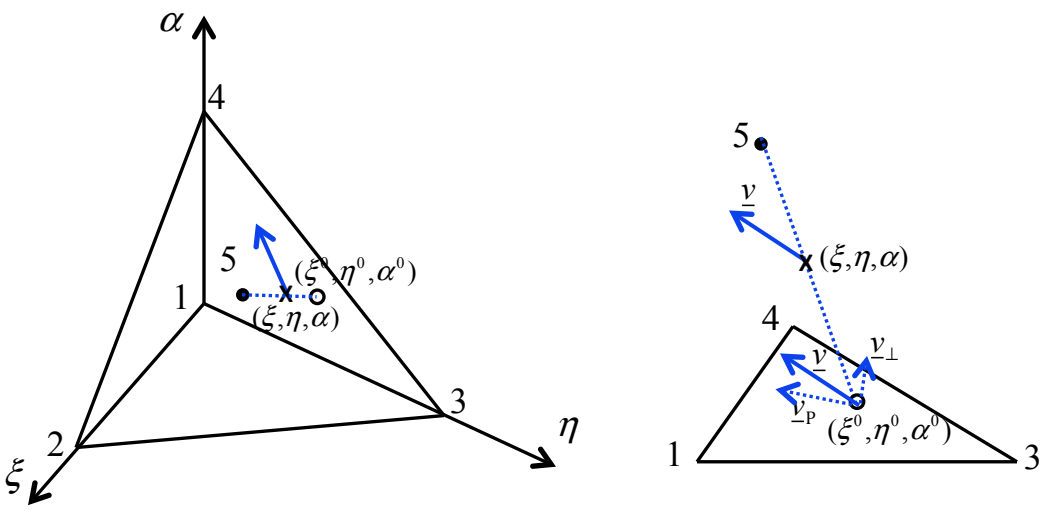

(Fig. 4.8) Factorization of the velocity at an interior flux calculation point

Based on the location of $(\xi_0, \eta_0, \alpha_0)$ on the faces of an element, the trial functions of V_h are determined (see Figures 4.11 (a), (b), (c) and (d)). The interpolations of the 1-D simplified Navier-Stokes equation with convection-diffusion terms are derived. The interpolation of region 1, for example, is calculated first by calculating the 1-D analytical solution along the element's edges, and acquires the information at mid-edge points (see figure 4.9), i.e., velocities at points P_{24}, P_{43} and P_{32}. The vertex nodes (resp. 2, 3 and 4 in figures 4.9 and 4.10) and the opposite mid-edge points (resp. P_{43}, P_{24} and P_{32} in figures 4.9 and 4.10) define three segments that intersect at the mid-face point (P_{243} in figures 4.9 and 4.10). By applying 1-D advection-diffusion analysis to these three segments, we obtain three different interpolations of values at a mid-face point. The final expression for an interpolated value at a mid-face point is the average of three interpolated values (see equation (4.15) for the example of region 1). These interpolations are applied to the two velocity components that are in the direction of two orthonormal vectors spanning the plane of the element face.

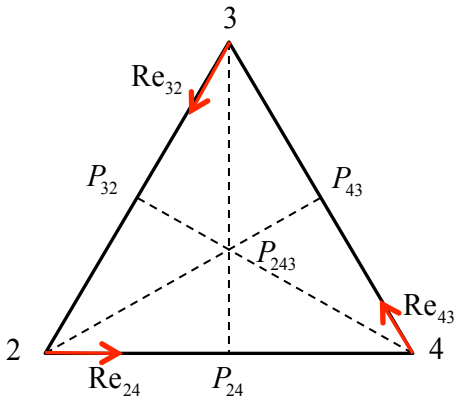

(Fig. 4.9) First 1-D advection-diffusion solution assumption procedure along the element edges

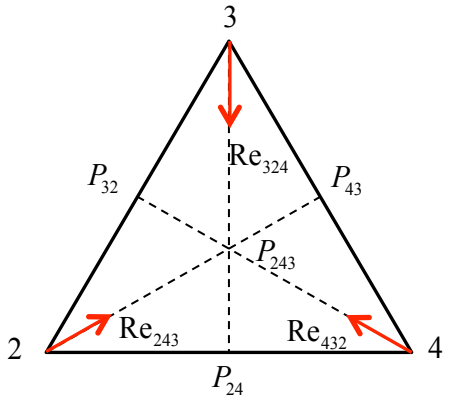

(Fig. 4.10) Second 1-D advection-diffusion solution assumption procedure through the element face's center

$$H_{243} = \frac{1}{3}(H_{3-P24} + H_{2-P43} + H_{4-P32}) \qquad (4.15)$$

Finally, vertex nodes, mid-edge points and a mid-face point define six inner triangles (for instance, 2, P_{32} and P_{243} in figures 4.9 and 4.10). We then calculate the values in inner triangles by linear interpolation of the vertices of the inner triangles (see appendix A).

(Table 4.3) Trial functions in V_h for the velocity component parallel to the element faces

Trial function	w_1	w_2	w_3	w_4
h^v_{1P}	0	$(1-4\xi)f_1^{(2)}$	$(1-4\eta)f_1^{(3)}$	$(1-4\alpha)f_1^{(4)}$
h^v_{2P}	$(4\xi+4\eta+4\alpha-3)f_2^{(1)}$	0	$(1-4\eta)f_2^{(3)}$	$(1-4\alpha)f_2^{(4)}$
h^v_{3P}	$(4\xi+4\eta+4\alpha-3)f_3^{(1)}$	$(1-4\xi)f_3^{(2)}$	0	$(1-4\alpha)f_3^{(4)}$
h^v_{4P}	$(4\xi+4\eta+4\alpha-3)f_4^{(1)}$	$(1-4\xi)f_4^{(2)}$	$(1-4\eta)f_4^{(3)}$	0
h^v_{5P}	$(4-4\xi-4\eta-4\alpha)$	4ξ	4η	4α

(Table 4. 4 (a)) Parameters used for the trial functions in V_h for the velocity component parallel to the element at each location of (ξ_0,η_0,α_0) in region w_1

	a_{11}	a_{12}	a_{13}	a_{14}	a_{15}	a_{16}
$f_1^{(1)}$	0	0	0	0	0	0
$f_2^{(1)}$	$(1-\eta_0-2\alpha_0)$ $+(2\alpha_0-2\eta_0)h_{24}$ $3\eta_0c_{12}$	$(2\xi_0-2\eta_0)h_{24}$ $+3\eta_0c_{12}$	$3\xi_0c_{12}$	$3\xi_0c_{12}$	$3\alpha_0c_{12}$ $+(2\xi_0-2\alpha_0)h_{23}$	$(-1+\alpha_0+2\xi_0)$ $3\alpha_0c_{12}$ $+(2-2\xi_0+2\alpha_0)h_{23}$
$f_3^{(1)}$	$3\eta_0c_{13}$	$3\eta_0c_{13}$	$3\xi_0c_{13}$ $+(2\alpha_0-2\xi_0)h_{34}$	$(-1+\xi_0+2\eta_0)$ $+3\xi_0c_{13}$ $+(2-4\xi_0-2\eta_0)h_{34}$	$(1-\alpha_0-2\xi_0)$ $+3\alpha_0c_{13}$ $+(2\xi_0-2\alpha_0)h_{32}$	$3\alpha_0c_{13}$ $+(2-2\xi_0+2\alpha_0)h_{32}$
$f_4^{(1)}$	$(2\alpha_0-2\eta_0)h_{42}$ $+3\eta_0c_{14}$	$(1-\eta_0-2\xi_0)$ $+(2\xi_0-2\eta_0)h_{42}$ $+3\eta_0c_{14}$	$(1-\xi_0-2\alpha_0)$ $+(2\alpha_0-2\xi_0)h_{43}$ $+3\xi_0c_{14}$	$+3\xi_0c_{14}$ $+(2-4\xi_0-2\eta_0)h_{43}$	$3\alpha_0c_{14}$	$3\alpha_0c_{14}$

(Table 4.4 (b)) Parameters used for the trial functions in V_h for the velocity component parallel to the element at each location of (η_0, α_0) in region w_2

	a_{21}	a_{22}	a_{23}	a_{24}	a_{25}	a_{26}
$f_1^{(2)}$	$(1-\alpha_0-2\eta_0)$ $+(2\eta_0-2\alpha_0)h_{13}$ $+3\alpha_0 c_{21}$	$3\alpha_0 c_{21}$ $+(2-4\alpha_0-2\eta_0)h_{13}$	$(3-3\eta_0-3\alpha_0)c_{21}$	$(3-3\eta_0-3\alpha_0)c_{21}$	$(-4\eta_0-2\alpha_0+2)h_{14}$ $(3\eta_0)c_{21}$	$(-\eta_0-2\alpha_0+1)h_{14}$
$f_2^{(2)}$	0	0	0	0	0	0
$f_3^{(2)}$	$(2\eta_0-2\alpha_0)h_{31}$ $+3\alpha_0 c_{23}$	$(2\eta_0+\alpha_0-1)$ $+(2-4\alpha_0-2\eta_0)h_{31}$ $+3\alpha_0 c_{23}$	$\eta_0-\alpha_0$ $+(2\eta_0+4\xi_0-2)h_{34}$ $+(3-3\eta_0-3\alpha_0)c_{23}$	$(4\eta_0+2\alpha_0-2)h_{34}$ $+(3-3\eta_0-3\alpha_0)c_{23}$	$(3\eta_0)c_{23}$	$(3\eta_0)c_{23}$
$f_4^{(2)}$	$3\alpha_0 c_{24}$	$3\alpha_0 c_{24}$	$(2\eta_0+4\alpha_0-2)h_{43}$ $+(3-3\eta_0-3\alpha_0)c_{24}$	$(-\eta_0+\alpha_0)$ $+(-2+2\alpha_0+4\eta_0)h_{43}$ $+(3-3\eta_0-3\alpha_0)c_{24}$	$(-1+\eta_0+2\alpha_0)$ $+(2-2\alpha_0-4\eta_0)h_{41}$ $(3\eta_0)c_{24}$	$(-2\eta_0+2\alpha_0)h_{41}$ $(3\eta_0)c_{23}$

(Table 4.4 (c)) Parameters used for the trial functions in V_h for the velocity component parallel to the element at each location of (ξ_0, α_0) in region w_3

	a_{31}	a_{32}	a_{33}	a_{34}	a_{35}	a_{36}
$f_1^{(3)}$	$(1-\alpha_0-2\xi_0)$ $+(2\xi_0-2\alpha_0)h_{12}$ $+3\alpha_0 c_{31}$	$3\alpha_0 c_{31}$ $+(2-4\alpha_0-2\xi_0)h_{12}$	$(3-3\xi_0-3\alpha_0)c_{31}$	$(3-3\xi_0-3\alpha_0)c_{31}$	$(-4\xi_0-2\alpha_0+2)h_{14}$ $(3\xi_0)c_{31}$	$(1-\xi_0-2\alpha_0)$ $(-2\xi_0+2\alpha_0)h_{14}$ $(3\xi_0)c_{31}$
$f_2^{(3)}$	$(2\xi_0-2\alpha_0)h_{21}$ $+3\alpha_0 c_{32}$	$(-1+\alpha_0+2\xi_0)$ $+3\alpha_0 c_{32}$ $+(2-4\alpha_0-2\xi_0)h_{21}$	$(\xi_0-\alpha_0)$ $+(3-3\xi_0-3\alpha_0)c_{32}$ $+(-2+4\alpha_0+2\xi_0)h_{24}$	$(3-3\xi_0-3\alpha_0)c_{32}$ $+(-2+4\xi_0+2\alpha_0)h_{24}$	$(3\xi_0)c_{32}$	$(3\xi_0)c_{32}$
$f_3^{(3)}$	0	0	0	0	0	0
$f_4^{(3)}$	$3\alpha_0 c_{34}$	$3\alpha_0 c_{34}$	$(2\eta_0+4\alpha_0-2)h_{43}$ $+(3-3\xi_0-3\alpha_0)c_{34}$	$(3-3\xi_0-3\alpha_0)$ $+(-2+2\alpha_0+4\xi_0)h_{42}$ $+(3-3\xi_0-3\alpha_0)c_{24}$	$(-1+\xi_0+2\alpha_0)$ $+(2-2\alpha_0-4\xi_0)h_{41}$ $(3\xi_0)c_4$	$(-2\xi_0+2\alpha_0)h_{41}$ $(3\xi_0)c_{24}$

(Table 4 .4(d)) Parameters used for the trial functions in V_h for the velocity component parallel to the element at each location of $(\xi_0, \eta_0, \alpha_0)$ in region w_4

	a_{41}	a_{42}	a_{43}	a_{44}	a_{45}	a_{46}
$f_1^{(4)}$	$(1-\eta_0-2\xi_0)$ $+(2\xi_0-2\eta_0)h_{12}$ $+3\eta_0 c_{41}$	$3\eta_0 c_{41}$ $+(-4\eta_0-2\xi_0)h_{12}$	$(3-3\xi_0-3\eta_0)c_{41}$	$(3-3\xi_0-3\eta_0)c_{41}$	$(-4\xi_0-2\eta_0+2)h_{13}$ $(3\xi_0)c_{41}$	$(1-\xi_0-2\eta_0)$ $(-2\xi_0+2\eta_0)h_{13}$ $(3\xi_0)c_{41}$
$f_2^{(4)}$	$(2\xi_0-2\eta_0)h_{21}$ $+3\eta_0 c_{42}$	$(-1+\eta_0+2\xi_0)$ $+3\eta_0 c_{32}$ $+(-4\eta_0-2\xi_0)h_{21}$	$(\xi_0-\eta_0)$ $+(3-3\xi_0-3\eta_0)c_{42}$ $+(-2+4\eta_0+2\xi_0)h_{23}$	$(3-3\xi_0-3\alpha_0)c_{32}$ $+(-2+4\xi_0-2\eta_0)h_{23}$	$(3\xi_0)c_{42}$	$(3\xi_0)c_{42}$
$f_3^{(4)}$	$3\eta_0 c_{43}$	$3\eta_0 c_{43}$	$(2\xi_0+4\eta_0-2)h_{32}$ $+(3-3\xi_0-3\eta_0)c_{43}$	$(2\xi_0+4\eta_0-2)$ $+(-2+4\xi_0-2\eta_0)h_{32}$ $+(3-3\xi_0-3\eta_0)c_{43}$	$(-1+\xi_0+2\eta_0)$ $+(2-2\eta_0-4\xi_0)h_{31}$ $+(3\xi_0)c_{43}$	$(2\eta_0-2\xi_0)h_{31}$ $+(3\xi_0)c_{43}$
$f_4^{(4)}$	0	0	0	0	0	0

The coefficients c and h appearing in tables 4.4 are explicated below:

$$
\begin{aligned}
c_{12} &= c_{243} + (1-c_{432})(1-h_{32}) + (1-c_{324})h_{24} \\
c_{13} &= c_{324} + (1-c_{243})(1-h_{43}) + (1-c_{432})h_{32} \\
c_{14} &= c_{432} + (1-c_{324})(1-h_{24}) + (1-c_{243})h_{43}
\end{aligned}
\qquad (4.16)
$$

$$
\begin{aligned}
c_{21} &= c_{134} + (1-c_{341})(1-h_{41}) + (1-c_{413})h_{13} \\
c_{24} &= c_{413} + (1-c_{134})(1-h_{34}) + (1-c_{341})h_{41} \\
c_{23} &= c_{341} + (1-c_{413})(1-h_{13}) + (1-c_{134})h_{34}
\end{aligned}
\qquad (4.17)
$$

$$
\begin{aligned}
c_{31} &= c_{124} + (1-c_{241})(1-h_{41}) + (1-c_{412})h_{12} \\
c_{34} &= c_{412} + (1-c_{124})(1-h_{42}) + (1-c_{241})h_{41} \\
c_{32} &= c_{241} + (1-c_{412})(1-h_{41}) + (1-c_{124})h_{24}
\end{aligned}
\qquad (4.18)
$$

$$
\begin{aligned}
c_{41} &= c_{123} + (1-c_{231})(1-h_{31}) + (1-c_{312})h_{12} \\
c_{43} &= c_{312} + (1-c_{123})(1-h_{23}) + (1-c_{231})h_{31} \\
c_{42} &= c_{231} + (1-c_{312})(1-h_{12}) + (1-c_{123})h_{23}
\end{aligned}
\qquad (4.19)
$$

$$c_{243} = \frac{e^{0.67\mathrm{Re}243} - 1}{e^{\mathrm{Re}243} - 1} \qquad \mathrm{Re}_{243} = \frac{\rho}{\mu}\left[\frac{1}{3}\left(\underline{u}_c^2 + \underline{u}_c^3 + \underline{u}_c^4\right)\cdot\left(\frac{1}{2}\left(\underline{x}_4 + \underline{x}_3\right) - \underline{x}_2\right)\right] \tag{4.20}$$

$$c_{324} = \frac{e^{0.67\mathrm{Re}324} - 1}{e^{\mathrm{Re}324} - 1} \qquad \mathrm{Re}_{324} = \frac{\rho}{\mu}\left[\frac{1}{3}\left(\underline{u}_c^2 + \underline{u}_c^3 + \underline{u}_c^4\right)\cdot\left(\frac{1}{2}\left(\underline{x}_2 + \underline{x}_4\right) - \underline{x}_3\right)\right] \tag{4.21}$$

$$c_{432} = \frac{e^{0.67\mathrm{Re}432} - 1}{e^{\mathrm{Re}432} - 1} \qquad \mathrm{Re}_{432} = \frac{\rho}{\mu}\left[\frac{1}{3}\left(\underline{u}_c^2 + \underline{u}_c^3 + \underline{u}_c^4\right)\cdot\left(\frac{1}{2}\left(\underline{x}_3 + \underline{x}_2\right) - \underline{x}_4\right)\right] \tag{4.22}$$

$$c_{134} = \frac{e^{0.67\mathrm{Re}134} - 1}{e^{\mathrm{Re}134} - 1} \qquad \mathrm{Re}_{134} = \frac{\rho}{\mu}\left[\frac{1}{3}\left(\underline{u}_c^1 + \underline{u}_c^3 + \underline{u}_c^4\right)\cdot\left(\frac{1}{2}\left(\underline{x}_3 + \underline{x}_4\right) - \underline{x}_1\right)\right] \tag{4.23}$$

$$c_{413} = \frac{e^{0.67\mathrm{Re}413} - 1}{e^{\mathrm{Re}413} - 1} \qquad \mathrm{Re}_{413} = \frac{\rho}{\mu}\left[\frac{1}{3}\left(\underline{u}_c^1 + \underline{u}_c^3 + \underline{u}_c^4\right)\cdot\left(\frac{1}{2}\left(\underline{x}_1 + \underline{x}_3\right) - \underline{x}_4\right)\right] \tag{4.24}$$

$$c_{341} = \frac{e^{0.67\mathrm{Re}341} - 1}{e^{\mathrm{Re}341} - 1} \qquad \mathrm{Re}_{341} = \frac{\rho}{\mu}\left[\frac{1}{3}\left(\underline{u}_c^1 + \underline{u}_c^3 + \underline{u}_c^4\right)\cdot\left(\frac{1}{2}\left(\underline{x}_4 + \underline{x}_1\right) - \underline{x}_3\right)\right] \tag{4.25}$$

$$c_{124} = \frac{e^{0.67\mathrm{Re}124} - 1}{e^{\mathrm{Re}124} - 1} \qquad \mathrm{Re}_{124} = \frac{\rho}{\mu}\left[\frac{1}{3}\left(\underline{u}_c^1 + \underline{u}_c^2 + \underline{u}_c^4\right)\cdot\left(\frac{1}{2}\left(\underline{x}_2 + \underline{x}_4\right) - \underline{x}_1\right)\right] \tag{4.26}$$

$$c_{412} = \frac{e^{0.67\mathrm{Re}412} - 1}{e^{\mathrm{Re}412} - 1} \qquad \mathrm{Re}_{412} = \frac{\rho}{\mu}\left[\frac{1}{3}\left(\underline{u}_c^1 + \underline{u}_c^2 + \underline{u}_c^4\right)\cdot\left(\frac{1}{2}\left(\underline{x}_1 + \underline{x}_2\right) - \underline{x}_4\right)\right] \tag{4.27}$$

$$c_{241} = \frac{e^{0.67\mathrm{Re}241} - 1}{e^{\mathrm{Re}241} - 1} \qquad \mathrm{Re}_{241} = \frac{\rho}{\mu}\left[\frac{1}{3}\left(\underline{u}_c^1 + \underline{u}_c^2 + \underline{u}_c^4\right)\cdot\left(\frac{1}{2}\left(\underline{x}_4 + \underline{x}_1\right) - \underline{x}_2\right)\right] \tag{4.28}$$

$$c_{123} = \frac{e^{0.67\mathrm{Re}123} - 1}{e^{\mathrm{Re}123} - 1} \qquad \mathrm{Re}_{123} = \frac{\rho}{\mu}\left[\frac{1}{3}\left(\underline{u}_c^1 + \underline{u}_c^2 + \underline{u}_c^3\right)\cdot\left(\frac{1}{2}\left(\underline{x}_2 + \underline{x}_3\right) - \underline{x}_1\right)\right] \tag{4.29}$$

$$c_{312} = \frac{e^{0.67\mathrm{Re}312} - 1}{e^{\mathrm{Re}312} - 1} \qquad \mathrm{Re}_{312} = \frac{\rho}{\mu}\left[\frac{1}{3}\left(\underline{u}_c^1 + \underline{u}_c^2 + \underline{u}_c^3\right)\cdot\left(\frac{1}{2}\left(\underline{x}_1 + \underline{x}_2\right) - \underline{x}_3\right)\right] \tag{4.30}$$

$$c_{231} = \frac{e^{0.67\mathrm{Re}231} - 1}{e^{\mathrm{Re}231} - 1} \qquad \mathrm{Re}_{231} = \frac{\rho}{\mu}\left[\frac{1}{3}\left(\underline{u}_c^1 + \underline{u}_c^2 + \underline{u}_c^3\right)\cdot\left(\frac{1}{2}\left(\underline{x}_3 + \underline{x}_1\right) - \underline{x}_2\right)\right] \tag{4.31}$$

$$h_{12}=\frac{e^{0.5\mathrm{Re}12}-1}{e^{\mathrm{Re}12}-1} \qquad h_{21}=\frac{e^{\mathrm{Re}12}-e^{0.5\mathrm{Re}12}}{e^{\mathrm{Re}12}-1} \qquad \mathrm{Re}_{12}=\frac{\rho}{\mu}\left[\frac{1}{2}\left(\underline{u}_c^1+\underline{u}_c^2\right)\cdot\left(\underline{x}_2-\underline{x}_1\right)\right] \tag{4.32}$$

$$h_{13}=\frac{e^{0.5\mathrm{Re}13}-1}{e^{\mathrm{Re}13}-1} \qquad h_{31}=\frac{e^{\mathrm{Re}13}-e^{0.5\mathrm{Re}13}}{e^{\mathrm{Re}13}-1} \qquad \mathrm{Re}_{13}=\frac{\rho}{\mu}\left[\frac{1}{2}\left(\underline{u}_c^1+\underline{u}_c^3\right)\cdot\left(\underline{x}_3-\underline{x}_1\right)\right] \tag{4.33}$$

$$h_{14}=\frac{e^{0.5\mathrm{Re}14}-1}{e^{\mathrm{Re}14}-1} \qquad h_{41}=\frac{e^{\mathrm{Re}14}-e^{0.5\mathrm{Re}14}}{e^{\mathrm{Re}14}-1} \qquad \mathrm{Re}_{14}=\frac{\rho}{\mu}\left[\frac{1}{2}\left(\underline{u}_c^1+\underline{u}_c^4\right)\cdot\left(\underline{x}_4-\underline{x}_1\right)\right] \tag{4.34}$$

$$h_{23}=\frac{e^{0.5\mathrm{Re}23}-1}{e^{\mathrm{Re}23}-1} \qquad h_{32}=\frac{e^{\mathrm{Re}23}-e^{0.5\mathrm{Re}23}}{e^{\mathrm{Re}23}-1} \qquad \mathrm{Re}_{23}=\frac{\rho}{\mu}\left[\frac{1}{2}\left(\underline{u}_c^2+\underline{u}_c^3\right)\cdot\left(\underline{x}_3-\underline{x}_2\right)\right] \tag{4.35}$$

$$h_{24}=\frac{e^{0.5\mathrm{Re}24}-1}{e^{\mathrm{Re}24}-1} \qquad h_{42}=\frac{e^{\mathrm{Re}24}-e^{0.5\mathrm{Re}24}}{e^{\mathrm{Re}24}-1} \qquad \mathrm{Re}_{24}=\frac{\rho}{\mu}\left[\frac{1}{2}\left(\underline{u}_c^2+\underline{u}_c^4\right)\cdot\left(\underline{x}_4-\underline{x}_2\right)\right] \tag{4.36}$$

$$h_{34}=\frac{e^{0.5\mathrm{Re}34}-1}{e^{\mathrm{Re}34}-1} \qquad h_{43}=\frac{e^{\mathrm{Re}34}-e^{0.5\mathrm{Re}34}}{e^{\mathrm{Re}34}-1} \qquad \mathrm{Re}_{34}=\frac{\rho}{\mu}\left[\frac{1}{2}\left(\underline{u}_c^3+\underline{u}_c^4\right)\cdot\left(\underline{x}_4-\underline{x}_3\right)\right] \tag{4.37}$$

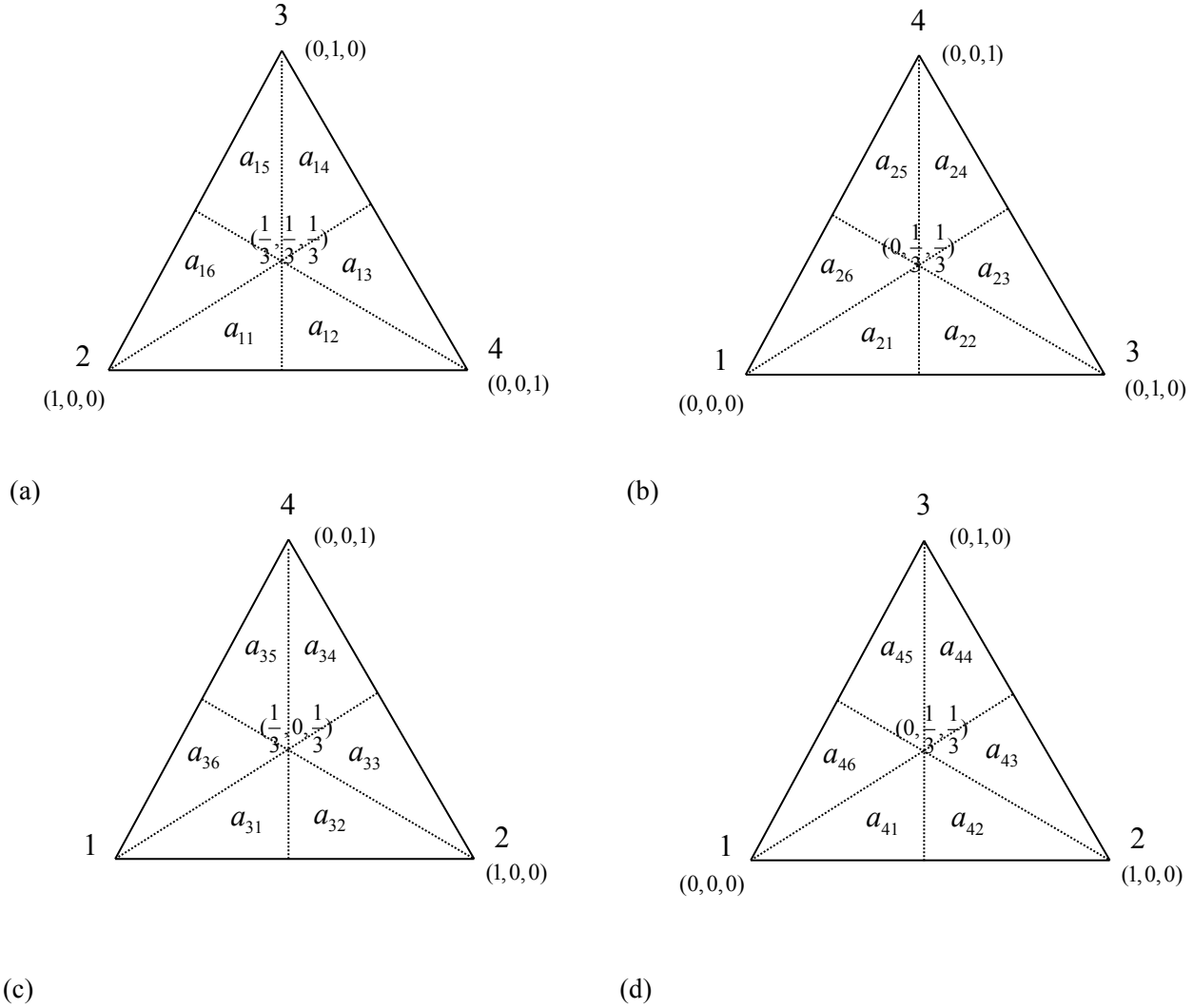

(Fig. 4.11) Faces of regions and definition of sub-regions as defined by the set of coordinates $(\xi_0, \eta_0, \alpha_0)$:

(a) element face at region 1 (w_1) (b) element face at region 2 (w_2)

(c) element face at region 3 (w_3) (d) element face at region 4 (w_4)

The scheme has the following properties:

- Stability of the solution is achieved.
- Compatibility of velocity values at the borders of the neighboring regions is satisfied.
- Completeness condition of the interpolation is satisfied, i.e. $\sum h_i^v = 1$.
- Interpolation is independent from the node numbering.
- Interpolation is independent of the rotation of the Cartesian coordinate orientation.
- Convergence of V_h to U_h for small element Reynolds number is reached.
- FCBI functions are always positive and less than or equal to 1.

The line that joins the barycenter node and a given flux calculation point (ξ,η,α) intersects the element side at a point denoted (ξ_0,η_0,α_0) (see figure 4.8). Geometrically, the trial functions in V_h are linear between the centroid and (ξ_0,η_0,α_0), and the interpolations of the element faces are calculated based on the analytical solution of the advection-diffusion equation. This scheme can be written as follows:

$$v_{||}^1 = \frac{\sqrt{(\xi-\frac{1}{4})^2+(\eta-\frac{1}{4})^2+(\alpha-\frac{1}{4})^2}}{\sqrt{(\xi_0-\frac{1}{4})^2+(\eta_0-\frac{1}{4})^2+(\alpha_0-\frac{1}{4})^2}}\left\{f_2^{(1)}v_{2||}+f_3^{(1)}v_{3||}+f_4^{(1)}v_{4||}\right\}+\frac{\sqrt{(\xi_0-\xi)^2+(\eta_0-\eta)^2+(\alpha_0-\alpha)^2}}{\sqrt{(\xi_0-\frac{1}{4})^2+(\eta_0-\frac{1}{4})^2+(\alpha_0-\frac{1}{4})^2}}v_{5||}$$
$$=(4\xi+4\eta+4\alpha-3)f_2^{(1)}v_{2||}+(4\xi+4\eta+4\alpha-3)f_3^{(1)}v_{3||}+(4\xi+4\eta+4\alpha-3)f_4^{(1)}v_{4||}+4(1-\xi-\eta-\alpha)v_{5||} \quad (4.38)$$

$$v_{||}^2 = \frac{\sqrt{(\xi-\frac{1}{4})^2+(\eta-\frac{1}{4})^2+(\alpha-\frac{1}{4})^2}}{\sqrt{\frac{1}{16}+(\eta_0-\frac{1}{4})^2+(\alpha_0-\frac{1}{4})^2}}\left\{f_1^{(2)}v_{1||}+f_3^{(2)}v_{3||}+f_4^{(2)}v_{4||}\right\}+\frac{\sqrt{(\xi_0-\xi)^2+(\eta_0-\eta)^2+(\alpha_0-\alpha)^2}}{\sqrt{\frac{1}{16}+(\eta_0-\frac{1}{4})^2+(\alpha_0-\frac{1}{4})^2}}v_{5||}$$
$$=(1-4\xi)f_1^{(2)}v_{1||}+(1-4\xi)f_3^{(2)}v_{3||}+(1-4\xi)f_4^{(2)}v_{4||}+4\xi v_{5||} \quad (4.39)$$

$$v_{||}^{3}=\frac{\sqrt{(\xi-\frac{1}{4})^2+(\eta-\frac{1}{4})^2+(\alpha-\frac{1}{4})^2}}{\sqrt{(\xi_0-\frac{1}{4})^2+\frac{1}{16}+(\alpha_0-\frac{1}{4})^2}}\left\{f_1^{(3)}v_{1||}+f_2^{(3)}v_{2||}+f_4^{(3)}v_{4||}\right\}+\frac{\sqrt{(\xi_0-\xi)^2+(\eta_0-\eta)^2+(\alpha_0-\alpha)^2}}{\sqrt{(\xi_0-\frac{1}{4})^2+\frac{1}{16}+(\alpha_0-\frac{1}{4})^2}}v_{5||}$$

$$=(1-4\eta)f_1^{(3)}v_{1||}+(1-4\eta)f_2^{(3)}v_{2||}+(1-4\eta)f_4^{(3)}v_{4||}+4\eta v_{5||} \tag{4.40}$$

$$v_{||}^{4}=\frac{\sqrt{(\xi-\frac{1}{4})^2+(\eta-\frac{1}{4})^2+(\alpha-\frac{1}{4})^2}}{\sqrt{(\xi_0-\frac{1}{4})^2+(\eta_0-\frac{1}{4})^2+\frac{1}{16}}}\left\{f_1^{(4)}v_{1||}+f_2^{(4)}v_{2||}+f_3^{(4)}v_{3||}\right\}+\frac{\sqrt{(\xi_0-\xi)^2+(\eta_0-\eta)^2+(\alpha_0-\alpha)^2}}{\sqrt{(\xi_0-\frac{1}{4})^2+(\eta_0-\frac{1}{4})^2+\frac{1}{16}}}v_{5||}$$

$$=(1-4\alpha)f_1^{(4)}v_{1||}+(1-4\alpha)f_2^{(4)}v_{2||}+(1-4\alpha)f_3^{(4)}v_{3||}+4\alpha v_{5||} \tag{4.41}$$

Note that the unsteady part of equation (4.9) has to contain the term with the time rate of change of the nodal mass. Applying the Petrov-Galerkin variational formulation and the finite element discretization, the first term of equation (4.9) is divided into two parts (see equation (2.8)). Weighting and finite element discretization makes the equation easily differentiable

$$\frac{d}{dt}\int_{\Omega} w\,[\rho\underline{u}]\,d\Omega=\frac{d}{dt}(M\underline{\hat{u}})=\frac{dM}{dt}\underline{\hat{u}}+M\frac{d\underline{\hat{u}}}{dt}=\frac{dM}{dt}\underline{\hat{u}}+M\underline{\hat{a}} \tag{4.42}$$

where w is the weight function of the momentum equation, which is a unit step function for the FCBI method, M is the mass matrix, and $\underline{\hat{u}}$ and $\underline{\hat{a}}$ are respectively a nodal velocity vector and a nodal acceleration vector. As we observe from the relation (4.42), the inertia is highly dependent on the configuration change of the mesh. For calculation of the inertia term, we define the rate of mass change and the acceleration using the trapezoidal rule of time integration.

4.1.2 Penalty method for stabilization

Since the problem is highly nonlinear and unsteady, the values of the barycenter node requires additional stabilization. Due to the small center volume resulting from the nature of the tetrahedral geometry, it can introduce singular behaviors. To bind the barycenter node, and prohibit uncontrolled behavior, we apply a very slight penalty that grows if the center node velocity values are much different from the average velocity of the four corner nodes of the element. Since the method should not enforce the barycenter velocity to have a value as boundary condition, the penalty should provide stability without affecting the whole calculation [16]. The Petrov-Galerkin variational formulation is as in reference [26]. Therefore the new momentum equation with the penalty function is written as:

$$\frac{d}{dt}\int_{\Omega} w\,[\rho \underline{u}]\,d\Omega + \int_{\Gamma} w\,[\rho \underline{v}\{(\underline{u}-\underline{u}_m)\cdot\underline{n}\}]\,d\Gamma - \int_{\Gamma} w\,[\underline{\tau}(\underline{u},p)\cdot\underline{n}]\,d\Gamma$$
$$+\lambda \underline{e}_5^T(\underline{u}_5 - \frac{1}{4}(\underline{u}_1+\underline{u}_2+\underline{u}_3+\underline{u}_4)) = \int_{\Omega} w\,[\rho \underline{g}]\,d\Omega \qquad (4.43)$$

The additional force and the stiffness due to the penalty are as follows:

$$F_5^* = \lambda(\underline{u}_5 - \frac{1}{4}(\underline{u}_1+\underline{u}_2+\underline{u}_3+\underline{u}_4)) \qquad (4.44)$$

$$K_{51}^* = -\frac{\lambda}{4},\ K_{52}^* = -\frac{\lambda}{4}, K_{53}^* = -\frac{\lambda}{4},\ K_{54}^* = -\frac{\lambda}{4},\ K_{55}^* = \lambda \qquad (4.45)$$

For the correct solution of the Navier-Stokes equations and applying only a slight bounding for stability, we use λ as small as 10^{-3} times the stiffness entries of the maximum absolute value of the 5th row which corresponds to the momentum equation of the center node.

Although it slightly changes the value of the momentum, the change induced by this very slight penalty is negligible, on the order of 10^{-5} or so, yet it makes the method remarkably stable by applying a numerical barrier that prevents the solution from behaving uncontrollably.

4.2 Numerical examples of 3-D problems

In this section, the 3-D FCBI scheme is verified with 3-D example problems taken from two references. First we solve the unsteady 2-D like, wall driven cavity flow problem, and compare our solutions to the results provided by Ghia et al. [27] and Kohno et al. [11]. We then analyze the solution of a 2-D like sloshing problem. Lastly, we show a comparison in the analysis of a purely 3-D sloshing problem.

4.2.1 Steady-state problem

Here, we calculate and show the results for a wall-driven cavity flow, in which the top rigid wall is moving in one direction with a unit velocity $\underline{u}_d = [1\ 0\ 0]^T$, while three confining walls, at the left, the right and the bottom, are stationary. This is a benchmark problem to evaluate the validity of fluid solution schemes. The results shown first contain a comparison with a rather coarse mesh (figure 4.17); the next comparison is done with a finer mesh (figure 4.20). All results are compared with results from reference [27] which were obtained with a finite difference scheme and very fine meshes, and results from reference [11], obtained with the 2-D FCBI scheme with meshes that have various mesh densities. Figures 4.15 shows the vector plot obtained by H. Kohno and K.J. Bathe [11], while figure 4.16 shows the vector plot obtained with our solution method. Mesh densities in this problem conform with mesh densities provided in reference [11] in order to verify the mesh effectiveness of the scheme.

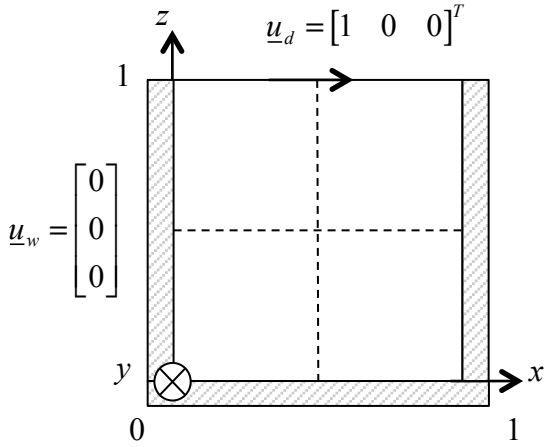

(Fig. 4.12) Square cavity problem definition ($0 \le x \le 1,\ 0 \le y \le 1,\ 0 \le z \le 1$)

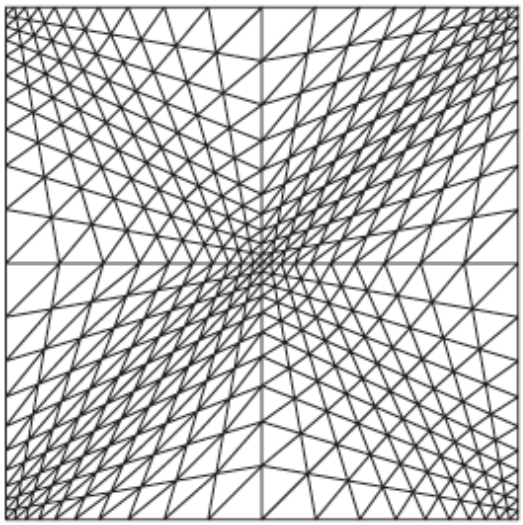

(Fig. 4.13) A coarse 2-D FCBI mesh [11]

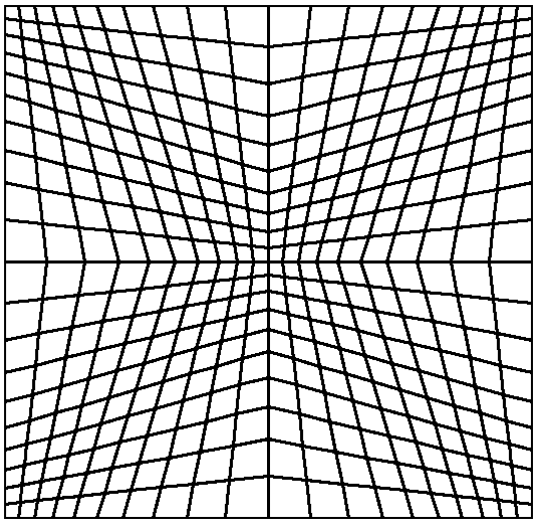

(Fig. 4.14) A coarse 3-D FCBI mesh for comparison

Note $\frac{\Delta x_{\max}}{\Delta x_{\min}} = \frac{\Delta z_{\max}}{\Delta z_{\min}} = 5$

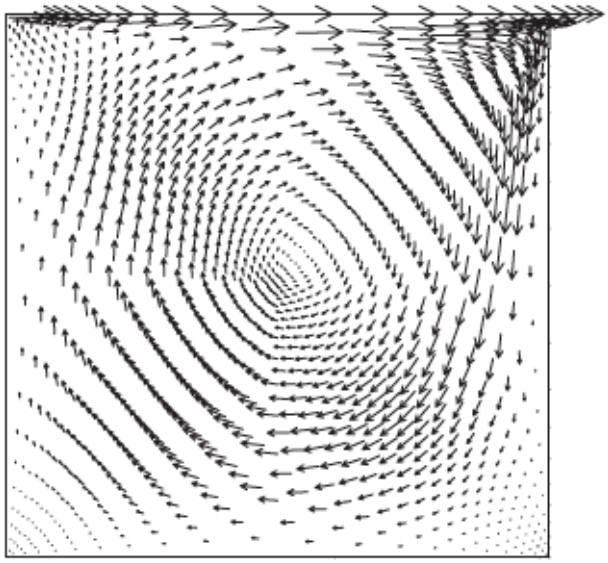

(Fig. 4.15) A velocity vector plot calculated with the mesh in figure 4.13

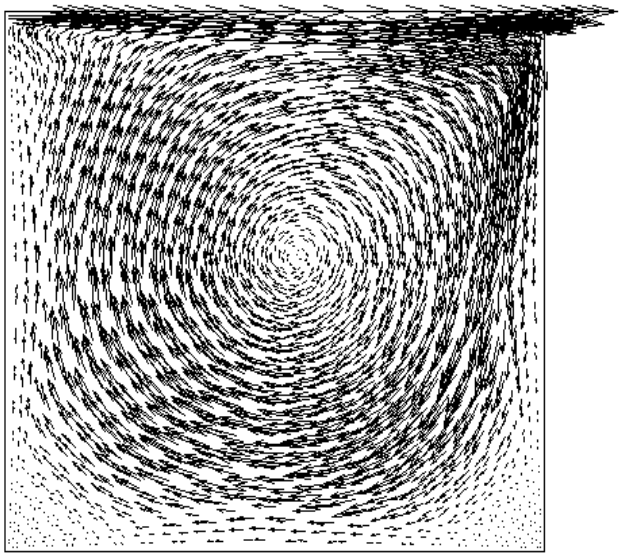

(Fig. 4.16) A velocity vector plot calculated with the mesh in figure 4.14

Figure 4.12 shows the geometry of the square cavity with the coordinate system. The no-slip boundary condition is imposed on the left, lower and right boundaries, while a unit velocity is prescribed on the upper wall including the corners. In addition, zero pressure is prescribed at the lower left front corner, at $(x, y, z) = (0, 0, 0)$. Originally, this problem is a two-dimensional problem. However, this can also be applied to three-dimensional solution schemes by applying forward and backward slip boundary walls. A mesh of 20×20 quadrilaterals that contain 2 triangular elements, used for calculation in reference [11], is drawn in figure 4.13. The 20×4×20 (in x, y and z direction, respectively) hexahedra that we used for calculating the 3-D FCBI results are shown in figure 4.14. The calculation is performed with Reynolds number 1,000. We define the Reynolds number as follows:

$$\mathrm{Re} = \frac{\rho |\underline{u}_d| l}{\mu} = \frac{\rho}{\mu} \tag{4.46}$$

where l is the length of the side of the cavity which is 1.

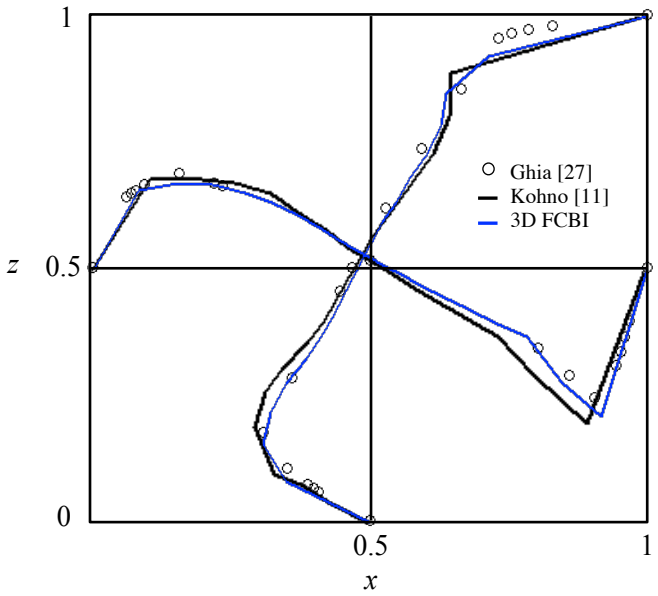

(Fig. 4.17) A vertical velocity profile at a horizontal mid-surface at $z = 0.5$ and a horizontal velocity profile at a vertical mid-surface at $x = 0.5$. The results from reference [11] and from the 3-D FCBI method correspond to the coarse meshes shown in figures 4.13 and 4.14.

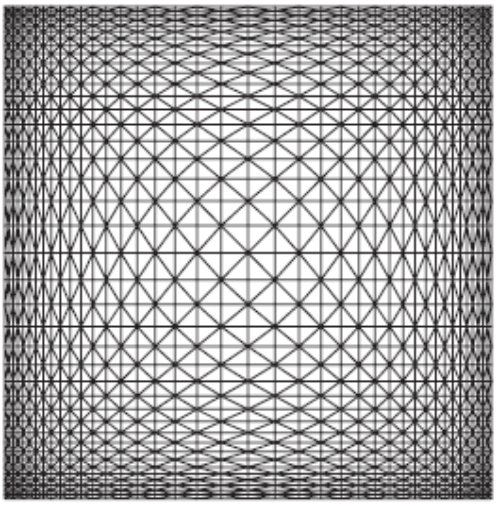

(Fig. 4.18) A finer 2-D FCBI mesh [11]

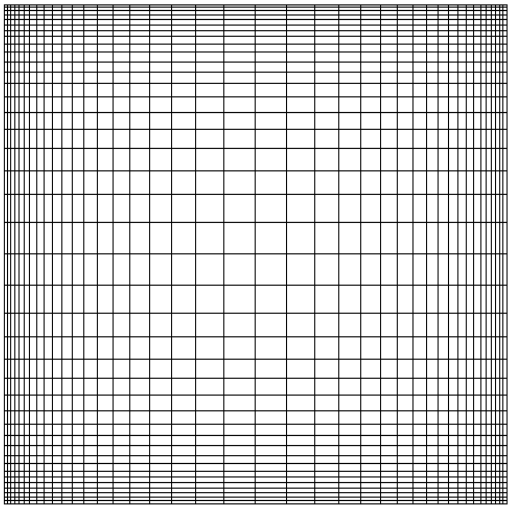

(Fig. 4.19) A finer 3-D FCBI for comparison

The second mesh configurations used for comparison at Reynolds numbers 1,000 and 10,000 are shown in figures 4.18 and 4.19. The mesh density is again the same. The mesh shown in figure 4.18 has 40 quadrilaterals in each direction x, z. Figure 4.19 shows the projected view in the x-z of the mesh $40\times4\times40$ hexahedra. Figure 4.20 shows the horizontal and vertical velocity profiles at mid-surfaces at Reynolds numbers 1,000 and 10,000. The figure shows similar behavior with the 2-D FCBI results [11] and agrees very well with Ghia's results, but shows much better quality than the results using linear interpolations in figure 4.20(b)

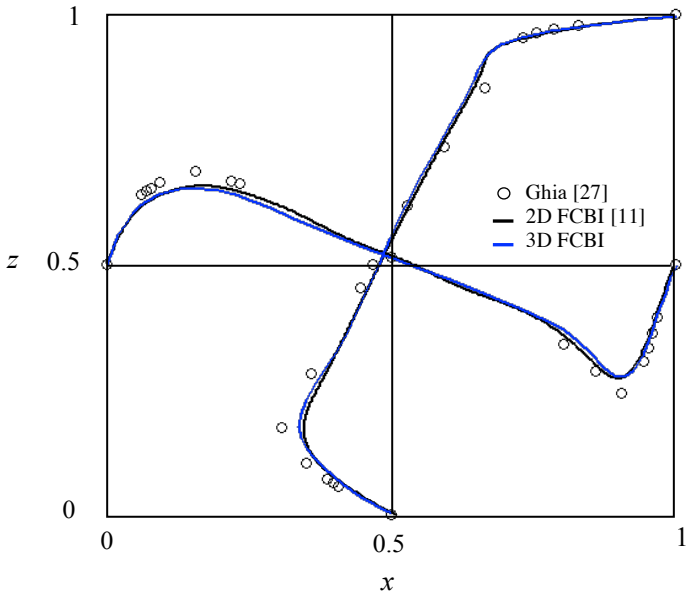

(a)

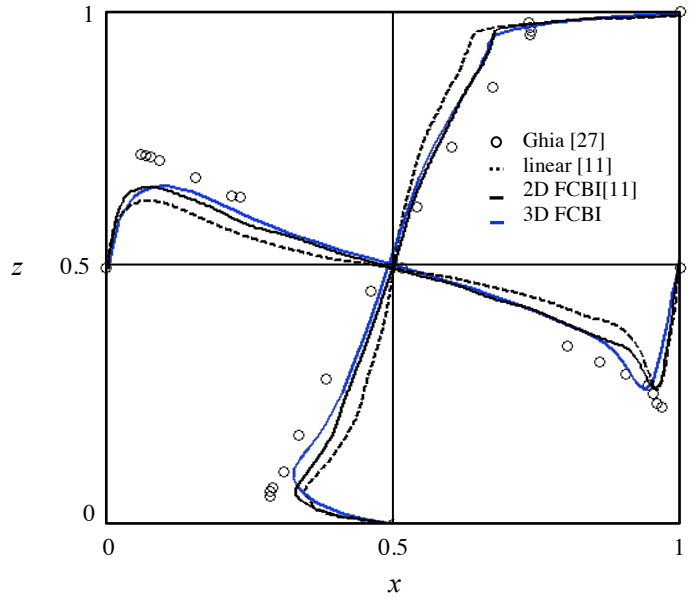

(b)

(Fig. 4.20) A vertical velocity profile at a horizontal mid-surface at $z = 0.5$ and a horizontal velocity profile at a vertical mid-surface at $x = 0.5$. The results from reference [11] and from the 3-D FCBI method correspond to the fine meshes shown in figures 4.18 and 4.19.
(a) Re= 1,000 (b) Re=10,000

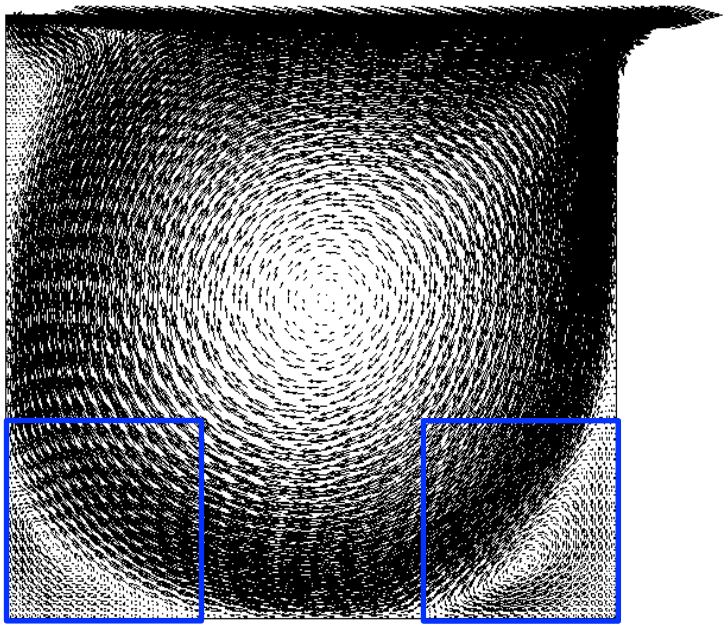

(a)

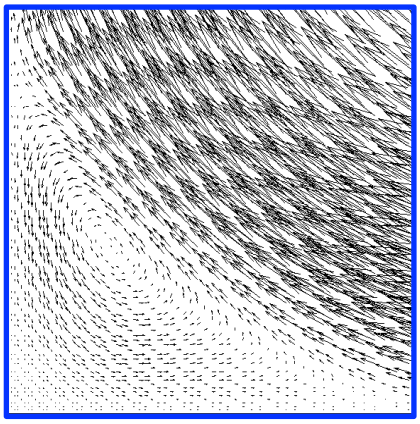

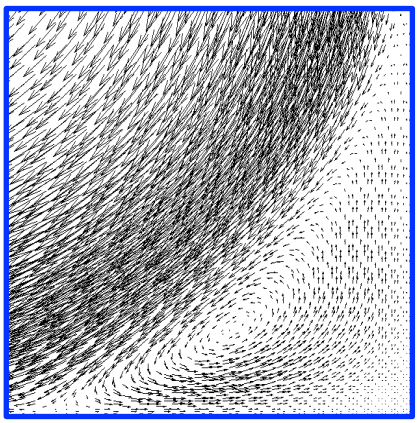

(b) (c)

(Fig. 4.21) Velocity vector plot of 3-D FCBI calculated with the fine mesh shown in figure 4.19 with Re =10,000:

(a) overall vector plot

(b) left corner recirculation around $(x, z) = (0, 0)$

(c) right corner recirculation around $(x, z) = (0, 1)$

4.2.2 Two-dimensional-like free surface problem

In this section, we perform a sloshing simulation in which the fluid is excited in one direction, in order to maintain symmetry and compare with experimental data. This problem demonstrates the validity of the dynamic responses of the solution. In particular, the scheme should conserve mass. Also, the dynamic response of the three-dimensional scheme should maintain the symmetry of the input loading even through the mesh itself is not symmetric. As shown below in figure 4.22, an open tank that contains water is excited in the x-direction only. The results satisfy symmetry throughout computational times and agree with the experimental and numerical results from reference [28]. The excitation input is given as $x = 0.005(1-\cos 6.85t)$, where t refers to the time. The time step size employed in the reference is 0.001 second and the 3-D FCBI solution was calculated with the time step of $\Delta t = 0.03\,\text{sec}$, which is 30 times bigger than the reference paper's time step size.

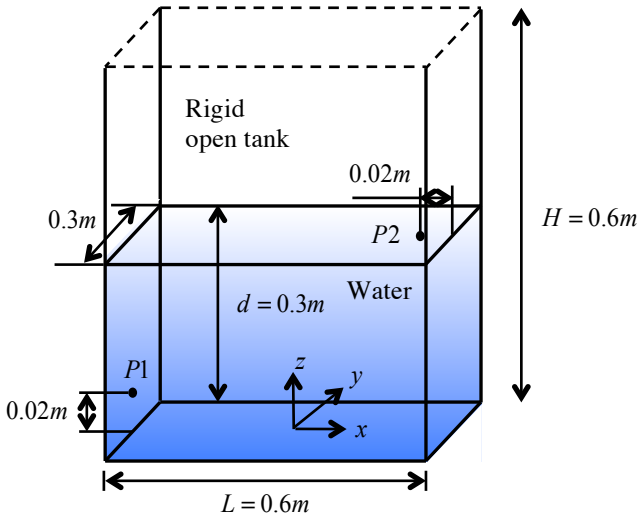

(Fig. 4.22) Problem definition and parameters for liquid sloshing in a rectangular tank

The 3-D FCBI case shows very stable results even with large time steps and no special treatments or variables contrarily to reference [28] which resorts to a "weighting value λ" . The resulting mass conservation error calculated in the FCBI solution is 0.0923%, while the reference admits that its suggested method suffers from conservation errors.

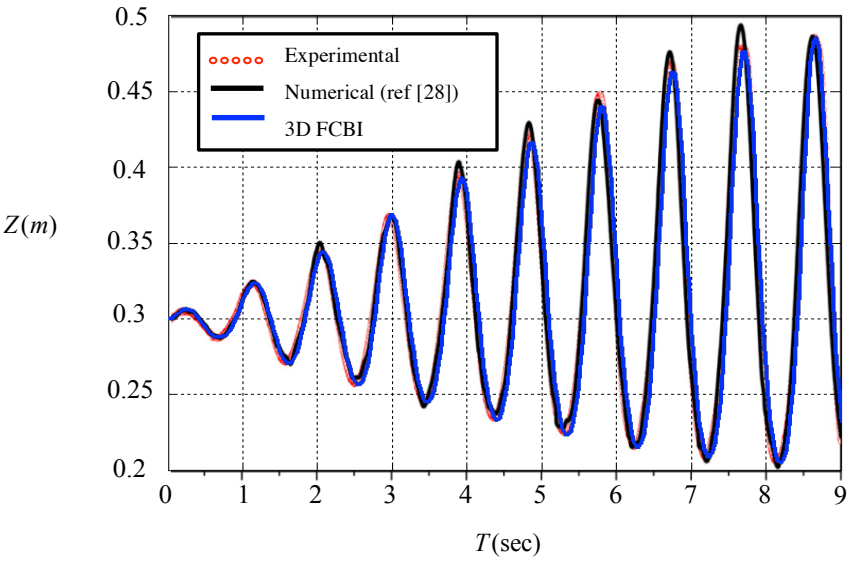

(Fig. 4.23) Time history of the height at the reference point P2

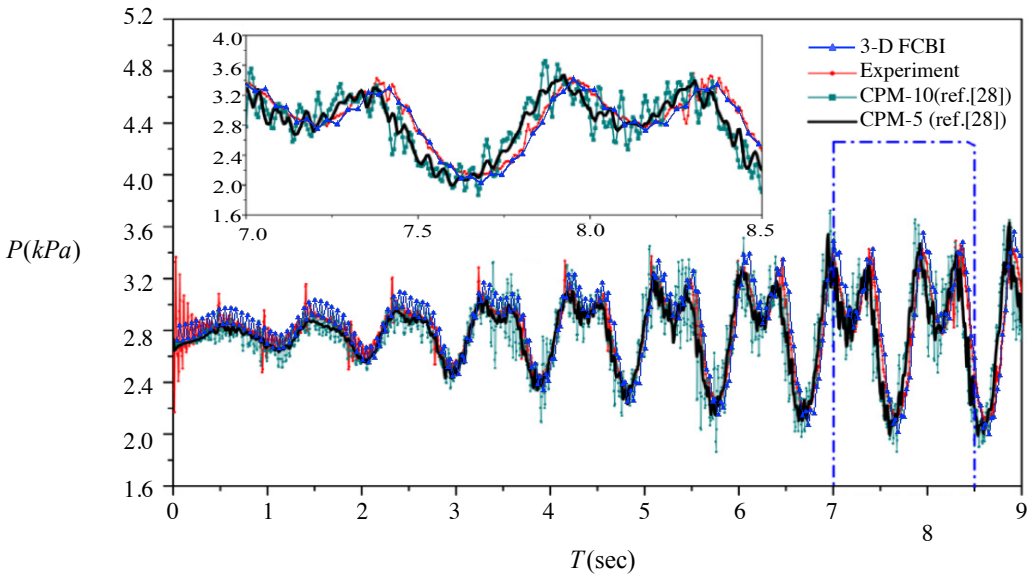

(Fig. 4. 24) Time history of the pressure at the reference point P1

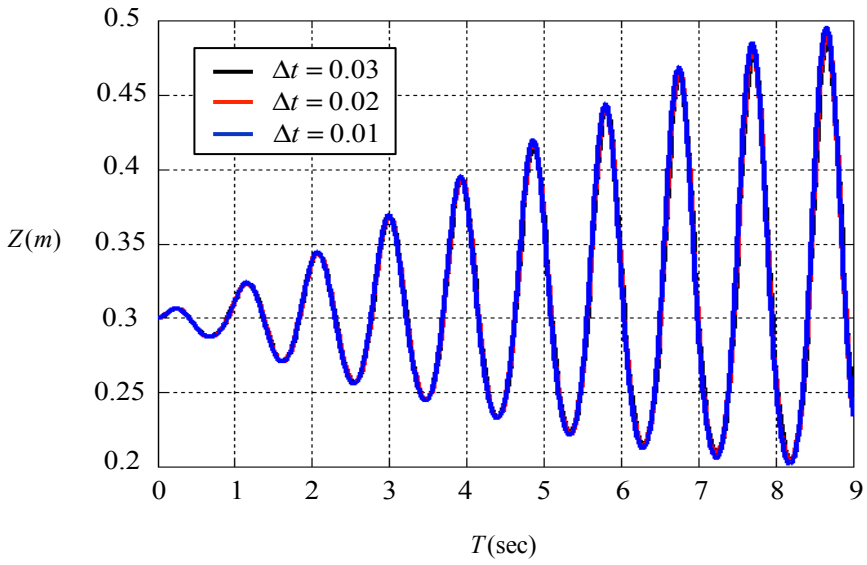

(Fig. 4. 25) Time history of z coordinate at point P2 due to different time step sizes

The results shown in figure 4.23-4.25 are calculated with meshes of 784 (14×4×14) hexahedra, or 4704 elements. As figures 4.24 and 4.25 show, the results from the proposed method match well with the experimental results of reference [28]. Because of the benefit of the robustness of the trapezoidal time advancing method, the figure 4.25 shows the independence of the solution from the time step sizes used. The figure below (figure 4.26) shows the results of the height history with different mesh densities. The results show more sensitivity to the mesh sizes because the problem induces large curvatures of the free surface interface, which finer meshes are more adapted to. We next define the generic element size as equation (4.47) (see figure 4.27).

$$h = \sqrt{(\Delta x)^2 + (\Delta z)^2} \tag{4.47}$$

$$E_n = \sqrt{\sum_{i=1}^{T} (Z_i^n - Z_i^{ref})^2} \tag{4.48}$$

where the Z_i's are the z-coordinates of point P2 at time step i. In equation 4.48, n is an index that labels the four different sizes of elements in meshes whose results are shown in figures 4.26 and 4.8. Reference values in equation (4.48) are calculated with a fine mesh that has 9,600 elements.

The generic element size was chosen as in equation (4.47) because the problem is symmetric in the y- direction and the y-directional mesh size does not play a role in convergence. In other words, even though the problem is calculated with 3 dimensional tetrahedral elements, the solution should not depend on the length in the y-direction, therefore, the element length does not take the y directional length into account. The convergence results are shown in figure 4.28. We find an overall convergence rate of 2.5832, which corresponds to a 2nd order convergence.

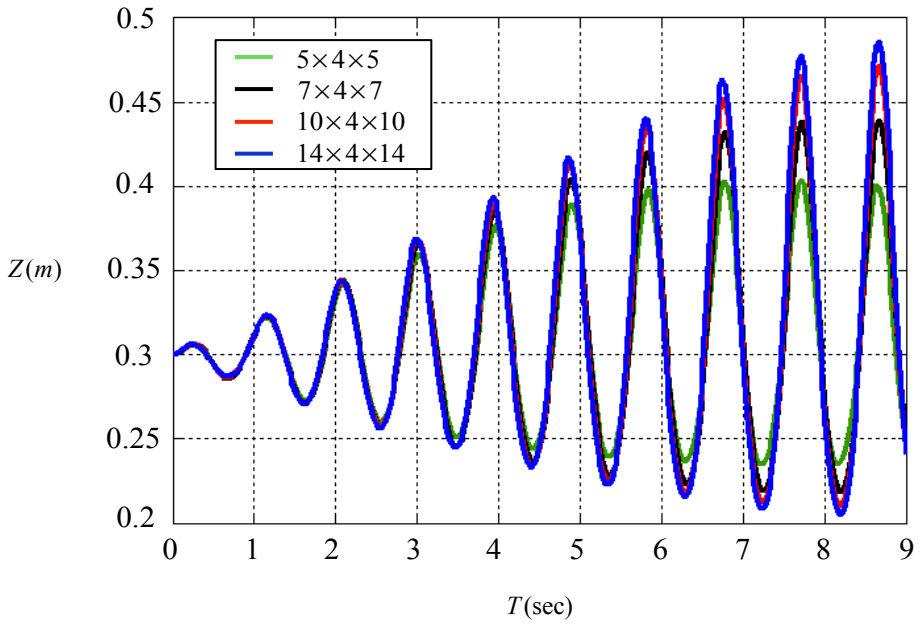

(Fig. 4.26) Time history of z coordinate at point P2 due to different element sizes

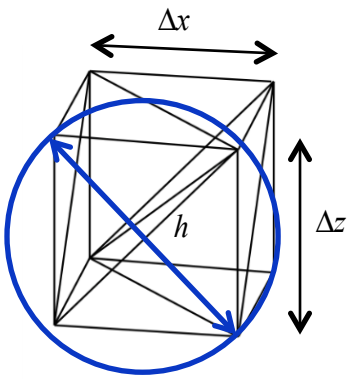

(Fig. 4.27) Measurement of the generic element sizes for the 2-D like free surface problem

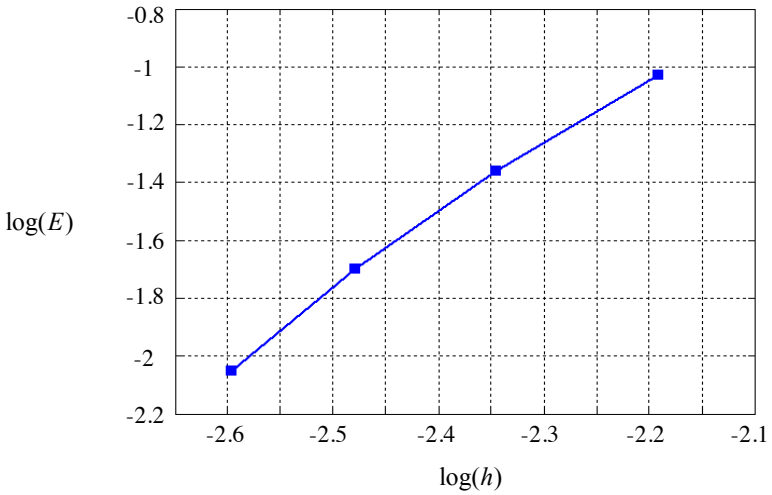

(Fig. 4.28) Convergence plot of the 2-D like sloshing problem

4.2.3 Three-dimensional free surface problem

The third 3-dimensional numerical example is a pure 3-dimensional sloshing problem excited with a near-resonance displacement input. The purpose of solving this problem is to illustrate the accuracy of the solution scheme in a true three-dimensional sloshing problem. The 3-dimensional analysis is the main focus of this thesis, and is important because, in practice, most free surface problems are 3-dimensional. Figure 4.29 shows the dimensions and parameters of the problem.

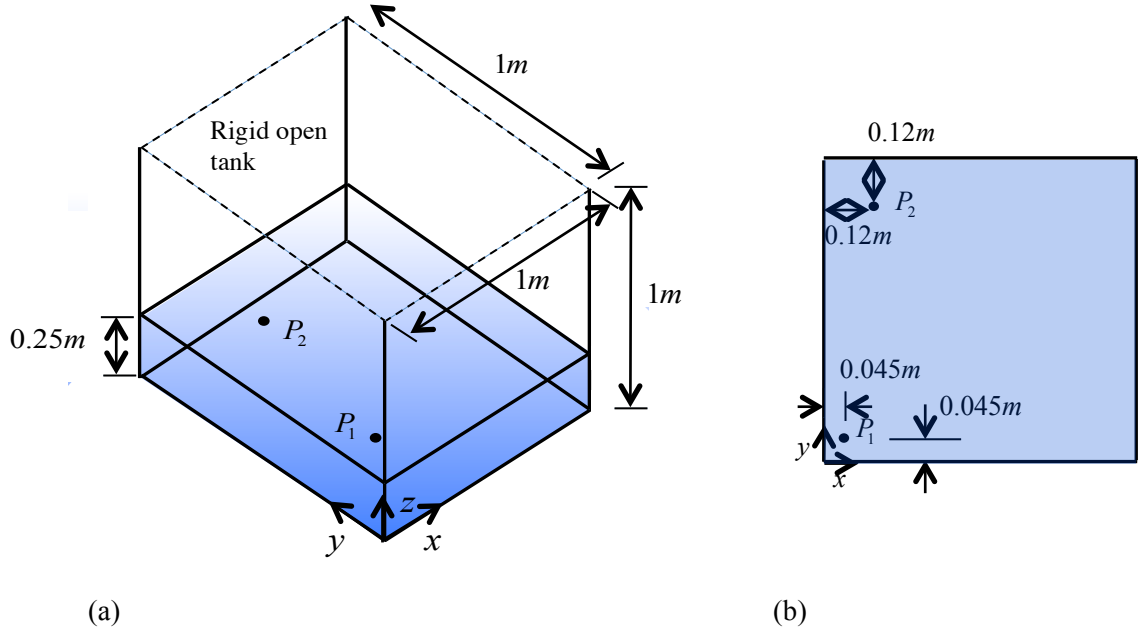

(Fig. 4.29) Definition of parameters for 3-D liquid sloshing in a rectangular tank
(a) iso-view of tank
(b) plan-view of tank with the locations of the calculation points

The open tank is excited with the displacements $d_x = 0.005\sin(0.93\omega_1 t)\cos 30°$ and $d_y = 0.005\sin(0.93\omega_1 t)\sin 30°$ in the x-direction and y-direction, respectively. The excitation frequency is given as $0.93\omega_1$. The natural frequency is calculated as:

$$\omega_1 = \sqrt{g\pi \tanh(\pi h)} = 4.4957\,\text{sec}^{-1} \qquad \text{where} \quad h = 0.25m \qquad \text{(Eq. 4.49)}$$

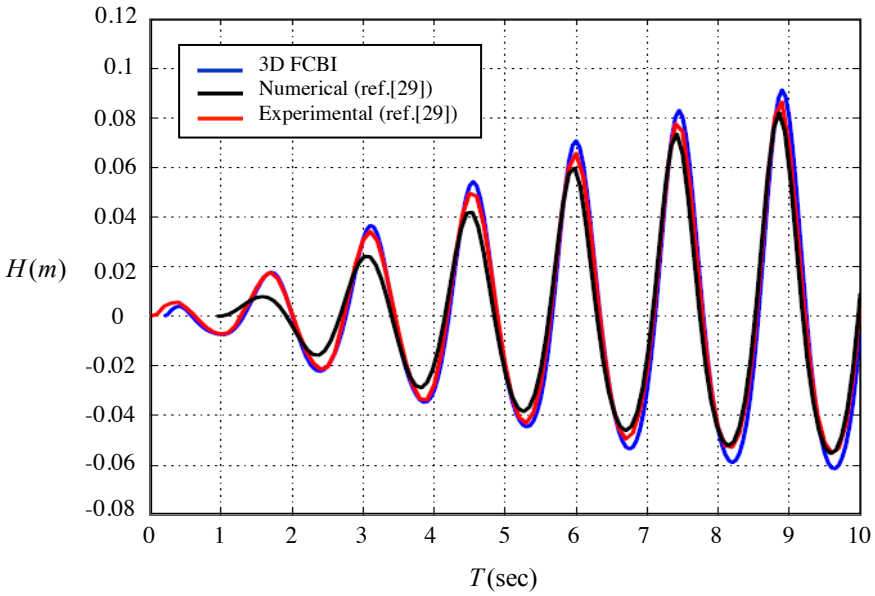

(Fig. 4.30) Time history of the height of reference point P2.
A 15×15×8 mesh (1800 hexahedra, 10,800 (=1800×6) tetrahedral elements) was used for the 3-D FCBI method

Note that H is the height (z-coordinate) of P2 measured from the undisturbed equilibrium position. Figure 4.30 shows the height history of point P2, illustrated in Figure 4.29. The simulation results of 3-D FCBI are very similar to the experimental results, especially for the early times. Since the problem's excitation velocity is very abruptly applied at time $t = 0$, the early stage puts an emphasis on the correct calculation of the unsteady effect.

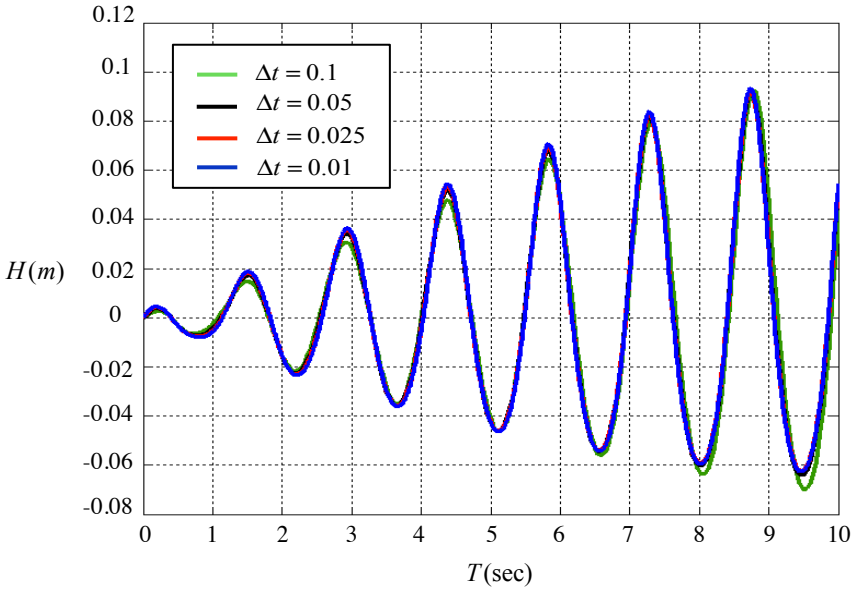

(Fig. 4.31) Time history of the height at point P2 due to different time step sizes
We used a 15×15×8 mesh for those calculations.

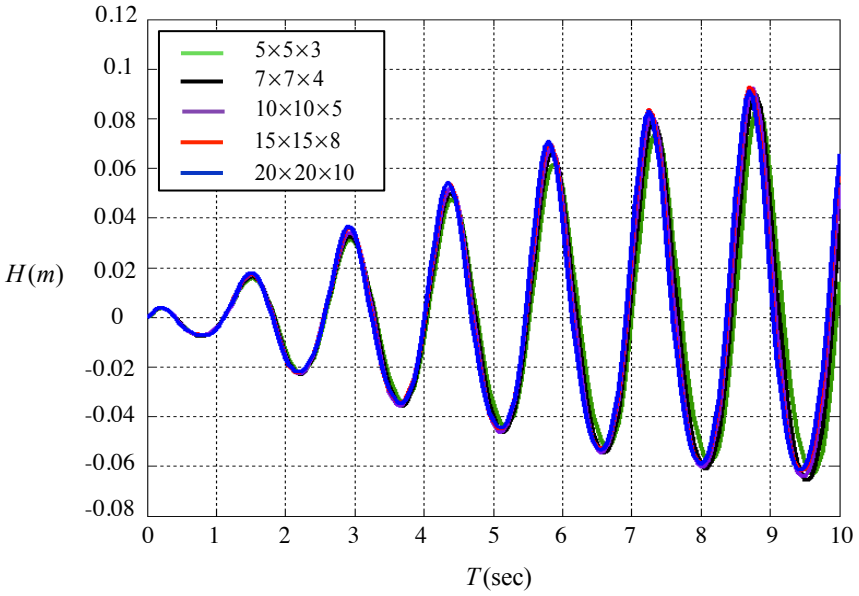

(Fig. 4.32) Time history of the height at point P2 due to different element sizes
with $\Delta t = 0.05\,\text{sec}$

Since this case does not have symmetry and is purely 3-dimensional, the element length is defined as the length of the 3-dimensional diagonal of the initial mesh configuration (see figure 4.33). Since the time step sizes have a very small influence on the results, the convergence study is performed only with different mesh sizes (see equations (4.50) and (4.51) for the definitions used). The overall convergence rate is calculated to be 2.2932 which is close to 2^{nd} -order convergence.

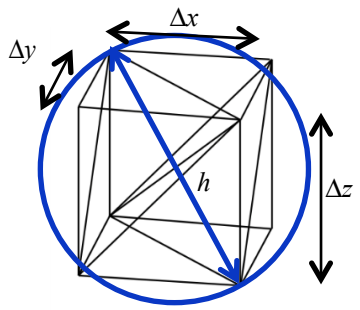

(Fig.4.33) Measurement of the generic element sizes for the 3-D free surface problem

$$h = \sqrt{\Delta x^2 + \Delta y^2 + \Delta z^2} \tag{4.50}$$

$$E_n = \sqrt{\sum_{i=1}^{T} (H_i^n - H_i^{ref})^2} \tag{4.51}$$

where reference values H^{ref} are calculated with the fine mesh which has 24,000 elements.

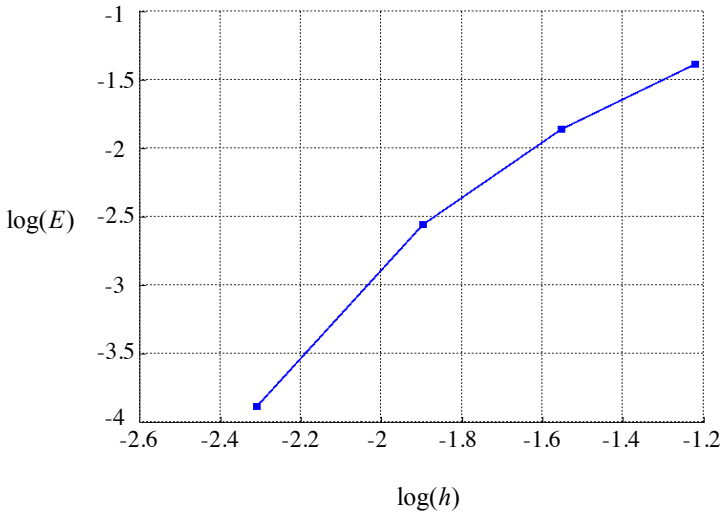

(Fig. 4.34) The convergence plot of the 3-D sloshing problem

Chapter 5

Conclusions

We have developed an efficient and accurate algorithm for solving free surface and multi-phase fluid flow problems, using an FCBI formulation for 3-node triangular elements and 4-node tetrahedral elements of moving domains. The newly developed 3-D tetrahedral FCBI formulation facilitates remarkably accurate dynamic response solutions of flows and, in particular, mass conservation, thus improving the reliability of the simulations. The contribution to the development of the 3-D FCBI solution scheme is based on the proper derivation of an ALE formulation using the Reynolds transport theorem. We then achieved stable and accurate solutions, even with relatively coarse meshes and large time steps. The proposed method was validated and very good agreement with experimental data from reference papers was found.

We achieved accurate solutions using structured meshes. However, more benefits would be observed using unstructured meshes needed for more complicated geometries, which tetrahedral elements can easily handle. More challenging problems to tackle will be the breakage of interfaces, i.e. splashes of free surface flows.

These problems might be solved by a mixture of classical ALE approaches and Lagrangian separated domain approaches [30]. This is the most physically intuitive solution scheme and this

would be compatible with the original solution scheme presented in this thesis. A similar but different approach in this context would rely on the use of a meshless method. A well-known one is the smoothed particle hydrodynamics (SPH) scheme which was suggested in reference [31]. It is a good tool to be used with ALE but requires treatments to be set. The SPH method defines a fluid domain as a set of particles that possess material properties and interact with each other [32]. The SPH method has the additional benefit of not having to generate meshes. Although SPH is known as the oldest modern particle method and widely used, there are highly promising meshless methods, such as the "method of finite spheres" (MFS), which has been validated by its usage in wave propagation analyses [33]. The MFS is a mesh-less method which defines the computational domain as a set of spheres that overlap. It has additional strength in that it eliminates limitations of SPH, such as boundary deficiency or the use of artificially set solution parameters [33, 34].

Appendix A

Some details regarding the FCBI scheme

Calculation of ξ_0, η_0, α_0 in each region

Region 1

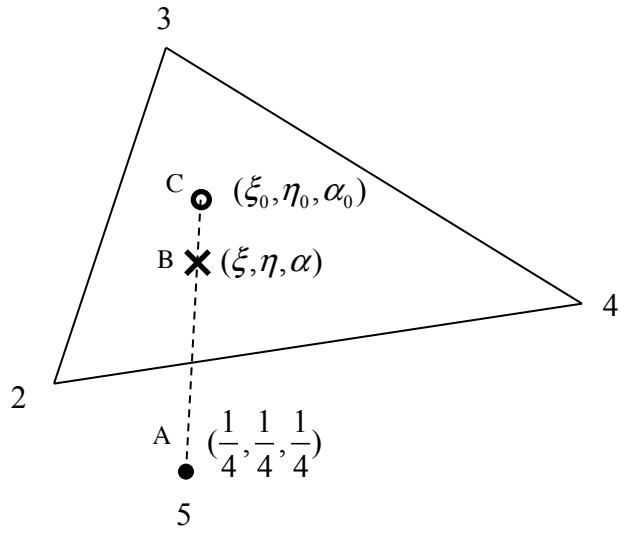

(Fig. A.1) Projection of the flux calculation point in region 1 from the barycenter node to the element face

In region 1, the relation $\xi_0 + \eta_0 + \alpha_0 = 1$ and the vector addition $\underline{C} = \underline{A} + t_0(\underline{B} - \underline{A})$ hold (see figure A.1).

From these relations, the constant t_0 and coordinates are calculated as follows:

$$t_0 = \frac{0.25}{\xi + \eta + \alpha - 0.75} \tag{A.1}$$

$$\xi_0 = 0.25 + t_0(\xi - 0.25) \tag{A.2}$$

$$\eta_0 = 0.25 + t_0(\eta - 0.25) \tag{A.3}$$

$$\alpha_0 = 0.25 + t_0(\alpha - 0.25) \tag{A.4}$$

In region 2, the calculation method is similar to the case of region 1, with $\xi_0 = 0$.

$$\eta_0 = 0.25 + \frac{0.25(\eta - 0.25)}{0.25 - \xi} \tag{A.5}$$

$$\alpha_0 = 0.25 + \frac{0.25(\alpha - 0.25)}{0.25 - \xi} \tag{A.6}$$

In region 3, $\eta_0 = 0$ is satisfied.

$$\xi_0 = 0.25 + \frac{0.25(\xi - 0.25)}{0.25 - \eta} \tag{A.7}$$

$$\alpha_0 = 0.25 + \frac{0.25(\alpha - 0.25)}{0.25 - \eta} \tag{A.8}$$

In region 4, $\alpha_0 = 0$ is satisfied.

$$\xi_0 = 0.25 + \frac{0.25(\xi - 0.25)}{0.25 - \alpha} \tag{A.9}$$

$$\eta_0 = 0.25 + \frac{0.25(\eta - 0.25)}{0.25 - \alpha} \qquad \text{(A.10)}$$

Interpolations in each sub-region

The parameters for the FCBI calculation are derived from the linear interpolation assumption inside the six sub-regions at each element side that belongs to each region. Therefore, in each sub-region, a new coordinate systems, (r_0, s_0) is defined as shown below (figure A.2)

In sub-region a_{11}

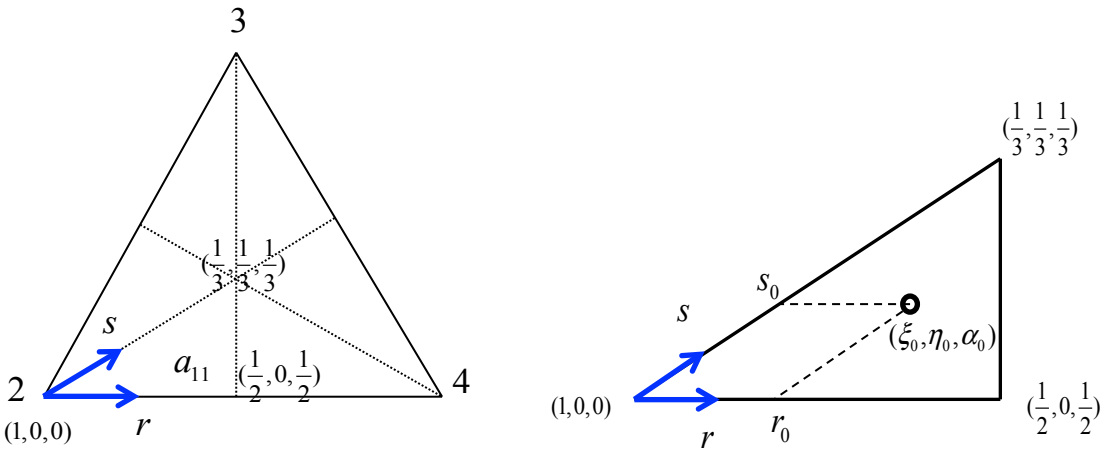

(Fig. A.2) Definition of the natural coordinate inside a sub-region a_{11}

Satisfying $s_0 = 3\eta_0$ and $(1,0,0) + s_0(-\frac{2}{3},\frac{1}{3},\frac{1}{3}) + r_0(-\frac{1}{2},0,\frac{1}{2}) = (\xi_0,\eta_0,\alpha_0)$ gives

$$(r_0, s_0) = (2\alpha_0 - 2\eta_0, 3\eta_0) \qquad \text{(A. 11)}$$

In a similar fashion, the natural coordinates of the 24 sub-regions use the projected flux calculation points on the element sides. Once the natural coordinates inside the triangle are identified, the linear interpolation inside the triangular region is applied.

$$\underline{v} = (1 - r_0 - s_0)\underline{v}_{(r_0,s_0)=(0,0)} + r_0\underline{v}_{(1,0)} + s_0\underline{v}_{(0,1)} \qquad \text{(A.12)}$$

For example, in the sub-region a_{11}, the velocity distribution is as follows:

$$\underline{v} = (1-\eta_0-2\alpha_0)\underline{v}_2 + 3\eta_0\underline{v}_{p24} + (2\alpha_0-2\eta_0)\underline{v}_{p243} \tag{A.13}$$

Appendix B

Some theoretical properties of FCBI elements

FCBI functions are always positive and less than or equal to 1.

The function value of the interpolation is always positive and less than or equal to one. The solution of the 1 dimensional advection-diffusion equation is:

$$\underline{v} = \frac{e^{\mathrm{Re}} - e^{\mathrm{Re}x^*}}{e^{\mathrm{Re}} - 1}\underline{v}_1 + \frac{e^{\mathrm{Re}x^*} - 1}{e^{\mathrm{Re}} - 1}\underline{v}_2 \qquad \text{(B.1)}$$

where $\mathrm{Re} = \frac{\rho l}{\mu}\left(\frac{1}{2}(\underline{u}_c^1 + \underline{u}_c^2)\right)$ and $x^* = \frac{|\underline{x} - \underline{x}_1|}{l}$

Here l denotes the distance between the nodes 1 and 2, and the convection velocity that is used for calculating the element Reynolds number, Re, is the averaged convection velocity projected in the direction of $\underline{x}_2 - \underline{x}_1$. The non-dimensional coordinate x^* is normalized with l and has the value of 0 at node 1 and 1 at node 2 (see figures B.1 and B.3). When the element Reynolds number is positive, the interpolation is calculated as follows:

$$h_1 + h_2 = \frac{e^{\mathrm{Re}} - e^{\mathrm{Re}x^*}}{e^{\mathrm{Re}} - 1} + \frac{e^{\mathrm{Re}x^*} - 1}{e^{\mathrm{Re}} - 1} = 1 \qquad \text{(B.2)}$$

The interpolation values for both the positive and negative element Reynolds number cases show that the interpolation is not negative or greater than 1 (see figures B.2 and B.4). And the addition of the interpolation values equals 1. In other words, the completeness condition is satisfied.

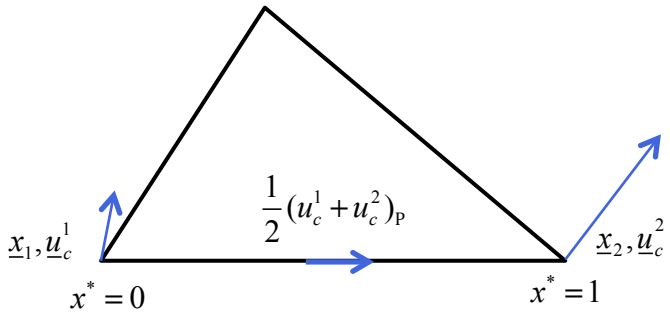

(Fig. B.1) A case when the element Reynolds number is positive

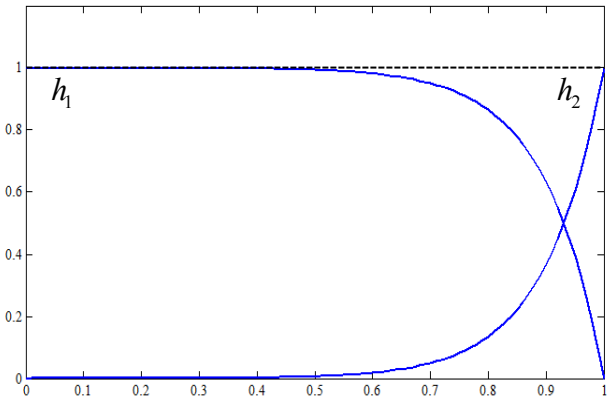

(Fig. B. 2) Interpolation of FCBI when the element Reynolds number is positive

When the element Reynolds number is negative we have:

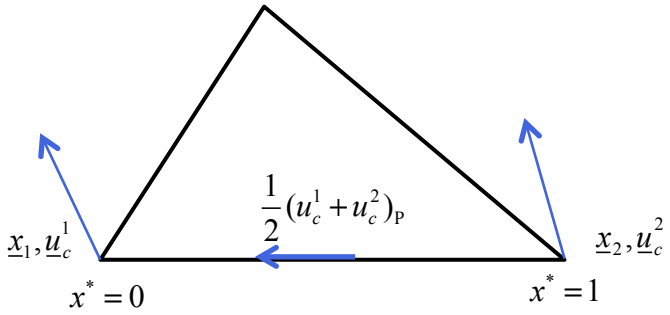

(Fig. B.3) A case when the element Reynolds number is negative

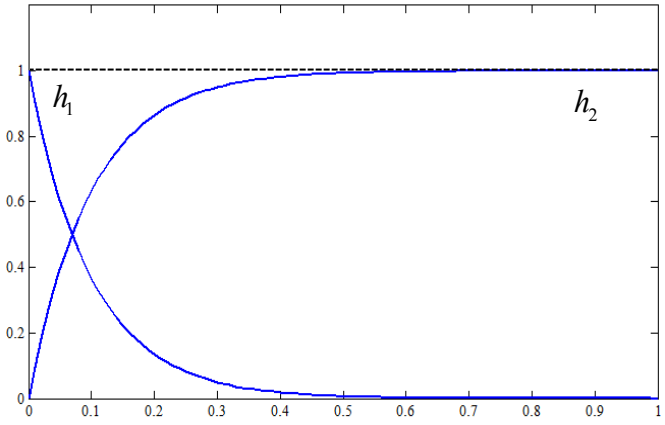

(Fig. B.4) Interpolation of FCBI when the element Reynolds number is negative

FCBI scheme requires finite Reynolds numbers.

Let us highlight one limitation of the FCBI method. Since the interpolation is calculated with the Reynolds number, inviscid flow problems cannot take advantage of the scheme. Let us examine the consequences of the inviscid condition on the presented scheme. Suppose we have a flow problem in a triangular fluid domain as shown in figure B.5.

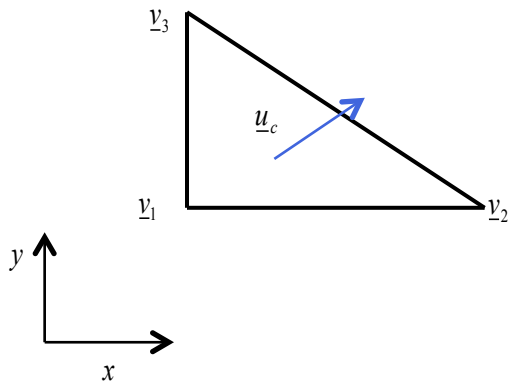

(Fig. B. 5) A problem in a triangular domain

The advection-diffusion equation is originally written as equation (B.3). However, now the Reynolds number is infinite because the zero dynamic viscosity is zero. Therefore, the advection diffusion equation of the inviscid flow can be represented as equation (B.4).

$$\underline{u}_c \cdot \nabla \underline{v} = \frac{1}{\mathrm{Re}_e} \nabla^2 \underline{v} \tag{B.3}$$

$$\underline{u}_c \cdot \nabla \underline{v} = 0 \tag{B.4}$$

Accordingly, the governing equation can be rewritten as equation (B.5)

$$\underline{u}_{cx} \frac{\partial \underline{v}}{\partial x} + \underline{u}_{cy} \frac{\partial \underline{v}}{\partial y} = 0 \tag{B.5}$$

For the case when the y-directional convection velocity is zero, equation (B.6) is satisfied.

$$\frac{\partial \underline{v}}{\partial \xi} = 0 \tag{B.6}$$

That is, the velocities of the nodes 1 and 2 have to be equal, which violates the independence of the nodal degrees of freedom. Thus, the method cannot be applied to completely inviscid flow problems.

Appendix C

Patch tests of tetrahedral FCBI elements

The patch test is an indicator of the quality of a finite element method and is required to ensure its completeness [35]. The patch test has to be passed with an assemblage of much distorted elements [16]. Two test cases, a constant velocity input case and a constant stress input case, are performed to verify the elements. These cases are chosen because we can estimate the solutions by continuity criteria and by calculation of partial differential equations (stress-strain relations of fluid elements).

Constant velocity input

First, we apply a constant velocity as an input to all boundary points and check the interior nodal points, including the barycenter nodes of all elements. The result must be the applied constant velocity. Meshes used for the patch test consist of 8 hexahedra: 2 hexahedra in x-, y- and z-direction each (see figure C.2 and Table C.1). One hexahedron contains 6 tetrahedral elements (see section 4.1), therefore, there are 48 tetrahedral elements used.

The results should show the continuity of the velocities across the element boundaries. Since there is no external stress load applied, the velocity distribution should be the same as U_x inside the patch. Figure C.3 shows the velocity vectors calculated with the 3-D FCBI method. The error is measured as the L2 norm of the velocity vectors.

$$E_U = \sqrt{\sum_{i=1}^{\#node} ((u_x^{(i)} - U_x)^2 + (u_y^{(i)})^2 + (u_z^{(i)})^2)} \qquad \text{(C.1)}$$

where $U_x = 1$ and u_x, u_y and u_z are nodal velocities. The error E_U of the patch test suggested at Figure C.1 is 8.2154×10^{-15}. Therefore, the completeness condition is satisfied for this case.

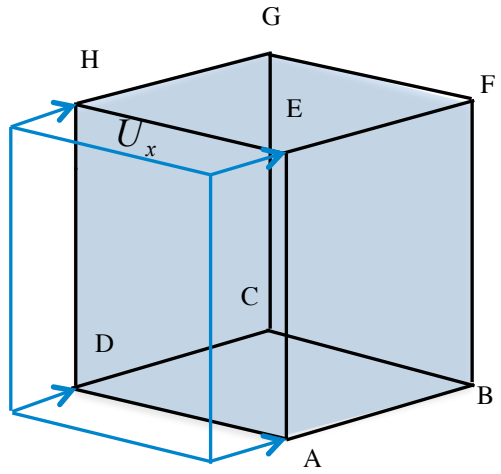

(Fig. C.1) Problem definition of a patch test with a constant velocity boundary input

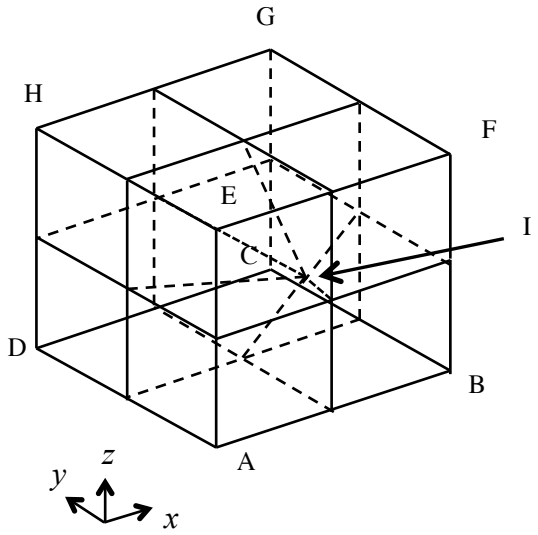

(Fig. C.2) Hexahedra used for patch tests

(Table C.1) Coordinates of the patch's corner points and an interior mesh point

Points	*x*	*y*	*z*
A	0	0	0
B	1	0	0
C	1	1	0
D	0	1	0
E	0	0	1
F	1	0	1
G	1	1	1
H	0	1	1
I	0.7	0.4	0.35

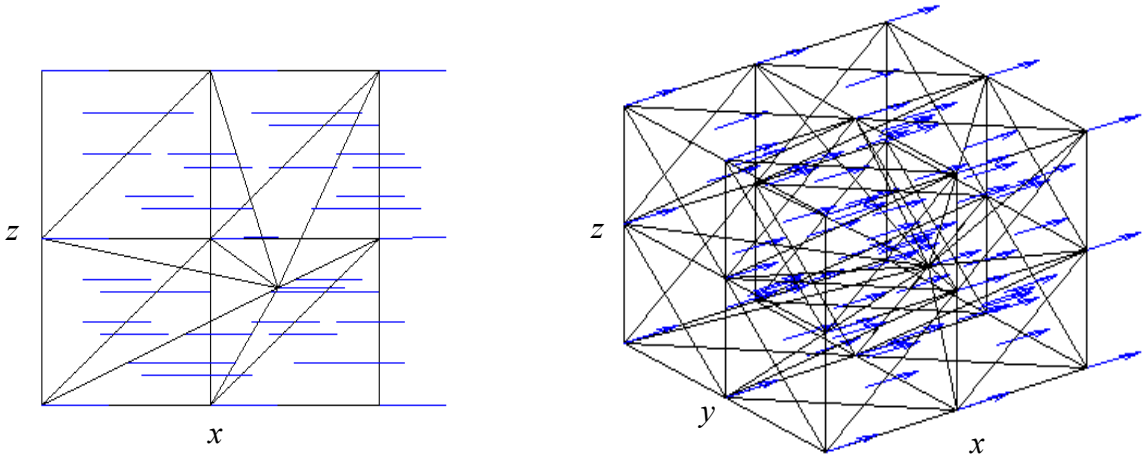

(Fig. C.3) Velocity vector plots of the patch test with prescribed velocity

Constant stress input

Next, a patch test with constant stress loading is also required to verify the inter-element velocity continuity [35]. The externally applied stress has to be identical to the internal stress distribution. To calculate the stress distribution more accurately, a relatively large viscosity is used. Therefore, we use the values $\rho = 1$ and $\mu = 10$ for the density and the dynamic viscosity, respectively.

At the walls H-E-F-G and D-C-B-A, the z velocity is set zero (see figure C.4(a)). In order to make the solution unique, we set point A as stagnant. The external given stresses and internal stresses, τ and σ respectively, are expressed as follows:

$$\tau = \begin{bmatrix} T & \tau_{xy} & \tau_{xz} \\ \tau_{xy} & T & \tau_{yz} \\ \tau_{xz} & \tau_{yz} & T \end{bmatrix} = \begin{bmatrix} 1 & 0.1 & 0.5 \\ 0.1 & 1 & 0.3 \\ 0.5 & 0.3 & 1 \end{bmatrix}, \tag{C.2}$$

$$\sigma = \begin{bmatrix} -P + 2\mu(\frac{\partial u_x}{\partial x}) & \mu(\frac{\partial u_y}{\partial x} + \frac{\partial u_x}{\partial y}) & \mu(\frac{\partial u_z}{\partial x} + \frac{\partial u_x}{\partial z}) \\ \mu(\frac{\partial u_y}{\partial x} + \frac{\partial u_x}{\partial y}) & -P + 2\mu(\frac{\partial u_y}{\partial y}) & \mu(\frac{\partial u_z}{\partial y} + \frac{\partial u_y}{\partial z}) \\ \mu(\frac{\partial u_z}{\partial x} + \frac{\partial u_x}{\partial z}) & \mu(\frac{\partial u_z}{\partial y} + \frac{\partial u_y}{\partial z}) & -P + 2\mu(\frac{\partial u_z}{\partial z}) \end{bmatrix} \tag{C.3}$$

The error for this case can be measured with the L2 norm of the differences of the stress tensors.

$$E_T = \sqrt{\sum_{k=1}^{\#node} [\sum_{j=1}^{3} \sum_{i=1}^{3} (\sigma_{ij} - \tau_{ij})^2]} \tag{C.4}$$

The error E_T is 0.0104. This is a rather small difference but induced by the convective effect. However, making dynamic viscosity $\mu = 1{,}000$ results in the error $E_T = 1.0308 \times 10^{-6}$. The velocity vector plot is shown in figure C.5.

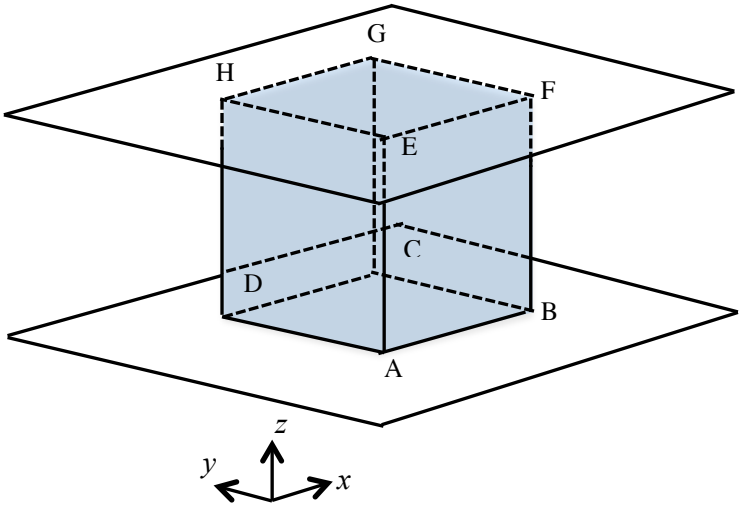

(a)

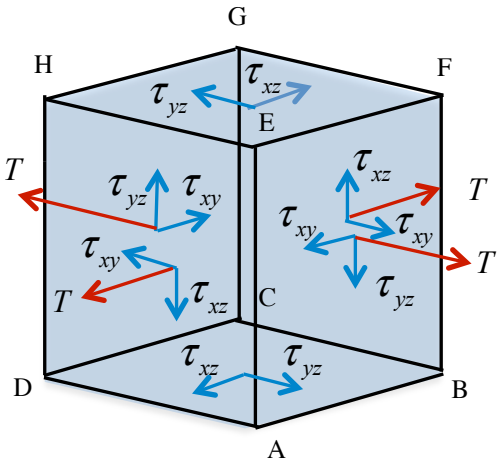

(b)

(Fig. C.4) Application of the stress input: (a) problem definition of the stress input case
(b) normal tractions and stress applied

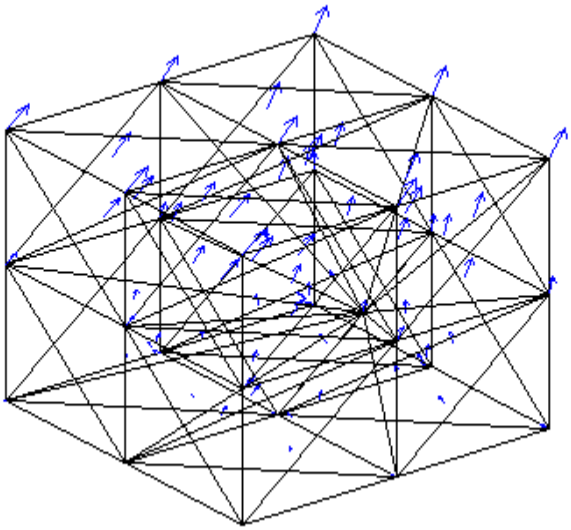

(Fig. C.5) Velocity vector plot of the patch test with normal traction and constant shear stress input with $\mu = 10$

Bibliography

[1] T. Okamoto and M. Kawahara, Two-dimensional sloshing analysis by Lagrangian finite element method, INT J NUMER METH FL, 11, 453-477, 1990.

[2] C. W. Hirt and B. D. Nichols, Volume of fluid method for the dynamics of free boundaries, J COMPUT PHYS, 39, 201-225, 1981.

[3] J. Lopez, J. Hernandez, P. Gomez, and F. Faura, An improved PLIC-VOF method for tracking thin fluid structures in incompressible two-phase flows, J COMPUT PHYS, 208, 51-74, 2005.

[4] D. Enright, R. Fedkiw, J. Ferziger, and I. Mitchell, A hybrid particle level set method for improved interface capturing, J COMPUT PHYS, 183, 83-116, 2002.

[5] M. Preisig and T. Zimmermann, Free-surface dynamics on moving domains, COMPUT METHOD APPL M, 200, 372-382, 2011.

[6] J. Grooss and J. S. Hesthaven, A level set discontinuous Galerkin method for free surface flows, COMPUT METHOD APPL M, 195, 3406-3429, 2006.

[7] C. E. Kees, I. Akkerman, M. W. Farthing and Y. Bazilevs, A conservative level set method suitable for variable-order approximations and unstructured meshes. J COMPUT PHYS, 230, 4536-4558, 2011.

[8] C. S. Wu, D. L. Young and C. L. Chiu, Simulation of wave-structure interaction by hybrid Cartesian/immersed boundary and arbitrary Lagrangian-Eulerian finite-element method, J COMPUT PHYS, 254, 155-183, 2013.

[9] B. Ramaswamy, Numerical simulation of unsteady viscous free surface flow, J COMPUT PHYS, 90, 396-430, 1990.

[10] K. J. Bathe and H. Zhang, A flow-condition-based interpolation finite element procedure for incompressible fluid flows, COMPUT STRUCT, 80, 1267-1277, 2002.

[11] H. Kohno and K. J. Bathe, A flow-condition-based interpolation finite element procedure for triangular grids, INT J NUMER METH FL, 51, 673-699, 2006.

[12] H. Kohno and K. J. Bathe, Insight into the flow-condition-based interpolation finite element approach: solution of steady-state advection-diffusion problems, INT J NUMER METH ENG, 63, 197-217, 2005.

[13] P. A. Sackinger, P. R. Schunk, and R. R. Rao, A Newton-Raphson pseudo-solid mapping technique for free and moving boundary problems: a finite element implementation, J COMPUT PHYS, 125, 83-103, 1996.

[14] M. Iwata, K. Sriyudthsak, M. Y. Hirai, and F. Shiraishi, Estimation of kinetic parameters in an S-system equation model for a metabolic reaction system using the Newton-Raphson method, MATH BIOSCI, 248, 11-21, 2013.

[15] R. I. Jennrich and S. M. Robinson, A Newton-related algorithm for maximum likelihood factor analysis, PSYCHOMETRIKA, 34, 111-123, 1969.

[16] K. J. Bathe, Finite element procedures, 2nd edition, Prentice hall, Watertown, MA, 2014.

[17] H. Braess and P. Wriggers, Arbitrary Lagrangian Eulerian finite element analysis of free surface flow, COMPUT METHOD APPL M, 95-109, 2000.

[18] X. Wang and K.J. Bathe, Displacement/pressure based mixed finite element formulations for acoustic fluid-structure interaction problems, INT J NUMER METH ENG, 40, 2001-2017, 1997.

[19] J. C. Martin and W. J. Moyce, An experimental study of the collapse of liquid, PHILOS T R SOC A, 244, 312-324, 1952.

[20] W. Rumold, Modeling and simulation of vehicles carrying liquid cargo, MULTIBODY SYST DYN, 5, 351-374, 2001.

[21] Z. K. Gao, X.W. Zhang, N. D. Jin, N. Marwan, and J. Kurths, Multivariate recurrence network analysis for characterizing horizontal oil-water two-phase flows, PHYS REV E, 88, 032910, 2013.

[22] V. Sabelnikov and C. Fureby, LES combustion modeling for high Re flames using a multi-phase analogy, COMBUST FLAME, 160, 83-96.2013.

[23] C. X . Zhao and A. P. J. Middelberg, Two-phase microfluidic flows, CHEM ENG SCI, 66, 1394-1411, 2011.

[24] M. Cruchaga, D. Celentano, and T. Tezduyar, A moving Lagrangian interface technique for flow computations over fixed meshes, COMPUT METHOD APPL M, 191, 525-543, 2001.

[25] J. Matsumoto, A relationship between stabilized FEM and bubble function element Stabilization method with orthogonal basis for incompressible flows, J APPL MECH, 8, 2005.

[26] S. N. Atluri and T. Zhu, A new meshless local Petrov-Galerkin approach in Computational mechanics, COMPUT MECH, 22, 117-127, 1998.

[27] U. Ghia, K.N. Ghia, and C.T. Shin, High-Re solutions for incompressible flow using Navier-Stokes equation and a multigrid method, J COMPUT PHYS, 48, 387-411, 1982.

[28] C. G. Koh, M. Luo, M. Gao and W. Bai, Modeling of sloshing with constrained floating baffle, COMPUT STRUCT, 122, 270-279, 2013.

[29] C. H. Wu, B.F. Chen, and T.K. Hung, Hydrodynamic forces induced by transient sloshing in a 3D rectangular tank due to oblique horizontal excitation, COMPUT STRUCT, 65, 1163-1186, 2013.

[30] F. D. Pin S. Idelsohn, E. Oñate, and R. Aubry, The ALE/Lagrangian particle finite element method : a new approach to computation of free-surface flows and fluid-objective interfaces, COMPUT FLUIDS, 36, 27-38, 2007.

[31] B. D. Guo, P. Liu, Q. L. Qu, J. L. Wang, and P.Q. Liu, Fluid-structure interaction modeling by ALE and SPH, APPL MECH MATER, 275-277, 393-397, 2013.

[32] M. B. Liu and G. R. Lin, Smoothed particle hydrodynamics (SPH): an overview and recent developments, ARCH COMPUT METHODS ENG, 17, 25-76, 2010.

[33] S. Ham, B. Lai, and K. J. Bathe, The method of finite sphere for wave propagation problems, COMPUT STRUCT, 142, 1-14, 2014.

[34] M. I. Herreros and M. Mabssout, A two-steps time discretization scheme using the SPH method for shock wave propagation, COMPUT METHOD APPL M, 200, 1833-1845, 2011.

[35] A. Razzaque, The patch test for elements, INT J NUMER METH ENG, 22, 63-71, 1986.